# PAVEMENT SURFACE CHARACTERIZATION FOR OPTIMIZATION OF TRADEOFF BETWEEN GRIP AND ROLLING RESISTANCE

**FINAL PROJECT REPORT**

by

Shabnam Rajaei
Roozbeh Dargazany
Karim Chatti
Michigan State University

Sponsorship
Center for Highway Pavement Preservation
(CHPP)

for

Center for Highway Pavement Preservation
(CHPP)

UNIVERSITY TRANSPORTATION CENTER for HIGHWAY PAVEMENT PRESERVATION

In cooperation with US Department of Transportation-Office of the Assistant Secretary for Research and Technology (OST-R)

August 2016

**Disclaimer**

The contents of this report reflect the views of the authors, who are responsible for the facts and the accuracy of the information presented herein. This document is disseminated under the sponsorship of the U.S. Department of Transportation's University Transportation Centers Program, in the interest of information exchange. The Center for Highway Pavement Preservation (CHPP), the U.S. Government and matching sponsor assume no liability for the contents or use thereof.

Technical Report Documentation Page

| | | |
|---|---|---|
| 1. Report No.<br>CHPP Report-MSU#3-2016 | 2. Government Accession No. | 3. Recipient's Catalog No. |
| 4. Title and Subtitle<br>Pavement Surface Characterization for Optimization of Tradeoff between Grip and Rolling Resistance | | 5. Report Date<br>August 2016<br>6. Performing Organization Code |
| 7. Author(s)<br>Shabnam Rajaei, Roozbeh Dargazany, Karim Chatti | | 8. Performing Organization Report No. |
| 9. Performing Organization Name and Address<br>CHPP<br>Center for Highway Pavement Preservation,<br>Tier 1 University Transportation Center<br>Michigan State University, 2857 Jolly Road, Okemos, MI 48864 | | 10. Work Unit No. (TRAIS)<br>11. Contract or Grant No.<br>USDOT DTRT13-G-UTC44 |
| 12. Sponsoring Organization Name and Address United States of America<br>Department of Transportation<br>Office of the Assistant Secretary for Research and Technology | | 13. Type of Report and Period Covered<br>14. Sponsoring Agency Code |
| 15. Supplementary Notes<br>Report uploaded at http://www.chpp.egr.msu.edu/ | | |

16. Abstract

Understanding the contact deformation behavior between pavement and tires within the contact patch is of great significance in revealing the mechanism of rolling resistance, grip and sound analysis. The concepts and mechanisms behind pavement friction are quite involved and not easily understood. Moreover, because there are many factors that affect friction, it is more of a process than an inherent characteristic of the pavement.

Here, a short literature survey on methods of pavement surface characterization, friction, and rolling resistance prediction are presented. The surface texture is then characterized by different means, e.g. statistical parameters and fractal techniques. It has been found that statistical parameters are scale dependent and they change by sample size. Therefore, fractal techniques is a better way for surface representation. A surface is then generated successfully using Fourier transform.

Focusing on effect of surface micro-texture on tread rubber energy loss, a finite element model is generated using commercial software ABAQUS. Common assumptions and finding of contact mechanics models are then validated and the energy loss due to predefined surfaces are calculated. In addition, a UMAT subroutine code has been prepared for characterizing the rubber material properties.

| | | | |
|---|---|---|---|
| 17. Key Words<br>Pavement, Surface characterization, Friction, Rolling resistance | | 18. Distribution Statement<br>No restrictions. | |
| 19. Security Classification (of this report)<br>Unclassified. | 20. Security Classification (of this page)<br>Unclassified. | 21. No. of Pages<br>119 | 22. Price<br>NA |

Form DOT F 1700.7 (8-72) Reproduction of completed page authorized

## Table of Contents


CHAPTER 1 - INTRODUCTION....1
1.1 Statistical modeling of surface roughness....1
1.2 Simulation and laboratory characterization of the friction at different scales....1
1.3 Influence of pavement properties on Grip....2
1.4 Influence of pavement properties on rolling resistance....2
1.5 Characterization of tire properties in different speed ranges....3
CHAPTER 2 - LITERATURE REVIEW....5
2.1 Introduction....5
2.2 modelling of surface texture....6
2.2.1. Characterization and modeling:.... 7
2.2.2. Surface-texture measurements.... 15
2.3 Friction....18
2.3.1. Friction Measurements.... 21
2.3.2. Texture-Friction Relationship.... 24
2.4 Influence of pavement properties on rolling resistance....32
2.5 Characterization of tire properties in different speed ranges....34
CHAPTER 3 - Experimental data....35
3.1 Surface texture measurement....35
3.1.1. Sample preparation.... 35
3.1.2. Surface Measurement.... 36
3.2 Pavement surface friction tests....38
CHAPTER 4 - ANALYSIS METHOD....40
4.1 surface texture simulation....40
4.2 Fractal characterization of surfaces....40
4.3 Finding fractal parameters....40
4.3.1. 1D PSD.... 40
4.3.2. 2D PSD.... 41
4.3.3. Roughness-length method.... 42
4.3.4. Tessellation (Projective Covering) method.... 42
4.3.5. Structure function method.... 43
4.3.6. Other fractal parameters.... 43
4.4 Investigating multi-fractal nature of analyzed surfaces....44
4.4.1. Scale-dependent fractal nature of pavements.... 44
4.4.2. Anisotropy: driving direction on fractal pavements.... 45
4.5 Obtaining 3D surface....45
4.5.1. Fractal Interpolation methods.... 45
4.5.2. Simulation methods.... 46
4.5.3. Combination of simulation and interpolation.... 46

4.6 Influence of pavement properties on Hysteresis component in micro-scale......................48
4.6.1. FE model description ........................................................................................ 48
4.6.2. Running FE model ............................................................................................. 61
CHAPTER 5 - RESULTS.....................................................................................................63
5.1 Statistical characterization of A SURFACE .................................................................63
5.2 fractal parameters ..........................................................................................................63
5.2.1. 1D PSD ............................................................................................................... 63
5.2.2. 2D PSD ............................................................................................................... 64
5.2.3. Roughness-length method.................................................................................. 65
5.2.4. Tessellation (Projective Covering) method ........................................................ 66
5.2.5. Comparison of the methods ............................................................................... 67
5.2.6. Estimation of other fractal parameters (other than D) ......................................... 69
5.3 multi-fractal nature of the surfaces.................................................................................69
5.3.1. Scale-dependent fractal nature of pavements .................................................... 69
5.3.2. Anisotropy: driving direction on fractal pavements ........................................... 70
5.4 3D fractal surfaces...........................................................................................................71
5.4.1. BFIS model .......................................................................................................... 71
5.4.2. IFFT model .......................................................................................................... 72
5.4.3. Blackmore anisotropic surface simulation........................................................... 72
5.4.4. Combination of simulation and interpolation ...................................................... 74
5.4.5. Validation of the surface structure....................................................................... 74
5.4.6. Fractal analysis of generated surfaces.................................................................. 75
5.4.7. Statistical analysis of the generated surfaces ....................................................... 76
5.5 friction measurement.......................................................................................................76
5.6 pavement micro-texture effect on Hysteresis component ..............................................77
5.6.1. Hysteresis component of single wave surfaces.................................................... 77
5.6.2. Hysteresis calculation for multiple wave surfaces................................................ 77
5.6.3. Investigation of the relationship between contact area and applied pressure ......... 78
5.6.4. Investigation of the relationship between penetration depth and applied pressure 80
5.6.5. Investigation of the relationship between h/λ and applied pressure ....................... 81
5.6.6. Investigation of the relationship between h/λ and Hysteresis................................ 81
5.6.7. Subroutine verification.......................................................................................... 82
CHAPTER 6 - DISCUSSION AND CONCLUSION.................................................................87
TECHNOLOGY TRANSFER .................................................................................................88

## List of Figures

Figure 1. Correlation between Rolling resistance coefficient and mean profile depth (MPD) ...... 3
Figure 2.Viscoelastic response of tire tread at different contact points ........................................ 3
Figure 3. Contact Length Relative to Vehicle Velocity in Wet Concrete and Dry Asphalt Conditions (Matilainen and Tuononen 2012). ................................................................... 4
Figure 4.Texture wavelength influence on pavement-tire interactions (after Henry, 2000 and Sandburg and Ejmont, 2002) ............................................................................................ 5
Figure 5. Simplified illustration of various texture ranges for pavement surface (after Sandburg, 1998) ........................................................................................................................... 6
Figure 6. Surface texture characteristics ........................................................................... 6
Figure 7. Surface texture parameters ................................................................................ 7
Figure 8. Self-affinity of pavement surface ...................................................................... 7
Figure 9. Friction mechanism ........................................................................................... 18
Figure 10.Compositions of Major influences on braking slip conditions (Hall2009) ................. 19
Figure 11. Effect of water presence on contact area (a) contact without water, (b) contact in presence of water, and (c) contact zone ........................................................................ 21
Figure 12. The kinetic friction coefficient for rubber sliding on a carborundum surface under different conditions (Grosch1963) ................................................................................. 22
Figure 13. Friction measurement devices: (a) BPT (b) DFT (c) CFME (d) Locked-wheel (e) Fixed-slip (f) Variable-slip (g) Side-force .......................................................................... 24
Figure 14. Various parts of a detailed tire model.............................................................. 25
Figure 15. Contact of rubber with a rigid substrate as pavement ............................................... 26
Figure 16. Relationship between Skid resistance and Macro- and Micro-texture (Serigos, 2014) ............................................................................................................................ 30
Figure 17. Correlation between the fractal dimension and the friction for dried and wet surfaces (Kokkalis, 2002) .......................................................................................................... 30
Figure 18. Friction variation relationship with Hurst exponent.................................................. 31
Figure 19.Wet skid resistance versus speed for constant (a) macro- and (b) micro-textures (Noyce, 2005) ........................................................................................................... 31
Figure 20. Map of Michigan State University campus, demonstrating the location of cored samples.......................................................................................................................... 35
Figure 21. Core samples taken from MSU campus by research team ......................................... 36
Figure 22. Samples of different pavement treatments (a) HMA (b) Thin overlay Asphalt (c) Concrete (d) Single Chip seal (e) Double Chip seal ..................................................... 36
Figure 23. Surface Measurement by Confocal Microscopy ........................................................ 37
Figure 24. Surface Measurement by 3D laser scanner ............................................................... 37
Figure 25. Pavement surface texture measurement (a) areas in the same direction, (b) areas in circular direction ........................................................................................................ 37
Figure 26. Comparison of inherent slope of the profile before and after performing a detrending ........................................................................................................................... 38
Figure 27. British Pendulum test and Locked-wheel device ...................................................... 38
Figure 28. Structure of a well-behaved power spectral density plot. $f_L$ and $f_U$ denote the range in which the plot is linear; β is a slope of this linear tendency, found with e.g. regression plot ...... 41
Figure 29. Bi-fractality by Structure function method................................................................ 45
Figure 30. Diagram of the main approach of the project ............................................................ 48

Figure 31.A sample of wavelength combination for pavement surface simulation in FE model. 48
Figure 32. Periodic Boundary condition ........ 49
Figure 33. Periodic Boundary condition effect on stress distribution ........ 50
Figure 34. FE model geometry and applied loads ........ 51
Figure 35. General flow of analysis in ABAQUS and Material Subroutine involvement ........ 54
Figure 36. General Flowchart of steps required for writing a subroutine ........ 55
Figure 37. Rubber block meshing ........ 59
Figure 38. Representation of three 2D profiles of one surface through several statistical parameters ........ 63
Figure 39. Plots generated with the 1D-PSD script for a randomly chosen data array: a) PSD of all individual profiles of a sample, b) Regression plot for the average PSD c) Maximum, minimum, and average PSD plots, d) phase information corresponding to the average ........ 64
Figure 40. Plots generated with 2D-PSD method a) power image of the 2D surface, b) phase information resulting from the FFT, c) radial average of the power image shows a regular decline of signal's power in all directions, and d) PSD obtained by (log-log) plotting of power vs. frequency ........ 65
Figure 41. Graphs generated with the roughness-length method, a) plot shows a log-log plot of length of window vs. rms for one profile; b) collective plot of all profiles in the data set, and c) the distribution of D values in the data set. ........ 66
Figure 42. Projective Covering method; a) data points obtained by plotting total area estimations vs. grid size used, b) linear regression fit, c) two-segment regression fit, and d) three-segment regression fit ........ 67
Figure 43. Graphical representation of fractal dimension obtained from different methods in 10 random samples ........ 68
Figure 44. Graphical representation of fractal nature ranges found with three fractal methods for 10 samples ........ 68
Figure 45. Structure function of a) all profiles in the area, b) a randomly chosen profile in the area, and c) average of all structure function graphs. ........ 70
Figure 46. Angular histograms showing the magnitude of fractal dimension in different directions, with circles showing the mean value of D in all directions for each method ........ 71
Figure 47. Results of the driving direction analysis shown in non-circular form ........ 71
Figure 48. BFIS a) original surface containing only 9 points from the raw data, b) first iteration c) second iteration, and d) third iteration. ........ 72
Figure 49. IFFT method, a) generated surface, b) contour graph of the surface, c) PSDs in two directions-inputs ........ 73
Figure 50. Blackmore algorithm, a and c) surface based on 81 and 1600 data points, b and d) contour map of the surfaces in a and c ........ 73
Figure 51. BFIS enhanced Blackmore algorithm, a) surface generated with Blackmore algorithm, consisting of 9 points in total, surface generated after one (b), two (c), and three (d) BFIS interpolation iterations. ........ 74
Figure 52. Four models of a sample of the measurement data (in the middle); Using a) BFIS interpolation, b) iFFT simulation, c) Blackmore and Zhou's anisotropic model, and d) Blackmore and Zhou's model enhanced with BFIS interpolation; ........ 75
Figure 53. BPN values for different conditions of dry surface and contaminated surfaces of HMA ........ 76
Figure 54. Energy variation by time ........ 77

Figure 55. Rubber penetration depth ........ 77
Figure 56. Creep Dissipation for combination of (a) 4mm and 0.5mm wavelength surfaces (b) 4mm, 0.5mm, and 0.25mm wavelength surfaces........ 78
Figure 57. Effect of phase angle on creep dissipation of Combination of (a) $\lambda$=4mm and 2mm, (b) $\lambda$=4mm and 1mm, and (c) $\lambda$=4mm and 0.5mm........ 79
Figure 58. Load-contact relationship (a) for $\lambda$=4mm (b) for combination of $\lambda$=4mm, $\lambda$=1mm and $\lambda$=0.25mm. ........ 80
Figure 59. Comparison of area of contact for smooth and rough surfaces ........ 80
Figure 60. Load-Penetration relationship for (a) $\lambda$=4mm and (b) combination of $\lambda$=4mm, 1mm, and 0.25 mm........ 81
Figure 61. (a) $\lambda$-Pressure relationship for different surfaces with the same h/$\lambda$ ratio when they reach the full contact, (b) relationship between the required pressure for full contact and h/$\lambda$ ratio. ........ 81
Figure 62. Hysteresis variation for different surfaces with the same h/$\lambda$ ratio ........ 82
Figure 63. Calibration of Yeoh hyperelastic model........ 83
Figure 64. Calibration of hyperelastic-viscoelastic model ........ 84
Figure 65. Tensile test modeling in ABAQUS ........ 84
Figure 66. Verification of Hyperelastic UMAT ........ 85
Figure 68. (a) A standard linear solid model (b) response in very slow rates (c) response in very fast rates ........ 85
Figure 69. Stress-strain relationships for (a) Relaxation test with fast rate, (b) relaxation test with slow rate (c) creep test with fast rate, and (d) creep test with slow rate ........ 86

# List of Tables

Table 1. Statistical parameters for surface characterization ........................................................... 8
Table 2. Important factors in pavement friction (after Hall et al., 2009)...................................... 19
Table 3. Correlation between different friction test results .......................................................... 24
Table 4.Prony series coefficient for rubber material .................................................................... 51
Table 5. Inputs and outputs of UMAT Subroutines....................................................................... 53
Table 6. Relative error in fractal analysis of the generated surfaces ............................................ 75
Table 7. Relative error of statistical analysis of the generated surfaces ....................................... 76
Table 8. Calibrated constants for Yeoh hyperelastic model ......................................................... 82
Table 9. Calibrated constants for Viscoelastic model.................................................................... 83
Table 10. Verification of viscoelastic UMAT code....................................................................... 86

## List of Abbreviations

CHPP: Center of Highway Pavement Preservation
IPF: Infrastructure Planning and Facilities
MDOT: Michigan Department of Transportation
MSU: Michigan State University
USDOT: United States Department of Transportation

## Acknowledgments

This research has been supported by Center of Highway Pavement Preservation (CHPP) and funded by United States Department of Transportation (USDOT). We thank our colleagues from Infrastructure Planning and Facilities (IPF) of MSU and Michigan Department of Transportation who provided means and expertise that greatly assisted this research.

We also thank our students, Zuzanna Filipiak, Miguel Labrador, Asha Patel, Lance Roth, and Briana Wendland for their assistance with pavement surface measurements and characterization.

## Executive Summary

### Background

The environmental and economic aspects of the transportation sector are receiving considerable attention as a consequence of high oil prices and public awareness on global warming. Tires, as one of the important components of transportation industry, account for 17-21% of the total energy consumption (Matilainen and Tuononen 2012). Therefore, there is a major potential to reduce the energy consumption through optimization of tires. Generally, the hysteresis accounts for 90-95% of tire energy losses and 10% reduction in the average rolling resistance which promises 1 to 2% decrease in the fuel consumption (Clark 1981). However, decreasing rolling resistance may jeopardize grip performance of tires which plays a fundamental role in highway safety.

Of the many phenomena involved in tire–road friction studies, surface texture, especially in macro-scale, has received significant attention and increasing interest as it is expected to explain the complex friction mechanism. The wavelength contents of a surface, ranging from atomic scale to hundreds of meters long, cover a broad range of applications in science, but when it comes to road frictional safety aspects, this is limited to micro-, macro- and mega-scales, as classified in (PIARC 1987). There is now much evidence to support the effect of other intermediate ranges such as meso-scale (01.-1mm) and nano-scale (100nm to 5μm) on properties of rubber-pavement interface (Do et al. 2009, Chen and Wang 2011, Dunford et al. 2012, Kane et al. 2012, Kane et al. 2013).

Recent studies attempting to draw best texture indicators for the rubber friction modeling (Heinrich et al. 2000, Persson et al. 2005, Villani et al. 2011) launched the application of fractal theories in road pavement investigations. Many researchers have discussed and some have examined this potential of scale-independent fractal parameters in pavement friction evaluation (Kokkalis et al. 2002, Cafiso and Taormina 2007, Chen and Wang 2011). It is generally known that roughness at nano- and micro-scales have direct influence on grip, while rolling resistance is mainly influence by meso- and macro- scale roughness (Chen and Wang 2011). Accordingly, in view of different behavior of rubber at low and high speeds, an optimized roughness profile can be found which shows the best trade-off between these performances.

Despite the large body of laboratory data available concerning the role of texture in (on) the macro- and micro-scales, no comprehensive fieldwork appears to exist in the literature to address role of the texture on defining the properties of rubber-pavement interface in multi-scale. Moreover, the current pool of information is quite fragmented and has not been integrated into a comprehensive framework to address texture friction issues. For a comprehensive multi-scale study on role of texture, we have to implement a multi-scale visco-elastic model of rubber into a detailed model of surface texture and then fit them to the macro-scale experimental results obtained during the field tests.

### Problem Statement

To analyze tire-pavement interface, several theoretical and experimental studies have been conducted. Tsotras in 2010, proposed a dynamic model using modal parameters which is experimentally validated. It should be noticed that such a model, which is only based on a geometrical relationship, is not accurate enough for in-depth normal pressure distribution analysis.

In a study by Hall (2003), a transient contact algorithm is developed, consisting of an analytical belt model, a non-linear sidewall structure, and a discretized viscoelastic tread foundation. Elegant experimental methods can be found in literature (Shiobara et al. 1996, De Beer et al. 1997)

To model rolling resistance, a classic elastic ring model is introduced where a tire is simplified as an engineering structure with three principal components: a tread band foundation (the inflated sidewall); an elastic ring (the composite tread band), and the tread components. Recently, using a new optical platform, the changes of rolling resistance with respect to velocity has been measured (Matilainen and Tuononen 2012). The results indicated strong correlation between rolling resistance and tire velocity. A summary of the findings of each is given in the study by Jackson and Streator (2006).

A common approach to measure the surface roughness is the standard deviation of the profile heights, also known as the root mean square (RMS) roughness. However, the RMS roughness can vary significantly based on the sample length or size of the area being considered. Therefore, Fourier Transform and Fractal techniques are used to characterize the structure of roughness over many different scales (Kogut and Jackson, 2005, Dawkins et al). A surface can be characterized over multiple scales by transferring it into the frequency domain and using a spectrum. Fractal analysis of surfaces suggests the existence of a common fractal structure over many different types and scales of surfaces, including paved roads and tracks (Nielsen and Skibsted, 2010).

In 2011, approximately 71 percent of the petroleum used in the United States was utilized in the transportation sector, accounting for 27 percent of the U.S. energy demand. Therefore, by increasing of energy costs, and public awareness on global warming, the interest in improving vehicle fuel economy has escalated. While numerous factors such as vehicle aerodynamics and engine efficiency influence overall energy efficiency, one mechanism that dissipates energy inefficiently is in the contact between the tire and the pavement. This loss is often quantified by the rolling resistance, and it is also affected by the properties of the road pavement. Rolling resistance is a focal area in the field of sustainability because it directly impacts all three facets of environmental, economic, and sustainability.

## Key Methodology

In this project, various means of surface characterization are studied and discussed, such as statistical parameters (e.g. mean profile depth) and fractal techniques. Having the fractal dimension as the key parameter in fractal techniques, different methods for finding the fractal dimension are compared with each other, e.g. 1D PSD, 2D PSD, roughness-length method, and tessellation. Moreover, the ability of a fractal dimension for efficiently characterizing a pavement surface and the possibility of considering the pavement surface as a scale-dependent fractal surface are investigated. In addition, efforts have been done to find the difference between the fractal dimension in driving direction and other directions on the samples. The presence of scale dependency and variation of fractal dimension in different directions could be key factors in future studies for surface characterization and simulation and relating friction to surface texture.

At the next step, different surface simulation and interpolation techniques are employed such as BFIS, IFFT, Blackmore anisotropic simulation and a combination of BFIS and Balckmore. Surfaces are generated with each method and their results are compared with each other.

For modeling the tire-pavement interaction in micro-scale, the focus of this study has been on the tire tread only. For this purpose, the smallest possible section of tread is modeled based on the boundary condition which by applying periodic boundary condition it is extended to the whole tread model. The FE model is developed in ABAQUS commercial software. Only hysteresis component is considered at this stage. The rubber material is considered as elastic-viscoelastic and hyperelastic-viscoelastic in two different material characterizations. Prony-series and constitutive models using UMAT subroutine are used for this characterization. The viscoelastic properties of the pavement surface are neglected in the study and it is considered as a rigid surface. Different pavement surfaces are generated for investigation of the surface influence on rubber hysteresis. Different assumptions presented by previous studies in contact mechanics about the relationship between the applied load, contact area, and penetration depth are investigated and the hysteresis component is calculated using Prony-series.

**Major findings and their implications**

In surface characterization, the statistical parameters such as mean profile depth (MPD) are found to be scale dependent and variable with sample length. Therefore, they are not sufficient for surface simulation. After considering fractal techniques, it was found that the results obtained from structure function method are not within the range of other methods. 1D and 2D PSDs give similar results as found in the literature. However, the results of RMS-roughness and Projective covering methods give similar values, near 2, for most of the samples. Due to the wide range of wavelength and amplitude in a pavement surface, it could be more beneficial to characterize the surface in two or more scales and assign a fractal dimension to each scale individually, which is called scale dependency. Also the reduction of the fractal dimension in driving direction is demonstration of a limitation of the current studies in relating the vehicle performance to surface texture. The scale-dependency and variation of fractal dimension in different directions should be considered in surface characterization and simulation and also in relating friction to surface texture. The results of surface modeling shows that with the IFFT method a better result is achieved in comparison to the fractal techniques, which is in contrary to the expectations. This can demonstrates that the fractal techniques employed here are not completely developed in comparison to the IFFT method used. Therefore, additional investigation is required for obtaining a conclusion.

After running the FE model with different surfaces, the common assumptions and finding of contact mechanics models are investigated.  Different factors, such as the relationship between the applied load, contact area, and penetration depth are investigated. The model confirms most of the assumptions in contact mechanics, e.g. linearity of the applied load and contact area relationship. However, the assumption that the hysteresis of a surface is equal to the summation of the hysteresis of the individual length-scales is found to be true only when there is no phase angle between the different scales. In presence of a phase lag the hysteresis is found to be less than the summation. The effect of phase angle between the surfaces has not been addressed in previous studies and it seems to be significant especially in higher length scales. Therefore, it is necessary to be considered in the future studies.

# CHAPTER 1 - INTRODUCTION

## 1.1 STATISTICAL MODELING OF SURFACE ROUGHNESS

Fourier Transform and Fractal techniques can be used to characterize the structure of roughness over many different scales. A surface can be characterized over multiple scales by representing it using a frequency spectrum. It is widely recognized that pavement surface texture influences tire-pavement interactions, including friction, interior and exterior noise, splash and spray, rolling resistance, and tire wear. Friction is primarily affected by micro-texture and macro-texture, which correspond to the adhesion and hysteresis friction components, respectively.

The roughness and texture of road pavements can be measured and evaluated by means of unified procedures both for surveys and processing of acquired data, with the goal to represent the surface profile as a spectrum of spatial frequencies. Thus, it can be possible to explore an optimized area in the frequency vs. texture level graph, where the spectrum has to fall into, in order to balance some conflicting requirements such as grip and rolling resistance. The boundaries of the area can be also referred to as the specific characteristics of the examined infrastructures; if a spectrum fits into the area, an optimal behavior of the surface is ensured, with respect to the interaction phenomena between tires and pavement which are influenced by surface texture. 2D Fast Fourier transform of the surface height profile can be used in the analysis of the micro-texture; calculating the profiles and assuming an isotropic surface roughness, an angular average of the surface over the entire spatial frequencies can be derived. Separate profiles for each test, can be averaged to monitor the overall characteristics.

Representatives for texture profile in terms of wavelength allows optimization of the trade-off between performance parameters of pavement surface. Nevertheless, it should be taken into account that (i) the evaluation of classical methods for the surface profile are not consistent with each other, and (ii) the measurements are generally not sufficient to fully represent the surface profile. Accordingly, new functional parameters have to be introduced and coupled with previous ones in order to develop a universal consistent approach.

## 1.2 SIMULATION AND LABORATORY CHARACTERIZATION OF THE FRICTION AT DIFFERENT SCALES

Spectral analysis is unable to individually characterize the surface texture at actual road conditions. In linking texture to friction, the relation between fractal parameters, in particular Hurst exponent (H), with friction coefficient is of great interest in this research. The applicability of H, as an indicator of full surface profile specification, in road texture– friction studies at different scales in laboratory and field experiments is still required to be investigated.

Previously, some studies show that the changes in the micro-texture region have no direct influence on the friction coefficient. Since micro-variations in the top topographies of texture may be the crucial factor contributing to the hysteresis friction component of dry friction (Persson, 2001). H may not be the sole indicator of texture in these cases. Therefore, fractal analysis of the surface should be carried out to model the complex pavement surfaces. The specific information needed about texture depth and density at the contact patch should be simulated. A thorough study on the validity of fractal and spectral analysis only on the top surface profile of road pavements should be carried out and micro-variations on the top surface of aggregates should be studied.

## 1.3 INFLUENCE OF PAVEMENT PROPERTIES ON GRIP

The factors that influence pavement friction can be grouped into four categories environmental factors, vehicle operational parameters, tire properties, and pavement surface characteristics, where the latter two will be studied in this project. Friction generally consists of the following forces.

1. Adhesion
2. Hysteresis
3. Shear

All components of grip largely depend on the pavement surface characteristics, the contact area, and the properties of the tire. The adhesion force is generally proportional to the real area of adhesion between tire and surface asperities. The hysteresis force is generated within the deflected viscoelastic tire material and is a function of speed. The shear force is proportional to the area of shear developed. Generally, adhesion is related to micro-texture whereas hysteresis is mainly related to macro-texture. For wet pavements, adhesion drops off with increased speed while hysteresis increases with speed, so that above 56 mi/hr (90 km/hr), the macro-texture has been found to account for over 90 percent of the friction. In the case of winter friction on snow and ice, the shear strength of the contaminant is the limiting factor.

Since adhesion force is developed at the pavement–tire interface, it is most responsive to the micro-level asperities (micro-texture) of the aggregate particles contained in the pavement surface. In contrast, the hysteresis force developed within the tire is most responsive to the macro-level asperities (macro-texture). As a result of this phenomenon, adhesion governs the overall friction on smooth-textured and dry pavements, while hysteresis is the dominant component on wet and rough-textured pavements. By exploring these correlations, it can be possible to find the optimized surface roughness which gives the best trade-off between hysteresis and adhesion.

## 1.4 INFLUENCE OF PAVEMENT PROPERTIES ON ROLLING RESISTANCE

The relationship between pavement surface texture and fuel consumption has not been thoroughly determined so far. Previously, an estimate of the influence was inferred from independent relationships between pavement surface texture and tire rolling resistance and between tire rolling resistance and fuel consumption. The tire rolling resistance consists of three major components which influence from different roughness spectrum

1. Tire deflection and bending (Macro-, mega- roughness)
2. Tread slip (Meso-, micro-)
3. Tread surface deformation ( micro-, nano)

The contributions of these terms are not clear at the moment and the role of these components in different speeds and roughnesses should be explored.

An example of the correlations between texture and rolling resistance is given in Figure 1Figure 1 using a standard tire (Sandberg et al. 2011). It appears that despite only having one data point with a high texture value, the correlations between texture and rolling resistance were strong.

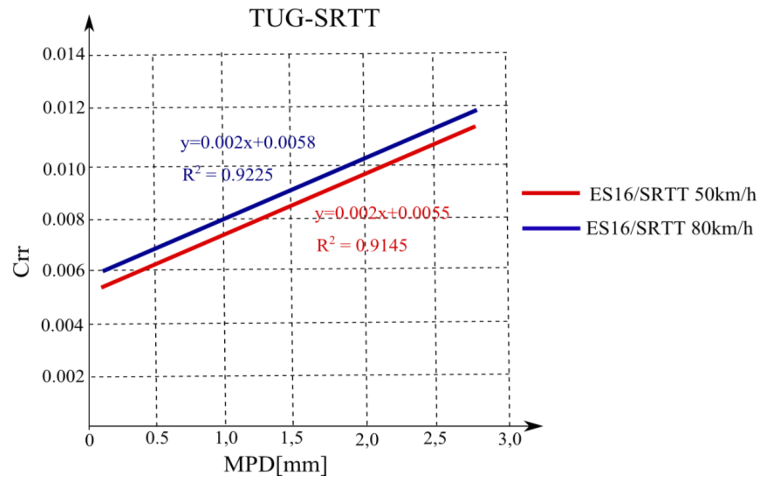


Figure 1. Correlation between Rolling resistance coefficient and mean profile depth (MPD)

Therefore, a comprehensive analysis on the role of tire viscoelasticity and pavement texture in rolling resistance is required. It is well known that rolling resistance is characterized by viscoelastic response of tire material, however, the details of this correlation are still far from being understood (see Figure 2). Thus, rolling resistance should be represented as the sum of the three aforementioned components, each of which is influenced by road texture and tire material properties.

The viscoelastic rubber properties can be modeled using a micro-mechanical model that will be developed within this project. The Tire deflection can be modeled as Rayleigh damping, the tread slip as frequency independent (viscous) damping, and tread deformation as high frequency micro-loading. Measured road texture profiles can be used as an input to study the combined influence of road texture and tread pattern on rolling resistance.

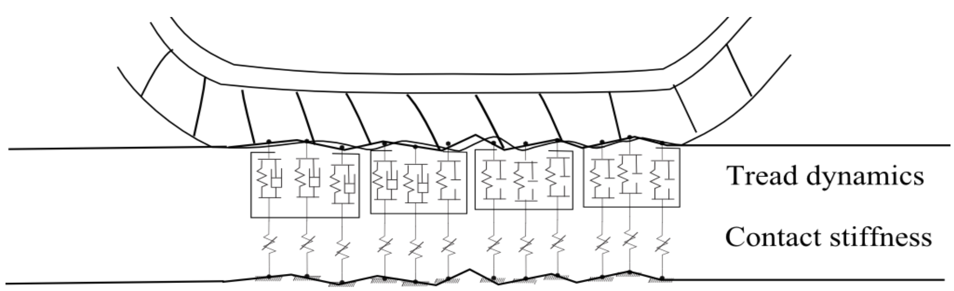


Figure 2.Viscoelastic response of tire tread at different contact points

### 1.5 CHARACTERIZATION OF TIRE PROPERTIES IN DIFFERENT SPEED RANGES

Tread slip and surface deformation are generally subjected to the dynamic loads with excitation frequency characterized by roughness of the pavement and tire velocity. Moreover, velocity has an important influence on the contact patch length (Hall,2003) (see Figure 3). Hence, the velocity of the wheel has significant impacts on the Rolling resistance and grip performances.

The influence of the velocity on tire-pavement interface can be modeled by simulating the contact patch and loading it with respect to the analyzed roughness of the surface. The behavior of rubber in different speed range is characterized by different material behavior which can be modeled through a generalized multi-scale material model. The influence of different components of hysteresis on rolling resistance in different speed range can be coupled by the revolution of friction with speed to obtain a complete picture of the correlation between Hysteresis-friction-velocity. Using this understanding an optimized road surface profile for a specific set of performances can be obtained.

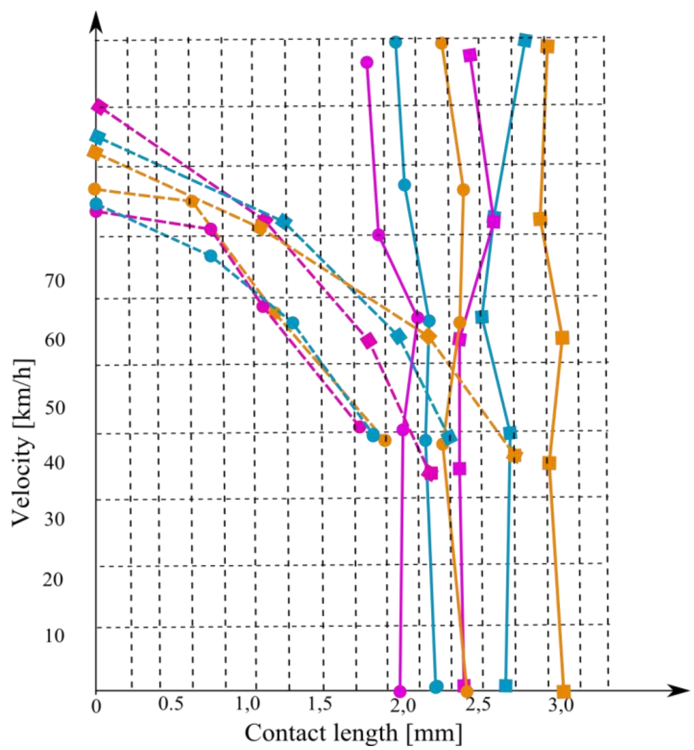


Figure 3. Contact Length Relative to Vehicle Velocity in Wet Concrete and Dry Asphalt Conditions (Matilainen and Tuononen 2012).

The work presented here consists of (i) thorough literature review of pavement surface, friction, and rolling resistance with emphasize on the role of micro-texture, (ii) surface characterization and simulation, (iii) rubber material modeling, and (iv) tire tread-pavement surface interaction modeling using FE model in ABAQUS commercial software.

# CHAPTER 2 - LITERATURE REVIEW

## 2.1 INTRODUCTION

Many factors are involved in the design of a pavement surface including safety, load capacity, ride quality, durability, noise and cost. A balance should be maintained among these parameters. Although some of the mentioned parameters can be controlled by proper material and construction methods, none of the design methodologies address friction and texture control properly. National Highway Traffic Safety Administration (NHTSA) reported that in 2013, 32,719 people lost their lives in motor vehicle traffic crashes and 2.3 million people were injured throughout the USA. About 15-18% of these crashes are related to wet pavements (Smith 1977, FHWA 1990, Davis et al. 2002). Strong relationship has been found between pavement skid resistance and accidents (Wen and Cao, 2006, Mayora 2009). The results showed that it is possible to decrease the accident rate by improving the friction of hazardous areas. While increasing the friction significantly increases safety, it negatively influences tire-road noise and rolling resistance [9, 10]. Therefore, there exists a tradeoff between these three phenomena; braking performance, rolling resistance, and noise.

The tire-pavement interaction depends on three components; tire, pavement, and operating conditions. In pavement, surface texture is one of the main factors influencing different aspects of tire-pavement interaction such as friction, rolling resistance, noise, etc. When tire roles over the pavement surface, a fraction of the texture will penetrate into the rubber, later on referred to as engaged texture. The relationships between various engaged texture wavelength and these aspects are shown in Figure 4.

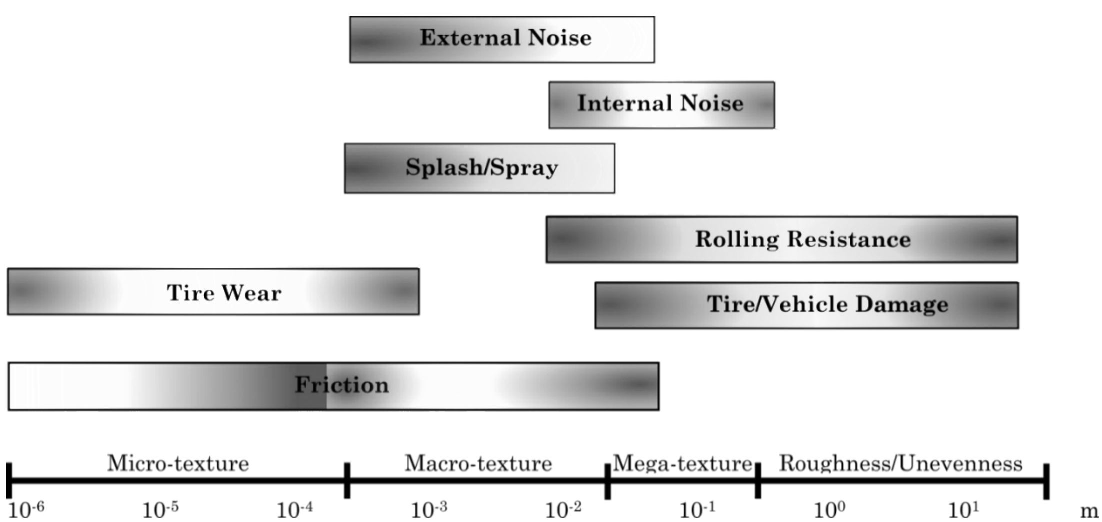


Note: Darker shading is an indicator of a more favorable effect of texture

Figure 4.Texture wavelength influence on pavement-tire interactions (after Henry, 2000 and Sandburg and Ejmont, 2002)

The engaged textures can be categorized into micro-, macro-, and mega-texture. Despite considerable progress in understanding macro- and mega-texture and its contribution to tire-pavement interaction, our understanding of the micro-texture remains to be developed.

This chapter is organized as follows: In section 2.2, pavement surface characterization and modeling will be studied. Several surface measurement methods will be discussed. In section 2.3, the underlying mechanism of friction and its contributing factors will be studied. Several friction measurement techniques will be discussed. Also the models that formulate the link between surface texture and friction will be addressed. In section 2.4, the influence of pavement surface textures on rolling resistance will be discussed and the coupling between friction and rolling resistance will be studied. In the final section, the effect of velocity on tire properties will be addressed.

## 2.2 MODELLING OF SURFACE TEXTURE

Pavement surface texture is characterized as deviations of the surface from a true planar surface which can be divided into different scales of unevenness or roughness, mega-texture, macro texture and micro texture (Figure 5). Permanent International Association of Road Congresses (PIARC) (1987) defined micro-texture as a wavelength shorter than 0.5 mm and peak to peak amplitude of 0.001 to 0.5 mm while characterizing the macro-texture by wavelength of 0.5 mm to 50 mm and peak to peak amplitude of 0.1 to 20mm. Also, it is known that micro-texture is a function of aggregate particle mineralogy. Figure 6 demonstrates a representation of texture characteristics.

Noyce et al (2005) referred to micro-texture as the irregularities of the aggregate particles surface in micro-scale. It depends on particle mineralogy, initial roughness and its ability to preserve their roughness against environmental and traffic polishing (Jayawickrama et al., 1996, Noyce et al., 2005). Basically, micro-texture is the part of pavement texture which is not visible by naked eye and it makes the surface feel more or less harsh (KJ Kowalski(2012 ,

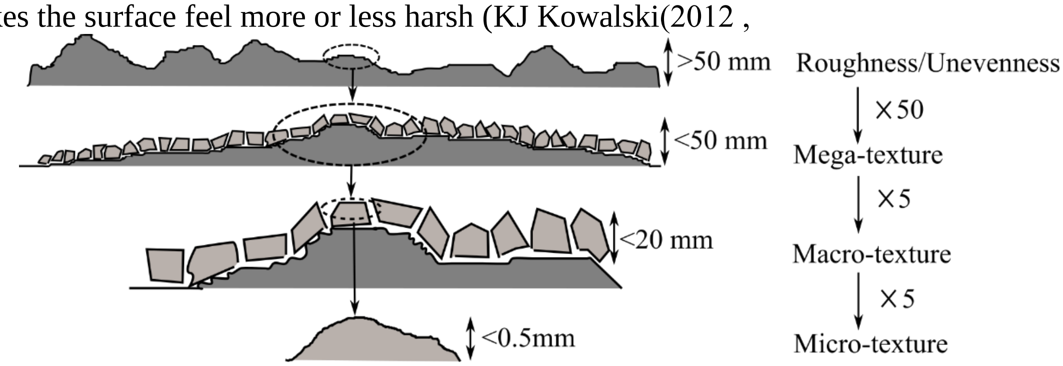


Figure 5. Simplified illustration of various texture ranges for pavement surface (after Sandburg, 1998)

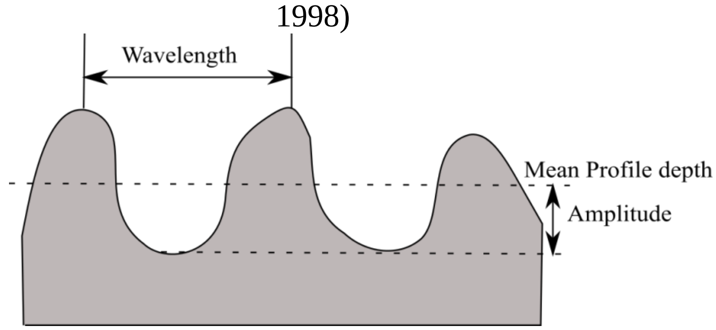


Figure 6. Surface texture characteristics

There are various parameters known to affect micro- and macro-texture in different pavement types (asphalt and concrete) such as Maximum aggregate dimensions, fine and coarse aggregate types, Mix gradation, Texture orientation etc (Sandberg, 2002, Henry, 2000, Rado, 1994, PIARC, 1995, ASSHTO, 1976). Among these factors only aggregate types are considered to influence micro-texture of the pavements.

#### 2.2.1. Characterization and modeling:

Seamless simulation of the pavement surfaces have been the focus of extensive studies. Characterization of the surface texture by wavelength and amplitudes into micro- and macro-texture cannot provide sufficient information. Having the same macro- and micro-texture. e.g. mean profile depth, in two different surfaces does not necessarily lead to similar friction levels (Kane, 2015). Therefore, other statistical parameters have been introduced to better represent the texture profile and its correlation with friction (yandell, 1971, Forster, 1981, yandell, 1994, sabey, 1959s, Do, 2004).

The statistical parameters can be categorized into four groups; (i) amplitude parameters, e.g. mean profile depth, mean texture depth, root mean square, skewness, and Kurtosis, (ii) functional parameters, e.g. surface bearing index, (iii) Hybrid parameters, e.g. surface area ratio, and (iv) spacing parameters, e.g. texture aspect ratio and direction (Li et al ,2016).

Table 1 represents some of these parameters used for characterization of the pavement texture. Parameters used in these formulae are illustrated in Figure 7.

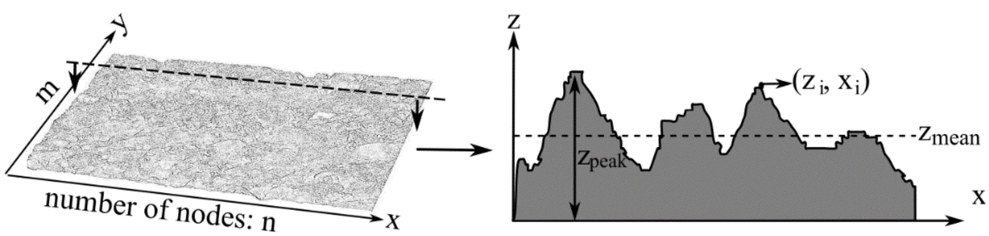


Figure 7. Surface texture parameters

In multi-scale surface characterization these parameters should be defined individually for each scale since they depend on the resolution (Moore, 1975, Do and Marsac, 2002, Ergun et al. 2005, Serigos et al., 2013). Instead of using different statistical parameters for each scale of texture, fractal techniques have been used for multi-scale characterization of pavement or aggregate surfaces; in which the surfaces are assumed to be self-affine. Such surfaces, when magnified still look the same as the previous scale. Figure 8 can show an example of self-affine surfaces in different magnifications.

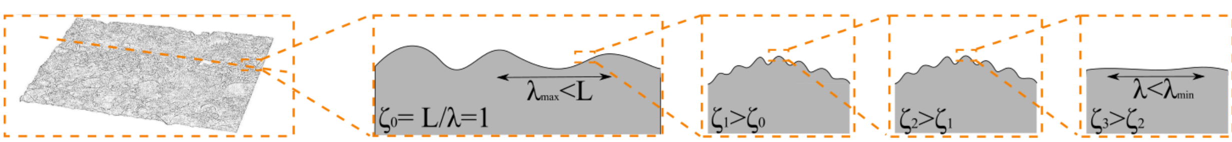


Figure 8. Self-affinity of pavement surface

Table 1. Statistical parameters for surface characterization

| Cat | Parameter | Description | Formula |
|---|---|---|---|
| i | $MPD$ | Mean profile depth | $MPD = z_{peak} - z_{mean}$ |
| i | $R_a$ | Arithmetic mean deviation of the profile | $R_a = \frac{1}{n}\sum_{i=1}^{n} \lvert z_i \rvert$ |
| i | $R_q$ | Root-mean-square deviation of the profile | $R_q{}^2 = \frac{1}{n}\sum_{i=1}^{n} (z_i)^2$ |
| i | $L_a$ | Average wavelength of profile | $L_a = 2\pi.\frac{R_a}{D_a}$ |
| i | $D_q$ | Root-mean-square slope of profile | $D_q{}^2 = \frac{1}{n}\sum_{i=1}^{n} (\frac{\Delta z}{\Delta x})^2$ |
| i | $L_q$ | Root-mean-square wavelength of profile | $L_q = 2\pi.\frac{R_q}{D_q}$ |
| i | Ssk | Skewness | $Ssk = \sum_{i=1}^{n} z_i{}^3\ (n\ R_q^3)^{-1}$ |
| i | Sku | Kurtosis | $Sku = \sum_{i=1}^{n} z_i{}^4\ (n\ R_q^4)^{-1}$ |
| i | SMTD | Simulated mean texture depth of an area | $SMTD = (\sum_{x=1}^{n}\sum_{y=1}^{m} z_{peak} - z(x,y))/(m\,n)$ |
| ii | $D_a$ | Arithmetic mean slope of profile | $D_a = \frac{1}{n}\sum_{i=1}^{n} \left\lvert \frac{\Delta z}{\Delta x} \right\rvert, \Delta z = z_{i+1} - z_i, \Delta x = x_{i+1} - x_i$ |
| ii | $\gamma$ | Profile slope at mean line | $\gamma = \frac{1}{n-1}\sum_{i=1}^{n-1} tan^{-1}(\frac{\Delta z}{\Delta x})$ |
| ii | SAR | Surface area ratio | $SAR = \frac{A - (m-1)(n-1)\ \Delta x\ \Delta y}{(m-1)(n-1)\ \Delta x\ \Delta y}$ <br> $A = \sum_{i}^{n-1}\sum_{j}^{m-1} A_{ij}$ <br> $A_{ij} = \frac{1}{4}(\lvert\overrightarrow{AB}\rvert + \lvert\overrightarrow{CD}\rvert)(\lvert\overrightarrow{AD}\rvert + \lvert\overrightarrow{BC}\rvert)$ |
| iii | S | Mean spacing of adjacent local points | $S = \frac{1}{n}\sum_{i=1}^{n} S_i$, $S_i$ is the space between adjacent peaks |
| iii | TAR | Texture aspect ratio | $0 < TAR = \frac{\text{The distance that the normalized ACF has}}{\text{The distance that the normalized ACF has}}$ <br> $\frac{\text{the fastest decay to 0: 2 in any possible direction}}{\text{the slowest decay to 0: 2 in any possible direction}} \leq 1$ |
| iii | $r_p$ | Mean radius of asperities | $r_p = \frac{2z_i - z_{i-1} - z_{i+1}}{l^2}$, where l is the length of the profile |
| iv | SBI | Surface bearing index of an area | $SBI = \frac{R_q}{H_{5\%}}$, $H_{5\%} = z$ at 5% bearing area |

Fractal parameters, such as fractal dimension D and Hurst exponent (H=3-D), can be representatives of all texture scales including micro-, meso-, macro-, mega-textures and roughness. In practice, there is always lower and upper length thresholds for self-affinity characteristic of a surface, in which in length scales more or less than those thresholds the surface cannot be considered as self-affine anymore. For pavement surfaces, this range can be from a few millimeters (equal to the size of the largest sand particle in asphalt pavements) to few micrometers as the lower threshold (Persson, 2001).

In the following a more detailed review on fractals will be presented.

### *Fractals*

In 1982 Benoit B. Mandelbrot proposed a novel idea of what he called "geometry of nature". He postulated that objects of any number of dimensions, up till then considered having irregular shape or texture, have in fact an inherent pattern of irregularity that repeats at all scales. This observation was a ground-breaking discovery and gave rise to a new extension of classical geometry - fractal geometry. Today fractal analysis (analyzing objects in search for their fractal nature) is applied to many fields of science, engineering, and arts, enabling humans to understand nature on a deeper level.

In this part the basic theories about fractals, their definition, types, and characterization methods are discussed.

### *Mathematical and descriptive definition of fractals*

A fractal is a pattern generated by the same geometric process repeated over and over which results in a never-ending, infinitely complex structure.

A fractal pattern gives impression of depth, due to inherent irregularity of boundary lines. This is the reason why fractals are described with fractal (Hausdorf) dimension, $D_H$, which in contrary to Cartesian dimension, $D_C$, can have any non-integer value. Fractal dimension of a fractal object is always larger than its Cartesian dimension (D=1 for a line, D=2 for a surface, D=3 for a volume, etc.):

$$D_H = D_C + (1 - H)$$

where, $0<H<1$ is the Hurst exponent, which accounts for the additional pattern of object's boundaries. The lower the value of Hurst exponent, the rougher the fractal object appears and the more additional dimension it fills.

### *Types of fractals*

There are many categories and applications for fractals, some of which are primarily used by mathematicians and physicists to describe chaotic behavior of variables, while others are used by producers to imitate nature on movie screens. In general, fractals are divided into self-similar and self-affine fractals.

Self-similar fractal object is an object approximately or exactly equal to a part of itself. Self-affine fractal object has pieces of itself scaled by different amounts in different directions. All self-similar objects are self-affine, while self-affine objects are usually not self-similar (Russ 1994).

### ***Types of fractal surfaces***

In physics, surfaces (as well as other objects) that exhibit an inherent pattern are classified as isotropic and anisotropic surfaces. Isotropic surfaces have the same physical properties in all directions. Anisotropic surfaces, however, have direction-dependent physical properties. Anisotropic surfaces can be divided into weak and strong. A Weak anisotropic fractal surface might visually look anisotropic, but when measured with fractal techniques it remains isotropic (same fractal dimension in all directions), e.g. isotropic surface stretched in one dimension. Strong anisotropic surface, however, has different values of fractal dimension in different directions (Russ 1994).

There are general equations for converting the fractal dimension of a profile to a surface such as:

$$1 + D_x \ \leq D_s \leq \ D_x + \ D_y$$

$$1 + D_y \ \leq D_s \leq \ D_x + \ D_y$$

where, $D_x$ and $D_y$ are estimates of fractal dimension is x and y directions and $D_s$ is the surface fractal dimension. For isotropic self-similar and self-affine surfaces, the left side of the inequality $(1 + D_x)$ is equal to $D_s$.

The inequality above is of high importance, because it enables one to describe (even if not exactly) a fractal surface when given only a single profile (or a small number of profiles).

### ***Fractal parameters***

#### ***i. Fractal dimension***

Fractal structures, when seen as signals (e.g. during analysis), are examples of fractional Brownian noises, described as a function $f(x) = ax^{g(D)}$, where variable x can be time in time domain or position in spatial domain, a is proportionality constant, and g(D) is a negative coefficient dependent on the structure (Jahn, Truckenbrodt 2004).

Based on this function, Power law methods are introduced for finding the fractal dimension. It must be noted that some of these laws are limited to self-similar fractals (e.g. Richardson), or one-dimensional data. However, some of them can be generalized to higher dimensions under some conditions (e.g. Minkowski, box counting, and power spectrum). Some of these laws are explained here:

**Richardson**

Richardson plot is one of the first methods that were developed for finding fractal dimension. It suggests that the total length of a fractal polyline changes with the size of length increment. When plotting the log-log plot of this relationship, it becomes linear with a slope of $\beta = 1 - D$. This method can be used for self-similar fractals only, as for self-similar fractals it gives incorrect estimations of D.

**Minkowski**

This method is a geometrical method involving circles covering the whole fractal line (one-dimensional fractal case). Log-log plot of radii of the circles versus area of the envelope the circles create around the line results in a straight line with a slope of $\beta = 2 - D$. One-dimensional Minkowski drawing is often called 'Minkowski sausage', because of the resulting shape. Two-dimensional Minkowski structure, with spheres covering a fractal surface, is called the Minkowski comforter. It can be used to both self-similar and self-affine fractals.

**Mosaic amalgamation and box-counting**

Russ, 1994, describes the mosaic amalgamation method as gradual coarsening of a fractal image. Treating each pixel as a square containing part of an image, and gradually merging neighboring squares, the sharpness and thus the total area and perimeter of objects in an image change. Log-log plot of total perimeter of depicted fractal structure versus side length of the square gives a line with $\beta = -D$. Box-counting is a common and simpler type of mosaic amalgamation, which is based on changing the size of a grid put on a picture. Similarly, the size of the depicted object changes with this change of resolution. Thus, the slope of the log-log plot of the number of covered squares versus the side length of the box has the same relationship with fractal dimension. The fractal dimension obtained from these methods, Kolmogorov dimension, is slightly different from Hausdorf fractal dimension. The two parameters approach the same value in the isotropic limit. Nevertheless, these approaches are widely used in studies of fractal surfaces and can be extended to three-dimensional fractal structures (by replacing the boxes by cubes).

**Power spectrum**

There are various techniques for estimating the power spectral density based on the available information, from non-parametric methods, e.g. periodogram or correlogram, to parametric methods, e.g. signal model beforehand. The former methods are less complex than parametric methods and rely on FT, FFT, or autocorrelation function. The non-parametric methods are either periodograms (Daniell method, Welch method, Bartlett method, etc.) or correlograms (spectral estimator based on covariance in the signal etc.). The first type includes a direct transformation of data while the second is an indirect interpretation of the signal.

In contrast to non-parametric methods for spectral estimation, parametric methods require an assumption to be made on the signal. They are model-based, which means that at the beginning of the analysis, a model for the signal that has a known functional form is generated, and the analysis consists of estimating parameters needed for the power spectrum based on the type of model (Stoica, Moses 1997).

A common method for finding power spectrum is using Fast Fourier transform (FFT). FFT divides the surface into combinations of magnitudes and their corresponding frequencies. PSD can be obtained by the log-log plot of the squared of the magnitude versus the frequencies. The slope of this graph has a linear relationship with fractal dimensions, for profiles, $D = \frac{5+\beta}{2}$, and for areas, $D = \frac{7+\beta}{2}$ (Bhushan et.al. 1992).

This method can be applied to both self-affine and self-similar data sets. It must be kept in mind that this method is precise for profiles, while for areas it tends to be slightly different from the Hausdorff dimension and it overestimates fractal dimension for D<2.5 and underestimates it for D>2.5. Different types of surfaces may give different deviations.

**Roughness-length (Malinverno)**

This method involves defining different windows along the main axis, starting from a window including the largest data point toward the minimum defined data points (e.g. ten). In each window, the part of the fractal structure is taken out of the picture and detrended (by e.g. subtracting a least-squares-regression line). Then the remaining root-mean-square (RMS) deviation is calculated as

$$RMS(\omega) = \frac{1}{n_\omega} \sum_{i=1}^{n_\omega} \sqrt{\frac{1}{m_i - 2} \sum_{j \epsilon \omega_1} (z_j - z_{av})^2}$$

where, $n_\omega$ is the total number of windows along the length, $\omega$, $m_i$ is the number of points, -2 in the equation stands for the two degrees of freedom which are lost by initial detrending. $z_j$ and $z_{ave}$ are the residual from the line and the mean residual in the *i*th window, respectively. Log-log plot of the relationship between RMS-roughness and length of the windows results in a linear line with $\beta = 2 - D$. This method can be used for self-affine data series, but is not extended for higher dimensions (Malinverno 1990, Russ 1994, Liang, Lin,et.al. 2012)

**Tessellation (Projective Covering)**

In this method, the surface is covered with different predefined grids. In each, the total area of the surface is calculated as a sum of areas of each square on the grid. Since the four corners of each square rarely lie on the same plane, the area of each square can be calculated as a sum of the two constituting triangles. After plotting the log-log plot of the total area for each grid size versus the grid size, the fractal dimension can be found based on the slope of the line, $\beta = 2 - D$ where slope, $\beta,$ is always negative, which means that the smaller the grid size, the larger the area.

This method is very similar to box-counting and Malinverno's roughness-length method, and can be count as an alternative cube-covering (extension of box-counting to 2D/3D structures). There are more variations of this method, e.g. triangular prism surface area method (pyramids instead of cubes or squares are used) (Xie,Wang,Stein, 1998, Zhou, Xie, 2003, Kwasny, 2009).

**Structure function**

The structure function was defined by Sayles and Thomas as for representing surface roughness in spatial domain (Sayles, Thomas 1977). It is defined as an average or expected value of the difference in elevation of two points in the profile as a function of their separation:

$$S(\tau) = \langle |z(x) - z(x+\tau)|^2 \rangle$$

where, z(x) is the profile elevation. The resultant $S(\tau)$ graph is a straight line (or a polygonal chain), whose slope is equal to

$$\beta = 2(2 - D)$$

By using approximate scaling-law structure function becomes

$$S(\tau) = K\tau^{\beta}$$

where, K is topothesy.

It is possible to extend the structure function to higher dimensions by using

$$S(\tau_x, \tau_y) = \langle \left| z(x, y) - z(x + \tau_x, y + \tau_y) \right|^2 \rangle$$

where, z(x,y) is the surface elevation. $S(\tau_x, \tau_y)$ obeys the same mentioned approximate scaling-law behavior as $S(\tau)$ (Kulesza, Bramowicz, 2014, Wu, 2000, Wu, 2001).

### *ii. Other fractal parameters*

In all of the methods described above only the relationship between fractal dimension and the slope of the log-log plots was mentioned. However, the slope is not sufficient enough to describe a unique fractal profile or surface. Therefore additional information is required, e.g. intercept of the line. This means that to describe a fractal structure, one has to define both the fractal dimension and amplitude of roughness, e.g. the constant of proportionality, a, in the aforementioned power law expression.

Several such constants are proposed in the literature, of which the most established ones are:

- Topothesy K (Russ 1994, Thomas,Rose,Amini 1999, Wu 1999, Kulesza, Bramowicz 2014),
- Scale constant G (Majumdar, Bhushan 1992),
- Proportionality factor C (Kwasny 2009), and
- Corner or critical frequency (Majumdar, Tien 1990, Wu 1999, Persson 2005).

### *Surface simulation*

There are two main approaches for generating a surface: (i) simulation of the surface from parameters related to the surface without using any actual data points (ii) interpolation between a limited numbers of points from measurements. A combination of these two approaches can also be used. Some of these methods which are able to generate self-affine fractals, and have fractal dimension value as one of the input parameters are presented in the following.

### i. Interpolation methods

To generate a surface, a continuous function must be found for interpolating between the data points. Apart from generating the original surface this method can be used to increase the resolution of the surface and model the smaller scale.

**Bivariate Fractal Interpolation Surface (BFIS)**

This algorithm generates a self-affine fractal surface and therefore can be useful for pavement surface simulation. The algorithm is a recurrent iterated function system (IFS), which differs from IFS by a stochastic element (probability factor). It is a generalized IFS for two dimensional self-affine structures. BFIS involves dividing a two-dimensional set of interpolation points into regions. Considering a subset including one or more regions, it can be divided into difference domains. Then, a contraction mapping can be determined, for mapping the endpoints of a domain to the endpoints of each region within the domain. To see a detailed mathematical description and derivation of BFIS, see (Bouboulis 2012)}.

## ii. Simulation methods

***Inverse Fast Fourier Transform (IFFT)***

Wu (Wu 2002) proposed several models of anisotropic surface, based on the classification of weak and strong anisotropy. This method of surface simulation is based on the Inverse FFT algorithm. Data points are computed as a sum of constituents resulting from the power spectral density of the surface.

$$z_{pq} = \sum_{k=0}^{M-1} \sqrt{P_{(x)_k}} e^{i2\pi[\phi_k + \frac{kp}{M}]} + \sum_{l=0}^{N-1} \sqrt{P_{(y)_l}} e^{i2\pi[\phi_l + \frac{lq}{N}]}$$

for $p = 0,1, \dots, M-1$, $q = 0,1, \dots, N-1$. $P_{(x)_k}$indicates the $k_{th}$ element of $P(x)$ (for discrete PSD), similarly $P_{(y)_l}$. Hence, in this method the power spectral density is an input. $\phi_l$ and $\phi_k$ are random phases, where k=0,1,2,…,M/2 and l=0,1,2,…,N/2. Another model was also presented for anisotropic surfaces

$$P(\omega_x, \omega_y) = \frac{G_x^{2D_x-2}\delta(\omega_y)}{\omega_x^{5-2D_x}} + \frac{G_y^{2D_y-2}\delta(\omega_x)}{\omega_y^{5-2D_y}}$$

where, $\delta$ is the delta function and G power scaling constant. It is possible to include the multi-fractal (scale-dependent) nature by defining two frequency thresholds, for which the PSD changes its slope (meaning the change of fractal dimension). For any direction not being one of the main x and y directions, power spectral density is a trigonometric function of the x and y PSDs.

***Blackmore anisotropic surface simulation***

This simulation method is used to generate a fractal surface profile as an anisotropic fractal model and it was proposed by Blackmore and Zhou (Blackmore, Zhou, 1998). It is a technique derived from Holder type condition that the surface has to satisfy, in which

$$\frac{|\Phi(X+h)-\Phi(X)|}{||h||^{3-s}} := \Theta(X,h)$$

is a positive continuous function bounded away from zero for small ||h||. Φ is the surface height and h is a small interval. The proposed surface model should satisfies this condition and its surface height is calculated as

$$\mathrm{z} = \Phi(\mathrm{x,y}) = \Phi(\mathrm{X}) = \alpha^{(s-2)} \sum_{n=1}^{\infty} \beta^{(s-3)n} \tau(\beta^n A(X) X + \Gamma_n)$$

where $\alpha > 0$, $\beta$ >1, and $2 \leq s < 3$ approaches the value of surface fractal dimension for large $\beta$s. $\tau$ is a continuous, piecewise smooth, doubly-periodic function and $A(X)$ is a smooth, 2*2 matrix-valued function. For detailed mathematical description of the model, see (Blackmore, Zhou, 1998).

### 2.2.2. Surface-texture measurements

There are a wide range of methods for surface surface-texture measurements of various surfaces such as pavement, mechanical parts, semiconductors and optics. These methods are different based on their type of evaluation, process, resolution and presence of contact between the device and surface. Nevertheless, none of them is well-recognized as the best mean for surface measurements. This review comprises the methods which have been used in pavement engineering and briefly addresses the available methods for other fields that have been validated in similar conditions. Currently, all of these methods are practical for measuring micro-texture profile of pavement surfaces in laboratory or low speeds but due to their high resolution and lack of required technology none of them can be used in highway speeds. Although, their improvements in recent years make the measuring techniques faster and more reliable, one of their major drawbacks is the time consuming process. These methods can be divided into two categories of contact probes and optic or contactless probes:

**1. Contact probe:**

The most common contact probe method which can give a quantitative measurement for surface micro-texture is stylus profiling device. These devices can have high resolution up to nano-scale. They are composed of a stylus, usually with a diamond tip of different sizes attached to a mechanical arm, which moves along a straight line and record the surface profile (Santos and Julio, 2012). The output of these devices is a 2D profile of the surface. There are also devices that can obtain 3D surface profile by measuring the surface in two perpendicular directions (Salah Ali, 2012). These devices are unable to capture a wide range of surface profile (similar to pavement surface) and usually they are limited to nano-scale and micro scale only, therefore they cannot be used for pavement surfaces measurements.

In pavement engineering, since it is believed that micro-texture is directly correlated with friction in low speed, friction measurements at low slip speeds have been used as qualitative methods for micro-texture measurements (Hall et al, 2006). The most common methods in this category are:

- **BPT:** British Pendulum number (BPN) is based on pendulum swing height of British Pendulum Test (BPT) and it is related to zero speed intercept of friction-speed curve ($\mu_0$) which characterize the friction in low speed. A high correlation was found between root mean square (RMS) of the height of surface micro-texture and $\mu_0$ of Penn State model by Pennsylvania State University; therefore, the BPN values are used as a surrogate for measurements of micro-texture (Henry and Leu, 1978, Stroup-Gardner et al., 2004).

- **DFT:** Dynamic Friction Tester measures the friction between the pavement surface and a rotating disc at 20 to 80 km/h speed under constant loading. Saito et al. (1996) demonstrated a strong relationship between BPN and the coefficient of friction of DFT. Hall et al. (2006) used DFT at 20 km/h (DFT20) as a surrogate for micro-texture.

## 2. Optical probe

In the last few decades, a wide range of optic devices for two and three dimensional digitizing have been introduced with various scales and applications. Optical techniques are based on the behavior of light in contact with a surface namely the angle of reflection of the light and the range of its scattering. These devices are contactless and therefore non-destructive. Also, they are usually faster than contact probes. But, usually they have the disadvantage of being sensitive to surface slope and small features, and multiple scattering in the deep valleys which can influence the accuracy of the device (Vorburger, 2006). Optical devices can be divided into different categories based on their measurement methods:

### 2.1. Laser scanners

Laser scanners project a beam of energy on the target surface. When the reflected beam hits the receiver sensor, the position of the target point can be obtained by trigonometric formulas and simple geometry. By obtaining the coordinate of all of the points, the 3D shape of the objects can be found. It should be considered that the magnitude of the reflected beam from the surface is related to the type of the surface. The difference between various devices and the resolution of the process can be defined by the laser spot size. Therefore, these devices are able to have high resolution from 1 micron to 0.01 mm based on their laser spot size. Also, due to this ability they can be used for multi-scale measurement of the surface (Do et al., 2000). In conventional laser scanners by increasing the field of view (FOV), the resolution and accuracy decrease. This problem is solved by synchronized scanning in modern devices. Laser scanners are not portable; therefore, they have limited application in-situ; Also they have high acquisition and maintenance cost.

Different types of these devices have been used in pavement engineering which some of these studies are presented here:

In 1986 Samuels utilized a laser sensor with a spot size of 0.1 to 0.2mm, but he was not able to find a significant difference in micro-texture of the surfaces (Do et al., 2000 and 2002). The Scanning Laser Position Sensor (SLPS) has been designed for obtaining topographic data of pavement surfaces specifically. Because of its portability, it can easily be used for in-situ measurement (Johnsen, 1997) but it is limited in measuring the full-range of texture. Do et al (2000) obtained micro-texture measurements by using laser and tactile systems with 0.001mm sampling interval. Li et al (2010) were able to obtain micro-texture measurements by using two laser scanners. Because of the low scanning speed and small spot size of 0.05mm, 1 kHz laser scanner was able to measure the micro-texture with 0.015mm resolution while 62 kHz laser scanner resolution was 0.031mm. Although 62 kHz scanner has lower resolution it can operate at relatively high speeds. Bitelli et al. (2012) used a triangulating desktop laser scanner with 650-nm resolution. Serigos et al (2013) utilized a laser texture scanner (LTS) for micro-texture data collection with resolution of 0.03 mm. They were able to scan an area of $25cm^2$ in 25 minutes in the field.

With the advance of technology, today, there are 3D laser scanners which are able to measure the surface with high resolution and accuracy in different scales and rather fast in comparison to previous devices. These scanners have been used by tire companies in their studies.

### 2.2. Image analysis

Image analysis systems obtain the surface texture by taking its photograph. Due to the development of technology and improvement of the resolution of the cameras, it became possible to measure the micro-texture of the surface with these systems. This method uses the following sequences: (a) illumination of the light over the surface (b) capturing the texture by the camera and feature extraction (c) computing and analysis (d) triangulation and obtaining the coordinates. One of the advantages of this method is its simplicity and one of the main problems is finding the common points among different image pairs when more than one camera is used.

This method has been used for pavement surfaces by taking pictures of cored samples in laboratory. In 1981 and 1989 Forster, deployed optical image analysis system for obtaining the surface micro-texture and finding the correlation between surface texture and skid resistance. In recent years developments in technology increased the precision and resolution of the process. In 2005 Ben Slimane et al. were able to measure the texture of pavement surface with 50 micron resolution by a methodology based on photometric image analysis and surface photometric model. Ergun et al. (2005) related surface friction to surface texture by using image analysis in micron scale. Masad et al. (2005) investigated the aggregate resistance to polishing. They characterized aggregate texture by using the Aggregate Imaging System (AIMS).

### 2.3. Microscopy

Microscopy can be divided in three categories of optical, electron and scanning probe microscopy. In all of these categories, a light or electron beam is diffracted and reflected from the surface and the scattered beams are gathered to obtain the image of the surface. The major advantage of this method is its high accuracy (up to 0.1 nano meter) and large vertical range up to some millimeters in some of the devices such as confocal microscopy (vorberger) Between optical and electron microscopy, the latter is more powerful since it uses electron beams and electrostatic and electromagnetic lenses of capturing the image of the surface while the other one uses visible light and lenses for magnification of the surface. (santos). The main disadvantages of the microscopic techniques are the time consuming process, the dimension, weight and non-portability of the devices, their high maintenance cost and sensitivity to light diffraction phenomena.

One of the most important microscopy techniques is the Scanning Electron Microscopy (SEM) which has been used in pavement engineering. In 1970, Williams and Lees and in 1971 Tourenq and Fourmaintraux obtained pictures by using Scanning Electron Microscope (SEM) and proved that SEM is effective in measuring the micro-texture of the aggregates (Rezaei et al., 2009).

There are some other methods such as structured light, interferometry which are able to measure micro-texture but they have not been used in pavement engineering.

## 2.3 FRICTION

Friction is a macro-scale empirical representation of a multi-scale deformation mechanism which results from three parallel phenomena; adhesion, hysteresis, and shear (Figure 9).

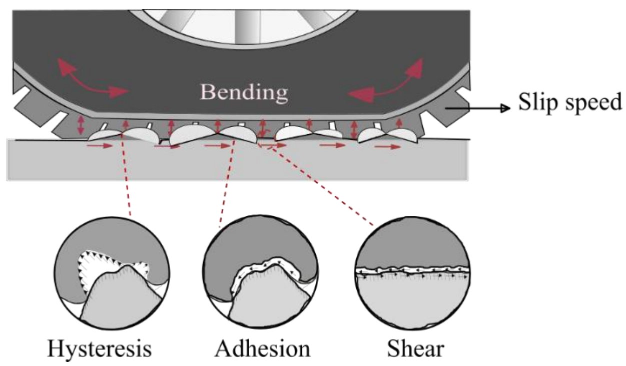

Figure 9. Friction mechanism

Adhesion is induced by interlocking and bonding of rubber compound to pavement surface. In the exposure of micro-asperities and irregularities of tire and pavement surfaces to each other, an attractive force due to Van der Waals or dipole forces keeps the two materials together and prevents their movements (Dewey2001, Persson1998). Adhesion is a function of the contact area and the shear strength of the contact surface (Hall2009).

Hysteresis, or internal friction, is a multi-scale phenomenon which highly influences the overall response of tires ranging from friction and noise to rolling resistance. It results from the viscoelastic response of the rubber material to the cyclic loading. Thus, the bulk deformation of the rubber and the deformation of the tire tread due to engaged texture yields hysteresis (Hall2009, Choubane2004, Lindner2004).

Defining the cascade of hysteresis in tire-pavement contact, three separate length-scales can be identified and associated to (i) tire deflection and bending, (ii) tread slip, and (iii) tread surface deformation (Bendtsen2004, Xiong2013).

The shear force of a rigid surface in contact with another material is small, and thus negligible. However, in the presence of a fluid scattered between the two surfaces, the shear force, which is mainly induced by the viscosity of the fluid, is more significant. The viscosity of water is less than snow, which leads to (i) lower shear forces in the contact area, and (ii) faster escaping rate of water from within the contact area and correspondingly smaller shearing contact area in comparison to the presence of snow. Therefore, the role of shear in friction between tire and rigid pavement is usually neglected except in the existence of snow (Hall2009). The contribution of friction components at different environmental conditions is depicted in Figure 10 (Hall2009).

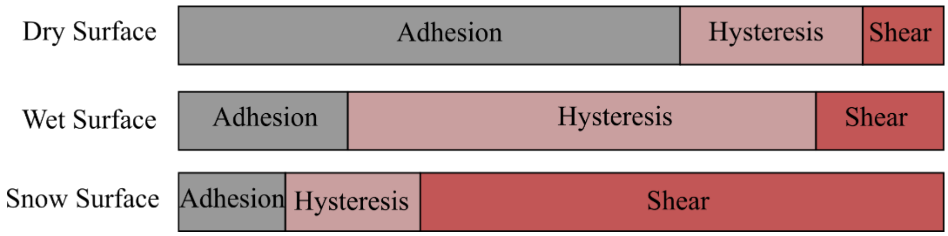


Figure 10.Compositions of Major influences on braking slip conditions (Hall2009)

Hysteresis is correlated to the volume of the deformed material and adhesion to the contact area (Kummer, 1966, Do, 2015). Therefore, these phenomena are governed by characteristics of the pavement surface, the tire properties, and the loading conditions due to environmental factors and vehicle performance (see Table 2).

In contrast to macro-texture, the contribution of micro-texture to adhesion is more significant than to hysteresis (Leu1978, Gandhi1991, Henderson2006, Hall2009). Nevertheless, there is a difference between the hysteresis of these two textures. The hysteresis of macro-texture contributes to rolling resistance and noise, in addition to friction (Bendtsen2004, Sandberg2003). However, the micro-texture mainly affects friction (Boere2009).

Table 2. Important factors in pavement friction (after Hall et al., 2009)

| **Pavement surface characteristics** | **Vehicle Operating Parameters** | **Tire Properties** | **Environmental factors** |
|---|---|---|---|
| ▪ **Surface-texture**<br>▪ **Material properties**<br>▪ Temperature | ▪ **Slip speed** **(**Vehicle speed, Braking action)<br>▪ Driving maneuver (Turning, Overtaking) | ▪ **Tread design and condition**<br>▪ **Inflation pressure**<br>▪ Tire Foot print<br>▪ Rubber composition and hardness<br>▪ Load<br>▪ Temperature | ▪ Climate (Wind, **Temperature, rainfall and condensation , Snow and Ice)**<br>▪ **Contaminants** like: Anti-skid material (salt, sand), Dirt, mud, debris) |

Note: Critical factors are shown in bold.

Beside the surface texture, the friction depends on other factors among which sliding velocity, temperature, normal load, and presence of contaminations are the most prominent ones. In the following, the influence of these factors on the contribution of surface texture to friction will be discussed. These factors are not necessarily independent of each other.

The velocity of the vehicle influences the role of surface texture in friction by affecting the viscoelastic behavior of the tire.

In tire-pavement interaction, two velocities of free rolling (static) and sliding velocity during cornering or ABS-braking (kinetic) are involved. The velocity of rolling tire directly influences the viscoelastic properties of the rubber. As the velocity increases the rubber becomes stiffer. Therefore, the contribution of different surface textures in friction varies with vehicle speed and the deformation rate (Persson2001). The influence of micro-texture on friction is more at lower speeds (soft tread) while the one of macro-texture is more at higher speeds (stiff tread) (Dewey2001, Hall2009). The changes in the engagement of textures affect the contact area between the tire and the pavement surface and thus the friction coefficient. At higher velocities, the contact area decreases due to the reduction of the engaged texture (Persson2001).

Temperature affects the viscoelastic properties of the rubber, similar to velocity. The tire pressure increases with temperature and consequently, the area of contact and the friction decreases (lin2004temperature, muller2003).

Bazlamit et al, (Bazlamit2005) suggested that the decrease in hysteresis due to the increase in temperature occurs in all surfaces with different textures. But, the effect of surface texture on adhesion is more dominant in comparison to temperature. However, there are still some challenges in understanding the effect of temperature on the friction (Flintsch2012) since the temperature in friction measurements are influenced by friction test method, pavement type, and climate (Lu1971).

Considering the effect of normal load on friction, increasing the load leads to an increased contact area due increase in the engaged texture. Whilst, the rate of penetration is defined by the rubber stiffness (kluppel2003). The relationship between the applied load and the contact area is the topic of many recent theoretical studies (heinrich2008, Persson2001, persson2002, heinrich2000). Most of the available theories define this relationship to be linear when the contact area in comparison to nominal contact area is small. As the load increases the area approaches to the nominal contact area in a continuous manner (Persson2006).

However, representing the contact to be similar to the real contact between a solid and a rough surface, and also considering the coupling of adjacent asperities under a reasonable load has been a challenge (archard1957, Greenwood1966, Bush1975, Persson2006). Such a relationship has been developed by Persson (Persson2001).

Contaminations also influence the role of surface texture in friction. As an example, in the presence of water the contact zone is divided into three zones: (i) tire lifting zone, (ii) thin water film zone, and (iii) full contact zone (Figure 11) (Moore1975). Since the friction force is only generated in the full contact zone, there is a reduction in friction due to the decrease in contact area. Surface micro- and macro-texture along with tire tread help the water to escape through the contact surface and therefore they could increase the contact area (Do2015). At high speeds, the available time for water evacuation decreases, thus, the loss of friction becomes more significant. If there is no contact maintained between the tire and the surface, aquaplaning[1] occurs.

[1] Aquaplaning occurs when enough water is trapped under the tire tread at high speeds to detach the entire tire tread from the pavement surface.

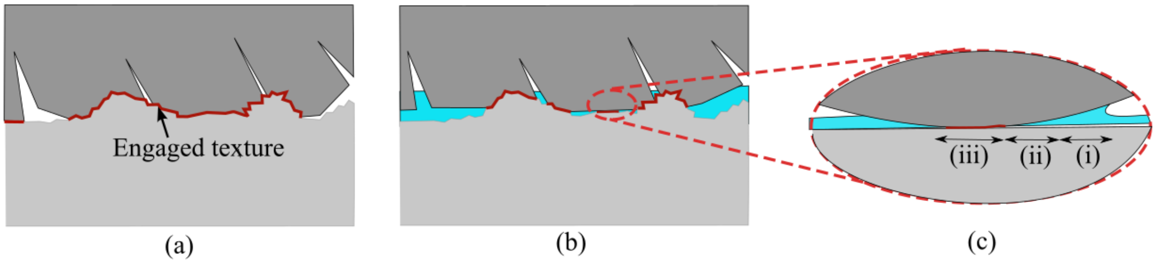


Figure 11. Effect of water presence on contact area (a) contact without water, (b) contact in presence of water, and (c) contact zone

Similarly, other contaminants (such as dust and dirt particles) decrease the friction because they prevent the contact between the tire tread and the smallest micro-textures of the surface. This effect is more significant on adhesion component since the influence of micro-texture on adhesion is more dominant than hysteresis. Therefore, adhesion is usually assumed to be important on clean and relatively smooth surfaces (Persson2001). It worth mentioning that in presence of detergents the friction coefficient is even less since they prevent the direct contact at the interface (roberts1971).

Grosch (Grosch1963) investigated the effect of dust, water and detergent on friction coefficient as depicted in Figure 12.

### 2.3.1. Friction Measurements

Friction measurement devices are founded on the principle of rubber sliding over the wet surface and the measurement of the resistance force. These devices follow different measurement mechanisms depending on the type of the measured friction force, the performance speed, and the slip ratio of the tire. The two different frictional forces measured with these devices are (i) longitudinal and (ii) lateral frictional forces, which help the driver to control and maneuver the vehicle safely. The longitudinal forces occur between the tire and the pavement surface when it is moving in the longitudinal direction in the free rolling or constant-braked mode. The lateral friction forces occur when the vehicle is changing direction or moving on a cross-slope road or facing a cross-wind effect.

Most devices are capable of measuring friction at various speeds up to highway limit. Some of them can even perform in variable slip ratio of the tire. Other factors can also influence the friction measurements, such as tire loading, size, tread design and construction, and inflation pressure. For controlling these tire-related factors standard tires are used after ASTM E501.

So far, there is no well-accepted universal friction measurement approach. The popular approaches vary depending on the region (Wallman2001). Here, the most popular friction measuring devices are reviewed.

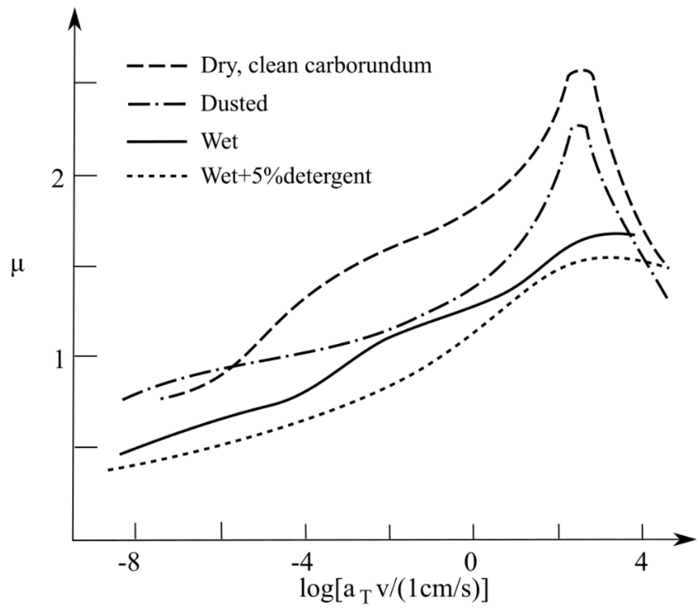


Figure 12. The kinetic friction coefficient for rubber sliding on a carborundum surface under different conditions (Grosch1963)

**i. Stationary devices**

The two devices that are used commonly for friction measurement at low speeds (which require the traffic to stop) are British Pendulum Tester (BPT) (AASHTO T 278 or ASTM E 303) and the Dynamic Friction Tester (DFT) (ASTM E 1911). In these devices, a slider (pendulum or rotating disc) slides over the pavement surface at a specific speed. The friction between the slider and the surface forces the slider to slow down. This friction is then measured tracing the dissipation of the kinetic energy of the slider which is governed by a decrease in the momentum of the pendulum or the disc (Hall2009). A good agreement has been found between the coefficient of friction of the DFT and the British Pendulum Number (BPN) at different speeds (Saito1996). The results of these methods are usually attributed to micro-texture of the surface because the effect of micro-texture on friction is more dominant at lower speeds.

**ii. Pulling devices**

The friction measurement devices which can work at higher speeds are mostly categorized in four groups of locked-wheel, fixed-slip, variable-slip and sideway-force or cornering mode. The locked-wheel devices measure the friction when the tire is moving in the vehicle direction, the wheels are locked and the slip ratio is 100%. The friction in fixed-slip devices is measured in vehicle direction and constant slip ratio up to 20%, similar to anti-lock braking condition. The variable-slip devices are capable of measuring the frictional force at predetermined slip ratios in vehicle direction. In sideway-force devices, there is a constant angle between the tire and the vehicle direction which is necessary to assess the rotational resistance and the controlling ability of the vehicles in curves at constant slip ratio (Nordstroem1998).

Among these devices locked-wheel (ASTM E 274) is widely used in the U.S. (Choubane2004). It characterizes the friction by a friction number (FN) that depends on the tire velocity, the horizontal and the vertical loads and the friction coefficient (Henry2000, Hall2009).

Despite being popular, locked-wheel devices have limited performance due to the required long distance between two readings. These devices provide only one reading of friction over a long distance. Also, the locked-wheel condition is not a proper representation of the braking condition of the current vehicles equipped with ABS systems. Therefore, continuous friction measuring equipments (CFME) (ASTM E2340) as slip-wheel devices (fixed-slip or variable-slip) are more preferable, e.g. Grip tester (najafi2015). These devices can measure the friction in higher frequencies and operate similarly to the ABS systems with a critical slip ratio of 10-20%. However, still, the current CFME devices are not able to measure the lateral friction at curves.

The ability of these devices to measure the friction at various speeds, is useful for investigating the effect of velocity on friction (Hogervorst1974, Noyce2005, Matilainen2012). At higher speeds, friction is mainly governed by hysteresis while at lower speeds, it is governed by adhesion (Masad2009). Accordingly, it could be possible to find the contribution of hysteresis and adhesion by performing friction test at different speeds.

The main limitation of the high-speed friction measurement devices is the consumption of a large amount of water for wetting of the surface (Ueckermann2015). Therefore, in the more recent friction measurement devices, the focus is on reducing the amount of required water as much as possible. The presence of water affects the measurements by reducing the engaged texture. Moreover, other factors such as temperature, speed of measurement, and age and wear of the rubber can affect the friction measurements, while being difficult to control during the measurement process. To address these limitations, the concept of contactless friction measurement based on optical texture measurements has been introduced. The method relates the surface texture measurements to the friction of the surface (Dunford2008). They are founded on the current friction prediction models based on surface data.

The tests presented here, evaluate friction by a friction coefficient or friction number, as a function of speed and tire load. Many equations have been developed by different studies to define the correlation between friction numbers and various factors such as surface texture, velocity, and temperature (Lu1971, Bazlamit2005, Hall2009). Some studies developed models to correlate the results of different tests. Some of these correlations are presented in Table 3.

A schematic comparison of the pavement friction devices and their mechanisms are presented in Figure 13.

Theoretical studies on rubber-surface contact characterization use different devices to measure the friction. Lorenz et al. (lorenz2011) developed a new instrument for validating their friction theory. It included a rubber block attached to an aluminum plate and a rough surface moving with a specific speed. A tension and compression load cell was used to measure the friction force in the interface. They used this device for measuring friction on concrete (lorenz2011) and asphalt (lorenz2013) surfaces.

Table 3. Correlation between different friction test results

| Friction coefficients | Correlation | Validation | Author |
|---|---|---|---|
| **BPN and DFT** | DFT=0.0078 BPN | R=0.97 | Steven_-2009 |
| | BPN=57.9 DFT+23.1 | R=0.86 | henry2000 |
| **BPN and SN** | $SN_{40}$= 0.862 BPN – 9.69 | ----- | Kissoff1988 |
| | $SN_0$=1.32 BPN-34 | R=0.95 | henry1983 |
| **BPN and CST** | BPN=179.67 CST | R=0.99 | Steven_-2009 |
| **SN and Mu** | $Mu_{40}$=1.21 $SN_{40}^{a}$-14.9 | R=0.99 | burns1973 |
| | $Mu_{40}$=2.14 $SN_{40}^{b}$-17.8 | R=0.92 | burns1973 |
| **SN and SFC** | $SFC_{50}$=0.388 $SN_{80}^{1.425\ c}$ | R=0.93 | Henry1986 |
| | $SFC_{50}$=1.52 $SN_{80}^{d}$-1.4 | R=0.9 | Henry1986 |

BPN: British pendulum tester, DFT: Dynamic friction tester, SN: Locked-wheel ([a] New Mexico Locked-Wheel, [b] California Locked-Wheel, [c] Stuttgarter Reibungsmesser, [d] Skiddometer BV 8), CST: California Skid tester (Stationary device), Mu: Mu Meter (Side-force), SFC: SCRIM tester (Side-force)

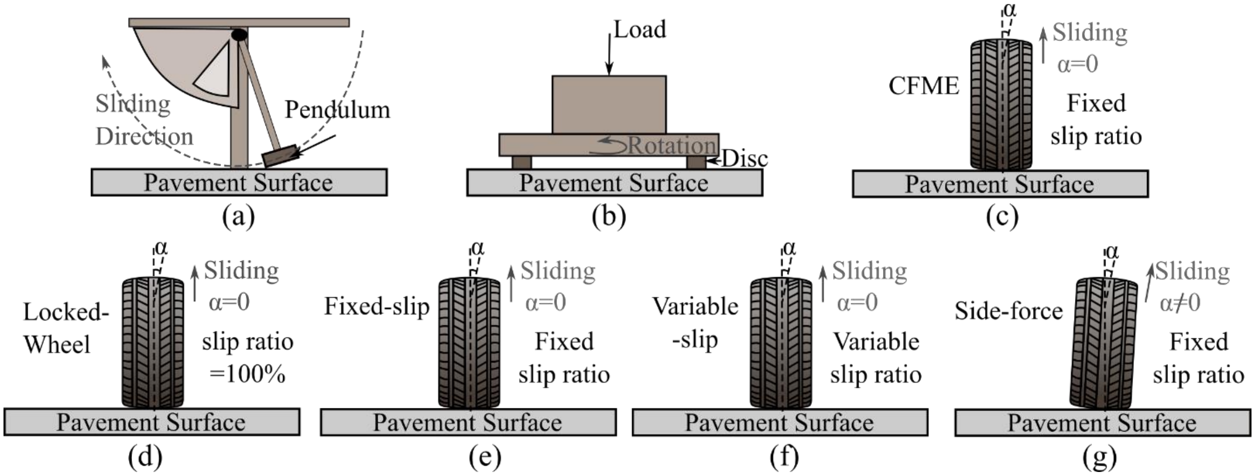


Figure 13. Friction measurement devices: (a) BPT (b) DFT (c) CFME (d) Locked-wheel (e) Fixed-slip (f) Variable-slip (g) Side-force

### 2.3.2. Texture-Friction Relationship

Friction coefficient, $\mu$, has long been known to be a function of the texture and adhesion of the contact surface (williams1955). On the smooth surfaces, the friction coefficient can be attributed to adhesion. On the rough surfaces, $\mu$ is attributed to deformation and hysteresis. In most of the existing studies the adhesion and hysteresis components of friction have been studied separately. While the surface texture directly influences the hysteresis, its contribution in adhesion is limited to the increase in the nominal surface area.

In pavement surface, micro- and macro-texture both affect the hysteresis, and consequently friction. While there are few models that can correlate the friction to the texture, it remains a challenge to define the exact geometrical parameters that contribute to friction.

The complexity of tire-pavement interaction, lack of detailed texture profiles, and in compatibility of tire and pavement models makes the development of a multi-scale contact model for predicting the pavement friction difficult (Li, 2005). Existing contact models are mostly phenomenological and can be divided into three categories (i) tire models, (ii) theoretical contact models, and (iii) empirical or semi-empirical models.

### *Tire Models*

Different tire models have been used for evaluation of friction performance of tires which is specifically important for braking. The models range from classical spring-damper models to detailed three-dimensional finite element (FE) models. The FE models can contain the non-linearity, incompressibility, large deformation and composite structure of the tires, but each execution may take several days. However, concurrent multi-scale FE simulations are able to calculate the tire deformation along with the interaction of its components at different scales (Wang, 2013). FE models generally consider different parts of a tire (Figure 14) and include several design and operational variables like deflection, pressure, load, and speed.

So far, existing tire models barely consider the effect of pavement surface texture. Similar scenario exists for pavement models. Therefore, further reviewing of the tire models is not presented here.

A comprehensive literature review on tire models has been done by Ghoreishy (Ghoreishy, 2008).


Figure 14. Various parts of a detailed tire model

### *Theoretical Friction Models*

Theoretical contact models can be categorized into three main groups; (i) single-asperity, (ii) multi-asperity, (iii) multi-scale fractal models. The **single-asperity models** (Greenwood, 1958, Ford, 1993, Sabey, 1958, Hui, 2000) consider the rough surface as simple triangles or spheres. They cannot consider the effects of multiple contacts between two surfaces. The assumption is true only when (i) the area of effective contact is considerably smaller than the one of the nominal contact, and (ii) the distance between adjacent asperities is so large that no mutual interaction exists (Persson, 2006). Here, the friction coefficient is mostly considered as a function of the pressure in the contact area or the contact angle. There is a linear relationship between the friction coefficient $\mu$ and the applied pressure up to a certain pressure. For pressures higher than that, the friction will be underestimated (Do, 2015).

**Multi-asperity models** (Bush, 1975, McCool, 1986, Thomas, 1998, Golden, 1981) consider that the contact occurs at more than one asperity, and thus are more reliable than single-asperity models. The original concept was introduced by Greenwood and Williamson in 1966 (Greenwood, 1966). The models cannot take into account the cases where there is the high penetration of the pavement into the rubber, since they do not consider the effect of rubber entrapment. Accordingly, the models are valid only when the ratio between effective and nominal contact area is small (Carbone, 2008).

**Multi-scale contact models** have been extensively studied in the past two decades. **Kluppel and Heinrich** (Kluppel, 2000) introduced a theoretical concept for relating the frictional force to the dissipated energy of the rubber during sliding on a self-affine surface (Figure 15).

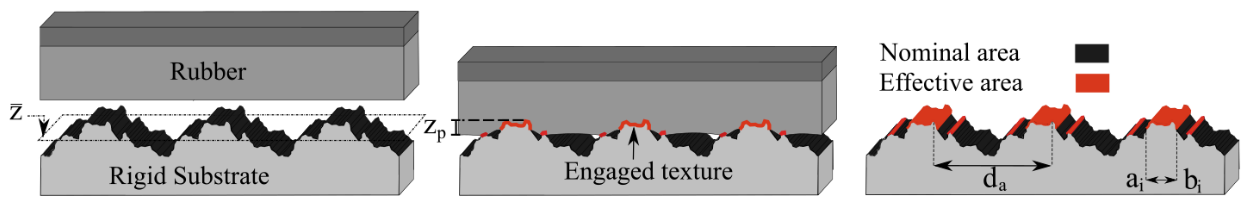


Figure 15. Contact of rubber with a rigid substrate as pavement

The surface was described by three shape-descriptor parameters; fractal dimension, $D_f$, and the correlation lengths parallel, $\xi_{\parallel}$, and normal, $\xi_{\perp}$, to the surface. Defining the friction coefficient $\mu$ as the ratio of resisting force to the normal force, it was given as

$$\mu = \frac{1}{4}(\frac{\xi_{\perp}}{\xi_{\parallel}})^2 \left(\frac{E"_{max}}{E'(\omega_{min})}\right) \arctan(\frac{(v_1 - v_2)v}{v^2 + v_1 v_2})$$

Here, $E'(\omega_{min})$is the storage Young modulus of the rubber corresponding to the minimum frequency of PSD of the surface, $\omega_{min} = \frac{2\pi v}{\xi_{\parallel}}$. $E"_{max}$ is the maximum loss modulus. To simplify the equations, the characteristic coupling velocities $v_1 = \frac{\xi_{\parallel}}{2\pi\tau_z}$ and $v_2 = \frac{\lambda_{min}}{2\pi\tau_z}$ were defined, where $\tau_z$ is the rubber relaxation time and $\lambda_{min} = \frac{L}{\xi_{max}}$ is the lower cut-off wavelength. The results of this model were validated by the classical friction data of Grosch (Grosch1963).

**Persson theory** of friction describes the energy dissipation of a perfectly elastic rubber layer with respect to the internal friction (Persson, 2001). In contrary to the theory of Kluppel model, Persson theory is three dimensional and has been hired as a base concept in several models (Heinrich, 2008, Ueckermann,2015). The theory mainly takes the hysteresis component of friction into account and exclude adhesion. Such an approach is relevant for rough or wet surfaces where adhesion has a negligible contribution to friction. Therefore, despite using a simplified assumption, the model provides a good representation of tire-pavement friction in most cases. The friction coefficient, $\mu$, is defined with respect to the rubber vibration frequency induced by the surface texture as

$$\mu = \int_{q_L}^{q_1} q^3 C(q) R(q) dq \times \int_0^{2\pi} \cos(\phi)\, Im\ \frac{E(qv\cos(\phi)}{(1-\upsilon^2)P} d\phi$$

In which $q_L = \frac{1}{\lambda_{max}}$ and $q_1 = \frac{1}{\lambda_{min}}$ are the lower and upper boundaries of wave number, q. $R(q) = \frac{A_{eff}}{A_{nom}}$ is the ratio of effective and nominal contact areas that are governed by spectral density, C(q), contact pressure, P, sliding speed, $v$, and rubber moduli, E, and Poisson ratio, $\upsilon$.

The model has been later advanced to take into account the roughness of both rubber and pavement surface (Scaraggi, 2015). Some other studies used the model to investigate the energy dissipation at opening cracks and shearing in thin viscous film (Lorenz, 2011), a way to reduce the static friction (Lorenz, 2012), and friction on ice (Persson, 2015, Lahayne, 2016).

**Pinnington model** used a dynamic stiffness approach to describe the hysteresis energy loss during friction due to contact with axisymmetric asperities with radius $\Delta$ (Pinnington, 2009). He used ideal peak shape surfaces as a single asperity contact and generalized the model to consider different surfaces such as periodic array of identical peaks, randomly distributed identical peaks in one or multiple scales. The friction force, here, depends on the contact length at different slip speeds, as a function of $\Delta$, and the slope of the peak at the contact line, $\frac{dz_{x=\Delta}}{dx}$. The friction coefficient is then defined as the mean slope of the contact, expressed as $\mu = \sin(G)(\frac{dz_\Delta}{dx})$, where G is the complex shear modulus. For a surface expressed by Fourier transformation, friction coefficient is given as

$$\mu = \sin(G)(\frac{dz_\Delta}{dx}) = -\sin(G)\int_0^\infty \frac{P_q \sin(q\Delta)}{|G|} dq$$

In which q is the wave number and $P_q$ is the Fourier transform of contact pressure distribution. .

The model was validated with measurements of Grosch (Grosch1963).

Using computational resources, residual molecular dynamics (RMD) simulations has been extensively used recently to explore rubber contact mechanics problems. While being numerically expensive, the simulation provides a detailed insight into different mechanisms involved in contact problem. The flexibility of simulation approach provides an excellent interface for validation of models, since the simulations can be validated by experiments and then be used for validation of theoretical models. The RMD method was also used to study the friction between a solid and a rough surface. In such studies the energy dissipation during sliding of a viscoelastic material on a rough surface and the adhesive contribution to friction were investigated (Scaraggi, 2015, Scaraggi, 2016).

So far, only the models considering the hysteresis component of friction have been discussed. These models are applicable for micro-texture of the surface as well as macro-texture. However, in dry or poorly lubricated contacts, adhesion is also present due to the molecular interaction between the two surfaces. In the presence of adhesion, the breakage of the adhesive bonds in the contact interface in addition to adhesional friction, can also cause adhesional hysteresis. While few studies have incorporated the effect of adhesion into the contact problem (Carbone, 2015, Busse, 2010), it remains a challenge to describe the friction as the result of concurrent hysteresis and adhesion mechanisms.

***Theoretical Adhesion Models***

If loading and unloading process occurs at a very low speed, rubber can be assumed elastic. Thus, some studies employed adhesion theories for elastic materials for the contact between rubber and rough surfaces (Carbone, 2004, Carbone, 2012, Persson, 2014). Among the existing elastic theories for adhesion, DMT theory (Derjaguin, 1934) and JKR theory (Johnson, 1971) have been used for this contact. In DMT theory, adhesion is considered as a force applied to the solid in addition to the normal force. The contact area is then defined by the classic theory of Hertz (Hertz, 1881). This theory includes the adhesion in non-contact zones near to the contact zone as well as the contact area and is valid for elastically hard solids which are weakly interacting with each other. However, in JKR theory, the adhesion is only limited to the extent of the contact area and the adhesional energy is defined as $U_{adh} = \Delta\gamma A$. In which $\gamma$ is the work of adhesion, which represents the required energy for separation of a unit area of the interface between two materials. This theory is valid for elastically soft solids which are strongly interacting with each other. Here, the deformed shape of the solids after the contact can be calculated by minimizing the total energy, sum of adhesional and elastic energies $U_{adh} + U_{el}$.

**Carbone model** (Carbone, 2004) is based on JKR theory and it considered the penetration of an elastic rubber layer into a fractal rigid surface. The hysteresis loop induced by a randomly rough adhesive contact was investigated. The total energy was defined as the sum of adhesion and elastic energies. The adhesion energy was obtained from

$$U_{adh} = -\gamma \sum_{i=1}^{n_c} \int_{a_i}^{b_i} \sqrt{1 + [z'(x)]^2}\, dx$$

where $\gamma$ is the work of adhesion. $z'(x) = z - \bar{z}$ is the height of the profile measured from its mean plane. $n_c$ is the number of contact regions and $a_i$ and $b_i$ are the limit lengths of each contact (see Fig. ). They found that the contact area has a linear relationship with the work of adhesion (Carbone, 2012).

Busse model (Busse, 2010) described friction coefficient as the summation of individual contribution of hysteresis, $\mu_{hys}$, and adhesion mechanisms, $\mu_{adh}$. Accordingly,

$$\mu = \mu_{hys} + \mu_{adh}$$

Here, the hysteresis friction is given by describing the surface by two different fractal dimensions, dividing it into two scaling ranges, expressed as

$$\mu_{hys} = \frac{< \delta >}{2Pv} (\int_{\omega_{min}}^{\omega_2} E"(\omega) C_1(\omega) \omega \, d\omega + \int_{\omega_2}^{\omega_{max}} E"(\omega) C_2(\omega) \omega \, d\omega$$

where $\delta = b.z_p$ is the mean excitation depth in which b is a fitting parameter. $C_1$ and $C_2$ are the PSDs in two different scaling ranges, namely $\{\omega_{min}$-$\omega_2\}$ and $\{\omega_2$-$\omega_{max}\}$.

Adhesion friction coefficient was defined as the ratio between the adhesion force $F_{adh}$ and normal force $F_N$.

$$\mu_{adh} = \frac{F_{adh}}{F_N} = \frac{\tau_s A_{eff}}{P A_{nom}}, \qquad \tau_s = \tau_0 (1 + \frac{E_{inf}/E_0}{(1 + \left(\frac{v_c}{v}\right))^n}$$

where $\tau_s$ and $\tau_0$ are the interfacial shear stress at $v$ and 0 velocities, respectively. $E_{inf}$ and $E_0$ are long term and instantaneous elastic moduli. Here, $v_c$ is the critical velocity where the shear stress is at maximum, and n is related to the exponent of the relaxation time spectra of the elastomer.

Persson and Scaraggi, (Persson, 2014), investigated the effect of surface roughness on adhesion between two elastic solids, implementing JKR and DMT theories into Persson theory of friction. They verified their theory results with exact numerical calculations using RMD.

### *Empirical Models*

Empirical modeling is another popular approach to describe the correlation between the texture of the surface and friction measurements through fitting of the results to pre-assigned formulas. Micro-texture and its role in friction is often neglected in empirical models of friction since most of the shape descriptor parameters considered in empirical models cannot detect micro-texture. For many parameters listed in table 1, micro-texture presence only results in micro-variations in their magnitudes. Therefore for inclusion of micro-texture effect, its characterization should be implemented separately.

In 1978, Dahir and Henry (Dahir, 1978) proposed the first empirical model that incorporated micro texture into friction by using BPN values as a surrogate for micro-texture. While their study suggest the existence of a correlation between friction and micro-texture, they could not formulate it (Luce, 2006). The relationship between BPN and surface texture has been the focus of several studies (Forster, 1989, McLean, 1998, Do, 2000, Do 2002, Ergun, 2005, Serigos2014}, and BPN was found to be governed by both micro- and macro-texture (see Figure 16) (Serigos, 2014).

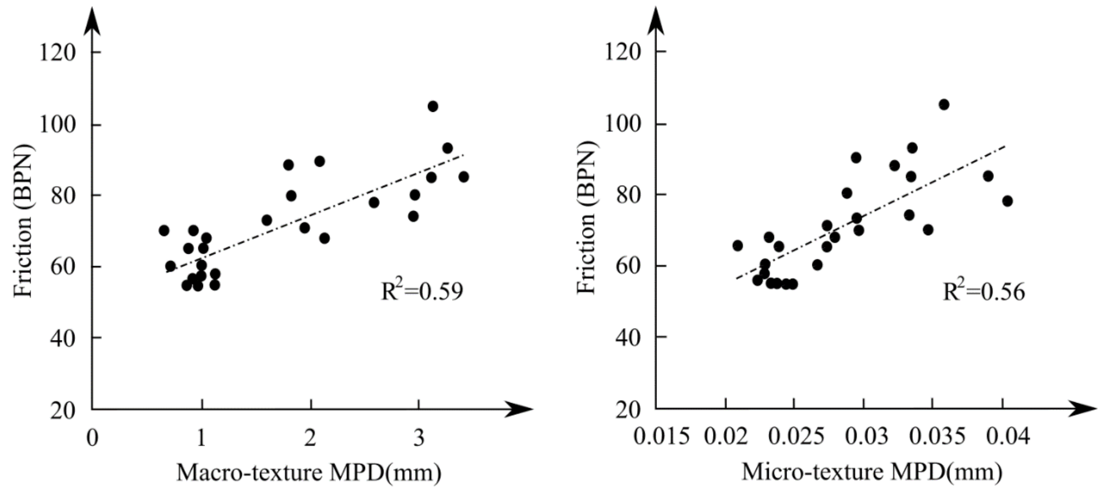


Figure 16. Relationship between Skid resistance and Macro- and Micro-texture (Serigos, 2014)

In another approach, Kokkalis and Panagouli (Kokkalis, 1998) described the friction at 40 mi/h $SN_{40}$, with respect to micro-texture as

$$SN_{40} = \frac{9.4m \times \bar{z} - 38}{4.25 \times d_a^{0.1} e^{\left(\frac{0.14}{\bar{z}_{macro}^{0.72}}\right)}}$$

where $\bar{z}_{macro}$ is the average macro-texture depth expressed in millimeters and $d_a$ is the distance between adjacent asperities. Later, Kokkalis et al. (Kokkalis, 2002) suggested that SN values are directly correlated to the fractal dimension (Figure 17).

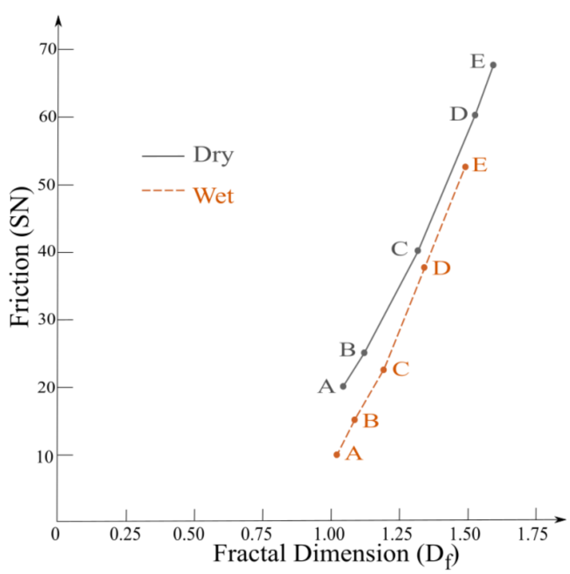


Figure 17. Correlation between the fractal dimension and the friction for dried and wet surfaces (Kokkalis, 2002)

Ergun et al. (Ergun, 2005) presented a model to correlate friction coefficient and surface texture as follows

$$\mu(s) = (0.37 + \frac{0.11}{MPD_{mac}} + \frac{0.15}{La_{mic}}) \times e^{(\frac{s}{149+91\log(MPD_{mac})+80\log(Rq_{mic})})}$$

where s is the slip speed and $MPD_{mac}$ is the mean profile depth of macro-texture. Here, $La_{mic}$ and $Rq_{mic}$ are the average wavelength and the root-mean-square of micro-texture, respectively. They suggested the average wavelength of the profile as the most reliable texture parameter for predicting the friction coefficient at no slipping.

Recently, Kanafi et al. (Kanafi, 2014) have extensively studied the correlation between friction and the fractal and non-fractal surface parameters. They found that none of the current fractal parameters can be considered to be directly correlated with the friction (seeFigure 18Figure 18).

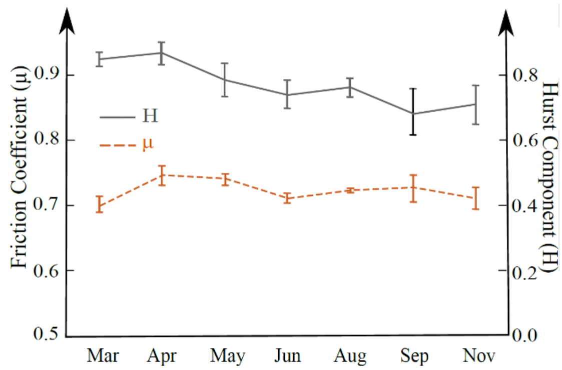


Figure 18. Friction variation relationship with Hurst exponent

Noyce et al. (Noyce, 2005) demonstrated the variation of wet skid resistance of pavement in different speed by changing micro or macro-texture, while keeping the other factor constant, as illustrated in Figure 19. On the basis of these results, it can be concluded that the need for adequate macrotexture does not reduce the need for high micro-texture in pavement surfaces. Both textures contribute to the wet friction although their magnitudes vary with speed (Noyce, 2005).

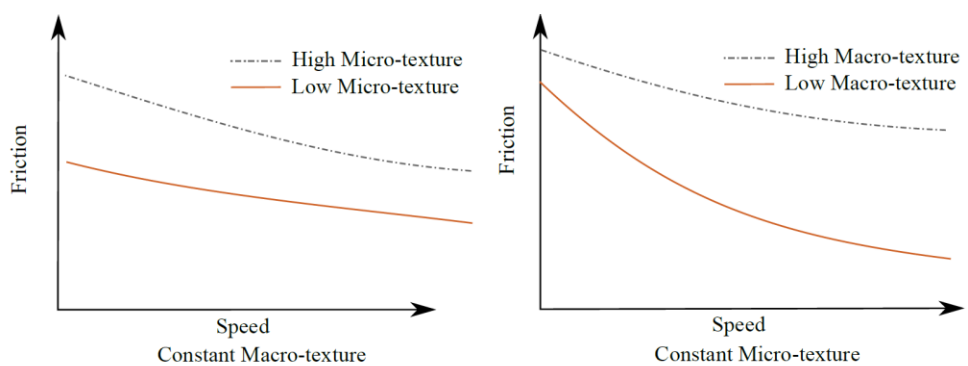


Figure 19.Wet skid resistance versus speed for constant (a) macro- and (b) micro-textures (Noyce, 2005)

Micro-texture plays a significant role in tire-pavement friction particularly in low speeds, and has to be understood (Forster, 1989, Serigos, 2014). Moreover, there has been very limited efforts on coupling of existing tire and surface models together. Since the influence of both elements on friction is evident, such efforts are necessary for thorough understanding of friction mechanism.

## 2.4 INFLUENCE OF PAVEMENT PROPERTIES ON ROLLING RESISTANCE

Rolling resistance is the required force for keeping an object such as a wheel or tire moving. Similar to friction there are different factors affecting rolling resistance (e.g. surface and tire characteristics, tire operating and environmental conditions). It occurs because of the energy loss or stress-strain hysteresis due to tire deformations and it is characterized by viscoelastic response of tire material. It consists of three components which act at different scales; (1) tire deflection and bending, (2) tread slip and (3) tread surface deformation (Bendtsen, 2004, Xiong and Tuononen, 2013). These deformations are respectively related to (1) Macro-texture, (2) Meso- and micro-texture and (3) micro-texture of the surface.

There are four standard measuring techniques for rolling resistance (Sandberg et al., 2011):

**(1)** Drum tests of tires in which the rolling resistance can be obtained by measuring the resistance of the tire against the rotation of a drum which is in contact with it. There are several standards for this method such as SAE J2452 (SAE 1999), SAE J1269 (SAE 2006), ISO 28580 (ISO 2009), ISO 18164 (ISO 2005). Although these tests are able to measure the rolling resistance force, they are not suitable for revealing the rolling resistance mechanism. A drum with large diameter can be used to represent a flat road.

**(2)** Trailer methods. There are three different kinds of these devices, TUG, BRRC and BASt; in which the rolling resistance can be measured due to the resistance of the test wheel to rolling while it is being towed by a vehicle (Descornet, 1990, Sandberg et al., 2011, Wozniak et al. 2011, Roovers et al. 2005, Boere, 2009). These devices have been used for correlating rolling resistance to pavement surface characteristics.

**(3)** Coast-down methods in which the vehicle is accelerated to a certain speed and rolled freely afterward in neutral gear. Since in this method all the significant contributions of driving resistance are involved, no direct measurements are obtained for rolling resistance.

**(4)** Fuel consumption methods. Which are the most general methods for assessment of rolling resistance since they include all possible contributions that influence the energy loss and therefore it is difficult to pinpoint the rolling resistance losses (Anderson et al., 2014).

Among these methods trailer method is more common than the other ones (Anderson et al., 2014).

Moreover, new techniques have been introduced which are capable of measuring different components of rolling resistance. For example, by using tire sensors the contact pressure of the tire can be measured even in high-speed rolling tires. Since hysteresis depends on time history of stress and strain, rolling resistance can be obtained by these methods. Optical tire sensors can also be used for tread deformation measurements by two laser triangulation sensors and the wheel rotation angle measurement (Xiong and Tuononen, 2013).

The combination of operational factors (e.g. deflection, pressure, load and speed) and tire material characterize the contribution of each hysteresis component and their interaction with each other. Over the years correlations have been found between tire deformations and hysteresis by various methods: (1) comparing rolling and non-rolling tires (Williams and Dudek, 1983) , (2)using viscoelastic models with finite element method (Luchini et al., 1994, Fraggstedt, 2008, Boere, 2009 and Lopez 2010), static finite-element model (Shida et al., 1999) or a combined finite element model by considering thermal losses in addition to rolling resistance (McAllen et al., 1996, Park et al., 1997, Song et al., 1998, Ebbott et al., 1999, Rao et al., 2006). (3)The empirical Magic Formula (Pacejka 2012) and its extended version introduced by Besselink et al. (2010), which gives the ability to consider pressure changes without having a set of parameters defined for them, improved the rolling resistance identification. (4) Probabilistic methods also have been used for road-tire modeling (Vantsevich and Stuart, 2008) (5) Numerical procedures (Lin et al., 2004). These modeling are usually performed in ABAQUS and ANSYS software and various material properties, rolling speed, tread profile, inflation pressure, normal load and ambient temperature are considered.

The rolling resistance components have been modeled by different method. Tire deflection can be modeled as Rayleigh damping by using Green's function (Larsson, 2000, Wullens and Kropp 2004, Lopez 2010), the tread slip as frequency independent (viscous) damping (Lopez 2010, Boere 2009), and tread deformation as high frequency micro-loading.

Although in tire industry many efforts has been done for developing new compounds and improving tire structure and tread designs, the mechanism of rolling resistance is far from being understood. One of the most important factors influencing rolling resistance mechanism is surface texture. Many experimental studies have been done for finding the influence of surface texture on rolling resistance on different types of concrete and asphalt pavements (Bester, 1984, Descornet, 1990, Delanne, 1994, Jamieson and Cenek, 1999, Hammarström et al., 2009). It is worth mentioning that although it is well-known that macro-texture increases rolling resistance of the tire, there is no universal agreement about the influence of the type of the pavement on rolling resistance. One reason for this shortcoming is the lack of proper measurement tool.

**Coupling friction and rolling resistance models**

Friction between tire and pavement has two major components of adhesion and hysteresis (Hall et al., 2009). On the other hand, rolling resistance occurs due to the hysteresis because of tire deformations (Bendtsen 2004). It is obvious that these two phenomena overlap each other on their hysteresis component. It should be taken into account that since friction is related to smaller scales of surface texture (nano-, micro, meso- and macro-texture), while higher texture scales also have influence on rolling resistance, the components of hysteresis which are involved in these phenomena are different. Therefore, the friction hysteresis components are tread slip friction (micro- and meso-texture) and tread deformation friction (nano- and micro-texture); While in rolling resistance bending hysteresis (Macro-, mega- roughness) is involved additionally (Bendtsen 2004).

Although this knowledge is available, most of the researches have not considered this overlap and studied these two phenomena separately. In 2000, Sandberg et al. investigated the relationship between friction, noise and rolling resistance experimentally. The correlations have been found between friction-noise and rolling resistance-noise but the friction-rolling resistance relationship was not obtained directly. No other study has been found regarding this relationship.

## 2.5 CHARACTERIZATION OF TIRE PROPERTIES IN DIFFERENT SPEED RANGES

Velocity has different effects on tire-pavement interaction due to the viscoelastic properties of the tire. It can change the tire surface deformation and tread slip, or it can have influence on the contact patch length; an increase in velocity reduce the contact patch and also it affects the scale of the surface texture which is in contact with the tire. In higher velocities tire is mostly in touch with macro-texture while in lower velocity micro-texture is the dominant texture scale. Therefore viscoelasticity and stiffness of the tire plays an important role in the modeling of rolling resistance and friction.

Currently different studies have been done for exploring these effects separately, either with experiments or modeling. Different experimental studies investigated contact patch forces and features by using accelerometers (Braghin et al. 2006, Matilainen et al. 2012 and 2014). In these studies they considered the effect of different factors such as rolling speed, inflation pressure, normal load, camber angle, slip angle, and slippage. In 2014, Xiong and Tuononen, measured the tread deformation by using optical tire sensor. They also investigated the effect of velocity on contact patch. But these studies were unable to find a quantitative relationship between the tread deformation and rolling resistance, because tread deformation is not uniform along the width of the contact patch and their equipment were insufficient for capturing the deformation in both directions.

# CHAPTER 3 - Experimental data

For investigating the tire-pavement interaction, experimental data of both surface and vehicle performance are required. For this purpose, several pavement samples were cored from Michigan state University campus and their surfaces were measured while the friction test were performed on them.

## 3.1 SURFACE TEXTURE MEASUREMENT

In this project the main focus has been on the effect of surface micro-texture on friction. Hence, the surface texture measurements should be performed by a device with high resolution. For obtaining such data, the measurements should be taken place in the laboratory. Therefore, samples should be cored from the field, transferred to the laboratory, cut, and then measured. Here, this process is divided into sample preparation and surface measurements:

### 3.1.1. Sample preparation

This part includes identifying the location of different pavement preservation types (see Figure 20), coring the samples and sawing them to the required size. For this purpose, based on the available resources and seeking the help from IPF and Land Scape Department of MSU and MDOT, the following types of pavement treatment samples have been considered:

- Hot mixed Asphalt (HMA): cored from Michigan State University campus
- Thin overlay asphalt: cored from Michigan State University campus
- Single and double chip seal: taken By MDOT from State of Michigan
- Concrete: provided by MDOT from State of Michigan

For variability and repeatability of the measurements, 30 samples from almost 15 sections have been taken for each treatment type. Figure 21 is showing coring process performed by project team members in June 2015 on MSU campus.

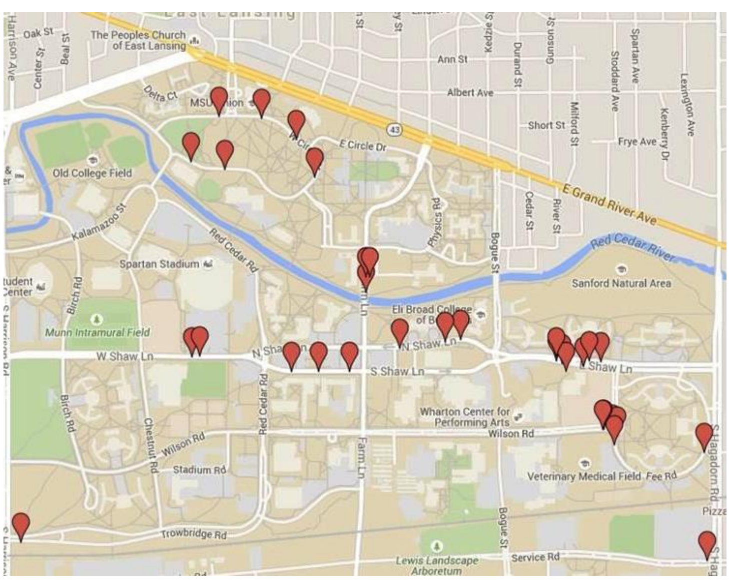


Figure 20. Map of Michigan State University campus, demonstrating the location of cored samples.

Figure 21. Core samples taken from MSU campus by research team

The diameter of the samples was 6 inches, while they were cut to almost 1 inch tall in the laboratory. Figure 22 is a demonstration of different samples in this project.

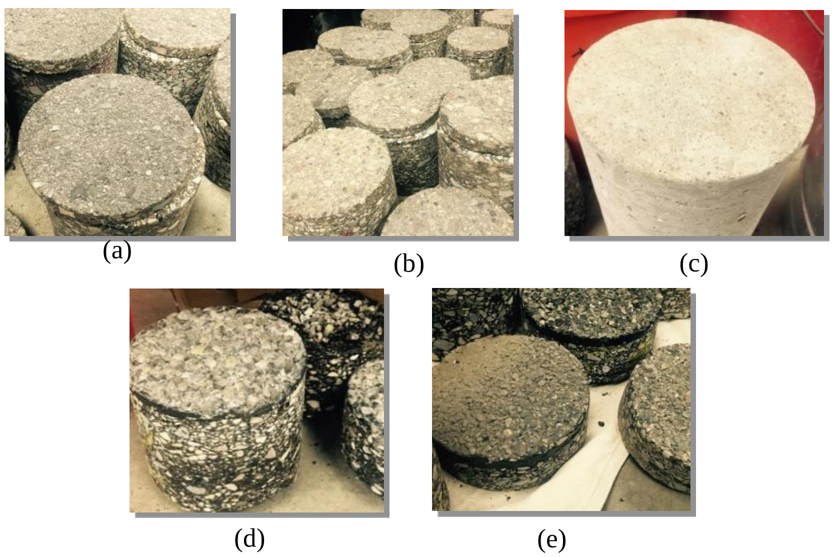


Figure 22. Samples of different pavement treatments (a) HMA (b) Thin overlay Asphalt (c) Concrete (d) Single Chip seal (e) Double Chip seal

### 3.1.2. Surface Measurement

For surface measurement of the prepared samples, Confocal Microscope was considered firstly. Although it was possible to achieve the required resolution with this device, the process was time consuming and cost much more than expected. A sample of these measurements is shown in Figure 23.

In the search for a new device, which gives sufficient resolution and performs the measurement in acceptable time, a three dimensional laser scanner was found and purchased. With this device the measurements can be obtained in seconds. The resolution of the device is 2 micron which is in the required range. An advantage of this device beside the fast process and its high resolution is that it works in 3D. Therefore, the problems that may occur using 2D lasers, e.g. loss of data in deep valleys on the pavement surface, and difficulties in overlapping the measurements for requiring a 3D picture, were not an issue anymore. The device along with the measured samples of the surfaces are illustrated in Figure 24.

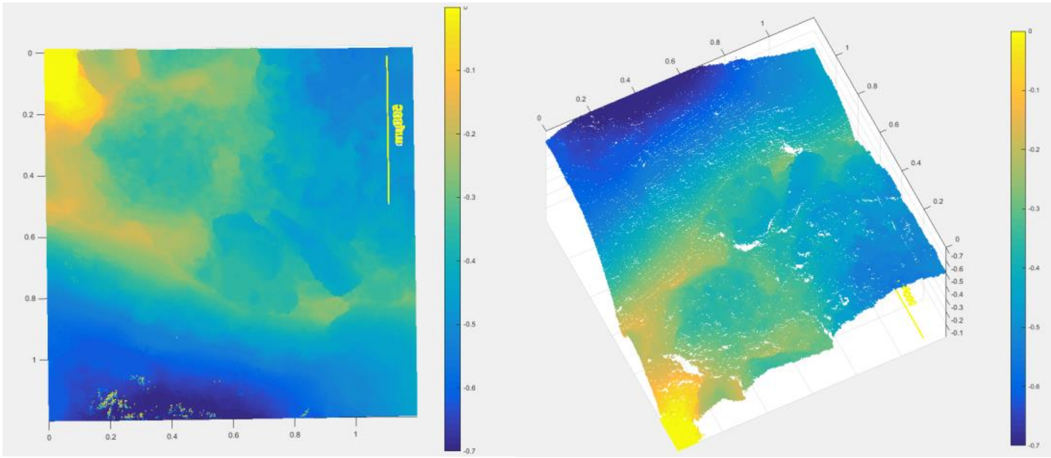

Figure 23. Surface Measurement by Confocal Microscopy

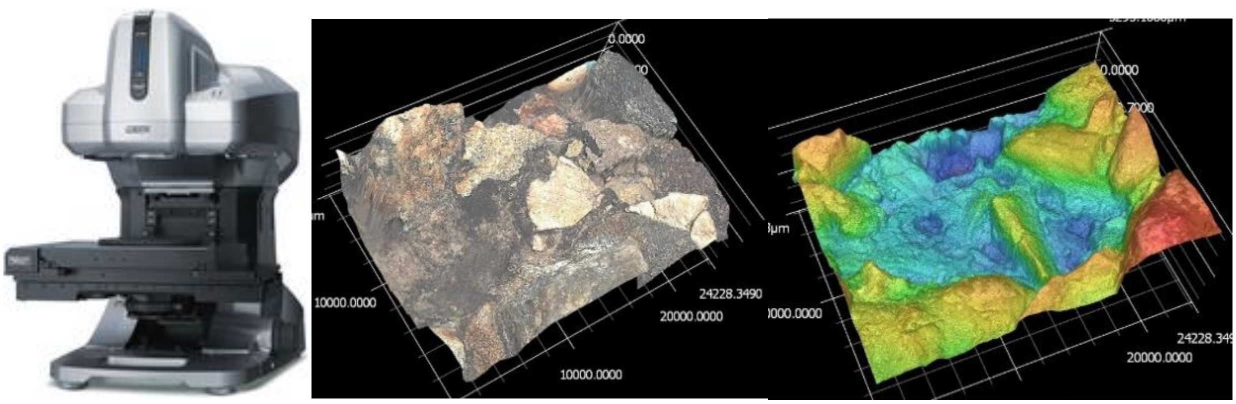


Figure 24. Surface Measurement by 3D laser scanner

For the purpose of surafce characterzation, surface measurments were performed in two different conditions. (i) Taking the measurements at four different areas in one direction, without rotating the sample, so that the slope of the measurements is the same between different samples. (ii) By rotating the sample in 10 degree steps as shown in Figure 25, to find the driving direction in different samples. The area of measurement is approximately 0.7 x 0.94 inch. The output is a matrix of 768x1024 elevation points, with unit dependent on the measurement resolution. The resolution can vary from 'x12' to 'x50'.

Figure 25. Pavement surface texture measurement (a) areas in the same direction, (b) areas in circular direction

Since after saw cutting, the samples were not completely horizontal, the measured surface should be detrended to eliminate the original tilting present in the samples. Two methods were employed for this process; eliminating the tilting through the device software or by a MATLAB code. A sample of this process is shown in Figure 26.

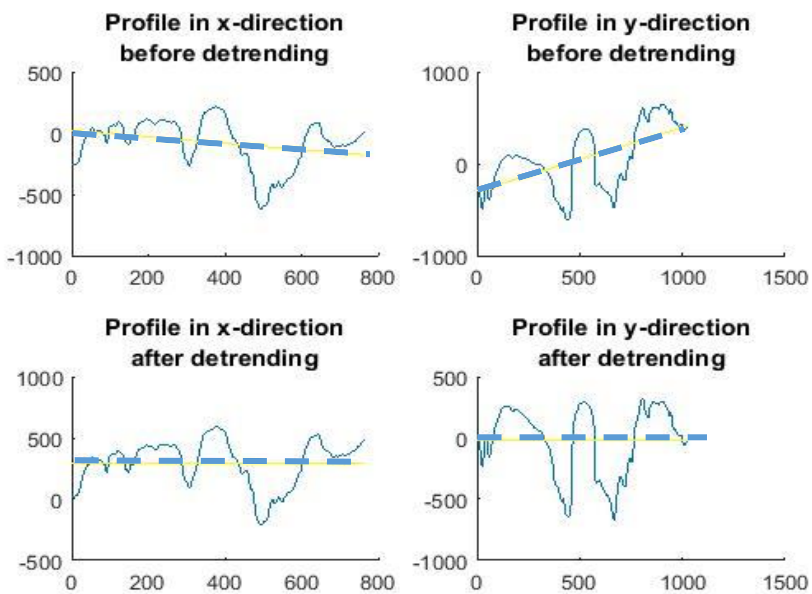


Figure 26. Comparison of inherent slope of the profile before and after performing a detrending

## 3.2 PAVEMENT SURFACE FRICTION TESTS

In this project three different methods were considered for friction measurement. One device was chosen as the primary device, which is the British Pendulum Tester in MSU,
Figure 27. Two other devices are selected for verification of the friction measurements from MDOT, which are a locked-wheel device for friction measurement in field and another BPT which were used in MDOT laboratory.


Figure 27. British Pendulum test and Locked-wheel device

The friction tests are done on the samples obtained from MSU campus (HMA and Thin overlay asphalt). These measurements are performed under three conditions of Dry, Wet and lubricated with three contaminants of water, soap and detergent. In dry condition both major friction components of adhesion and hysteresis are involved while in wet condition the hysteresis is the dominant factor. The lubricant has been used for the purpose of limiting the adhesion component and obtaining the hysteresis between the rubber and pavement surfaces. In this project the effect of two different lubricants has been considered (soap and detergent).

# CHAPTER 4 - ANALYSIS METHOD

## 4.1 SURFACE TEXTURE SIMULATION

There are various ways to characterize the surface texture. Statistical parameters have been used for this purpose for a long time. But this parameters are scale dependent and their value depends on the sample size. Having one parameter for the entire sample results in missing information in smaller scales. Therefore, these parameters should be defined for each scale separately. Another approach for surface characterization is using fractal techniques in which the surface can be defined by parameters describing the surface over various scales.

## 4.2 FRACTAL CHARACTERIZATION OF SURFACES

The main parameter in fractal analysis is fractal dimension, $D_f$. There exist many different methods to find the fractal dimension for a given fractal structure (see section Characterization and modeling:2.2.1). Although it is expected to achieve similar results by different methods for the same data set, the estimations deviate depending on the nature of the analyzed structure. Therefore, here several methods were used simultaneously to find a representative value for D.

Four power law methods of 1D power spectral density plot, 2D power image, roughness-length, and projective covering method (tessellation) were used. These methods were all developed and tested by other researchers, however, some of them have not been used for analyzing the pavement surfaces. PSD and roughness-length methods were originally developed for analyzing 1D fractal data (profiles), but PSD can be extended to 2D surfaces. Tessellation is by its nature a 2D analysis method, considered as a variation of the box-counting method in higher dimension. Accordingly, here, the data was treated either as an array of profiles or as an area. The raw surface profile data in this project is in form of 2D matrix.

It worth mentioning that depending on the type of fractal structure, single D values may not be possible to be found. This is due to the bi-fractal (usually understood as different values for small and large-scale textures (Kokkalis, Panagoulis 1997) or multi-fractal (usually understood as different values in different angular directions, (see Falconer 2003 )) natures of the surfaces. Here the surfaces are analyzed for both features, using methods established by other researchers (Xie,Wang,et.al. 1999; Thomas, Rosen, et.al. 1999; Wu 2000; Bhushan, Majumdar 1992). Another suggestion is that fractal dimension is not sufficient to fully describe a fractal structure (even if it is not bi- or multi-fractal) (Bhushan, Majumdar 1992; Russ 1994; Jahn, Truckenbrodt 2004). Therefore other parameters should be calculated e.g. frequency thresholds and coefficient G for PSD, topothesy K for structure function, and proportionality factor C for the projective covering graph.

## 4.3 FINDING FRACTAL PARAMETERS

### 4.3.1. 1D PSD

The most common power spectrum method treats the surface data matrix as an array of vectors, representing parallel profiles of a surface (Lawson, Aikens et.al. 1996, Persson, Albohr et.al. 2005, Sidick 2009, Walsh, Leistner et.al. 1999, Elson, Bennett 1995 ). By performing 1D Fourier Transform on each vector the PSDs can be obtained for each one of them. Then, the PSD plots are

averaged (with use of ensemble average) to obtain a general PSD plot. It has been instructed to take at least twenty individual PSD estimates into the computation (Elson, Bennett, 1995). The profiles should be chosen from different locations on the surface to achieve a good representative PSD of the entire surface.
The procedure involves finding the correct scaling factor for Fourier transform algorithm, appropriate treatment of the FFT output, verifying whether the studied surfaces fulfill theoretical constraints (with phase diagram) and finding D, frequency thresholds ($f_L$, $f_U$), and power scaling constant G from the PSD graphs (see Figure 28).

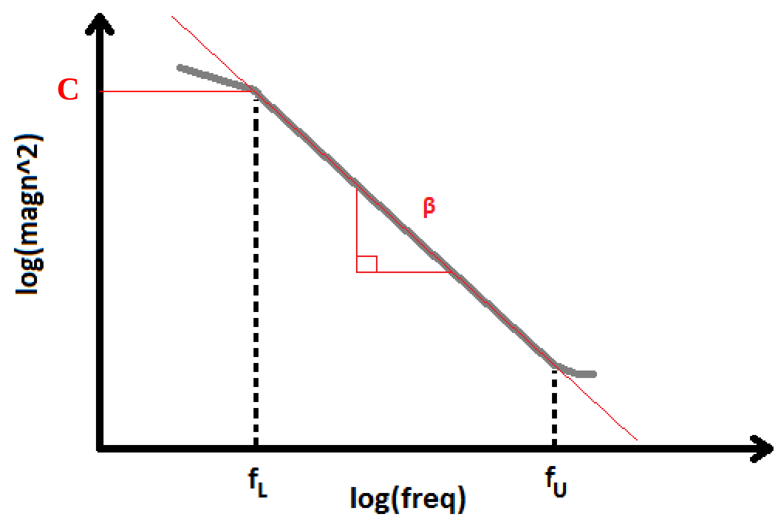


Figure 28. Structure of a well-behaved power spectral density plot. $f_L$ and $f_U$ denote the range in which the plot is linear; β is a slope of this linear tendency, found with e.g. regression plot

#### 4.3.2. 2D PSD

An intuitive approach to performing Fourier Analysis on surface area data that would not lead to any loss of potential information (as opposed to 1D PSD plot) is 2-dimensional FFT. This method is represented by fft2() and fftn() commands in Matlab. Its output is a matrix of the same size as the data matrix that contains transformed data in form of complex numbers. With any of these commands, Fourier Transform is executed first along each column, then along each row (where the rows are already arrays of complex numbers). Most of the procedure steps of this method are the same as for the 1D-PSD. Phase diagram (2D, as well) should remain random.

A so-called power image or 2D PSD results from the 2D Fourier Transform and it has a characteristical shape (Russ, 1994). The graph usually shows a characteristic 'cross' dividing the graph in four parts (from top view). The generated power image was treated as a verification step in the analysis. To extract a PSD plot from power image, the radial average of the power image should be taken. The 1D representation of log (magnitude$^2$ ) versus frequency of the data should show a tendency characteristic for power laws ($P(f) \sim 1/f^{\beta}$).

### 4.3.3. Roughness-length method

The third power law method that was implement in this project is the roughness-length Malinverno method. It is a 1D approach to analysis 2D data. The size of the window in the calculations ranges from about 5% to 20% of a profile's length (which depends on the data set). The Matlab function runs a root-mean-square residual calculation in each window following Malinverno's original instructions (Malinverno 1990). Then the result is normalized, plotted against frequency, fitted with partial least square regression. The fractal dimension of each profile is determined using the formula $D = 2-\beta$, where $\beta$ is a slope of the PLS regression fit. Note that the result is an estimate of the fractal dimension of the profiles and not the surface. It is worth noting that it is suggested that this method is suitable for self-affine fractals as well (not only self-similar, well-behaved fractals).

**Dependence of results on the choice of the smallest window size**

In this method if the data points in each window or box are too few, the obtained results for fractal dimension may not be correct anymore. For this purpose in this study the difference in results depending on the size of the smallest window has been investigated (largest window is fixed to 20% of the total number of points).

### 4.3.4. Tessellation (Projective Covering) method

Another method used for finding the fractal dimension is the tessellation method (Zhou et.al., 2003; Kwasny, 2009). Here, the 2D data matrix is treated as an array of squares (smaller matrices within data matrix). First, a grid is virtually imposed on the area spanned by the data points. The grid size, defined in number of points, is the input of this method. Consequently, the spatial resolution (in microns), the number of squares in each direction, and the number of squares in total will be obtained. Next, the area spanned by the grid of a particular size is calculated. This area can be found by summing up the areas of all squares, which were calculated separately. Since the grid nodes rarely lie in the same plane, each square has to be divided in two triangles, whose areas can be calculated using standard geometric laws, e.g. vector product (Kwasny, 2009) or multiplication of side lengths (Zhou, et.al. 2003). Both methods were used to ensure the accuracy of the results. Moreover, there are two ways to divide a square in triangles (along any of two diagonals). Although, previous studies suggested that the results should essentially be identical, here, both cases are considered. The total area of the surface is then estimated through calculating the area of the grid. Next, the size of the grid will be changed several times and all steps will be repeated.

It worth mentioning that since the calculation should be repeated for the same data, set the size of the grid cannot be arbitrary. Therefore, the total number of data points in the data set analyzed has to be divisible through any of the numbers of points on the side of each grid square. Once this has been done, log-log plot of $\delta$ (the spatial resolution mentioned above) versus Area($\delta$) is generated. The plot should be approximately a straight line with negative slope related to D, $\beta = 2 - D$. The slope is always negative, because the finer the grid, the more irregularities are included in this new grid-surface, and so the total area increases. The proportionality factor C can be found from the y-intercept on the graph of $\log(A(\delta))$ vs. $\log(\delta)$. (Kwasny 2009)

### 4.3.5. Structure function method

Structure function method is also another approach for finding the fractal dimension. To generate a structure function for a data set, the following definition is used.

$$S(\tau) = \langle |z(x) - z(x+\tau)|^2 \rangle$$

Structure function used here is one-dimensional, therefore, each profile in the data set is treated separately (structure function is found for each). After the structure function is calculated, a number of S(τ ) graphs are chosen to find a good linear fit for the entire data set. Finally, statistical analysis is performed on the results and the log-log plot of τ versus S(τ ) is obtained. From the graphs, the fractal dimension, D can be found.

The results of all the mentioned methods are compared with each other.

### 4.3.6. Other fractal parameters

***Power scaling constant G***

According to Bhushan Majumdar power spectral density has a form of

$$P(f) = \frac{G^{2(D-1)}}{f^{5-2D}}$$

where G is a scale constant with dimension of length. Accordingly,

$$\log\big(P(f)\big) = 2(D-1)\log(G) - (5-2d)\log(f)$$

$$G = 10\ e^{(y_{intercept})/(2(D-1))}$$

To find the power scaling constant for 2D PSD, the radial average should be used as $P(f)$.

***Proportionality factor C***

Using Tesselation method to find fractal dimension, there is a relationship between the number of boxes $N(\delta)$ on the side length, $\delta$, required to cover the structure and the length, $\delta$.

$$N(\delta) \sim \delta^{-D}$$

Consequently the total area can be calculated by multiplying the number of boxes by the area of each box ($\delta^2$), as

$$A(\delta) = N(\delta).\delta^2 \sim \delta^{2-D}$$

To make this equation an equality, a proportionality factor is included, $A(\delta) = C.\delta^{2-D}$. After rearranging, this gives

$$\log\big(A(\delta)\big) = (2-D)\log(\delta) + \log(C)$$

This means that the proportionality factor can be found from the y-intercept on the graph of $\log\big(A(\delta)\big)$ vs. $\log(\delta)$ (Kwasny 2009).

***Topothesy and Critical length***

After generating the structure function graph, the topothesy, K, can be found from the linear fit to the graph.

$$y_{intercept} = 2 - \frac{1}{2}K$$

The critical length $f_c$ is also described as the threshold for the linear fit.

## 4.4 INVESTIGATING MULTI-FRACTAL NATURE OF ANALYZED SURFACES

The power law methods used in the previous sections are all primarily used to find a single fractal dimension value of a fractal profile or surface. However, in the generated graphs (log-log plots) more than one tendency (more than one slope) can be recognized for all surfaces. This indicates that one fractal dimension may not be enough for defining a pavement surface properly and therefore, the fractal nature of the surfaces is scale-dependent, i.e. the surface has different fractal dimensions on different scales (so on different resolutions and measurement frequencies). Moreover, in 2D methods (2D PSD and Projective Covering) it was observed that the fractal dimension is not constant in different directions of the surfaces. This proposition seems reasonable for pavements and might be easily explained, as the tires in contact with the surface, in usually consistent driving direction, polish off the rough texture and make it smoother. Subsequently fractal dimension value of the surface would decrease in the driving direction, and remain constant (or change less drastically) in other directions. This pattern of the texture is called anisotropy and was briefly explained in the chapter 2. In this section the methods used for determining the scale-dependent fractal nature and driving direction of the surfaces are presented.

### 4.4.1. Scale-dependent fractal nature of pavements

Scale-dependency seems to contradict one of the main characteristics of fractals, scale-independency of fractal pattern. Therefore, it should be treated with caution and understood as different fractal pattern on different texture-scales. Thus, within a particular texture range (e.g. macro-texture: from 0.5 mm to 20 mm), the scale-independency and uniform fractal nature still hold. This behavior can also be verified by power law methods to check the accuracy of the tendencies found in log-log graphs. Here, the structure function of the surfaces is calculated and fractal dimension values and other fractal parameters (topothesy, K, and critical length, fc) are found (see Figure 29 ).

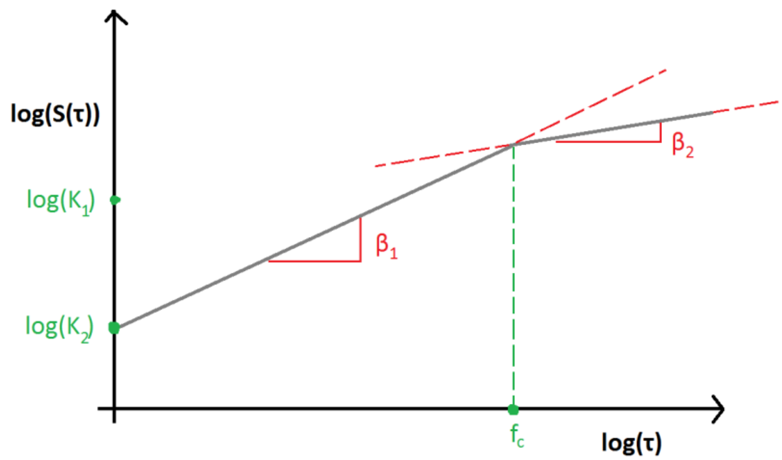


Figure 29. Bi-fractality by Structure function method

Although the size of the data sets used here are the same, there is no restriction applied by the method for the total required number of points. This is one of the reason that this method has been chosen among the available ones.

#### 4.4.2. Anisotropy: driving direction on fractal pavements

For determining the anisotropicity of the pavement surfaces and dependency of the fractal dimension on the direction of the measurement, measurements are performed by rotating the sample by ten degrees increments. Then the fractal dimension in each direction is calculated using the aforementioned methods.

### 4.5 OBTAINING 3D SURFACE

In this part of the project different approaches for generating a fractal surface are investigated. The four algorithms used here are categorized in two groups of Fractal Interpolation methods (BFIS model) and Simulation methods (iFFT, Blackmore and BFIS enhanced Blackmore models). Moreover, the influence of the input parameters on the output of each algorithm is studied.

#### 4.5.1. Fractal Interpolation methods

Here, only one Fractal Interpolation technique, Bivariate (Recurrent) Fractal Interpolation Surfaces algorithm, is considered.

***Bivariate FIS***

Bivariate FIs is an interpolation method for generating self-affine surfaces. For generating a surface using this method, limited number of points is extracted from the raw data points. Using the algorithm after performing some iteration the surface is created. The more the number of iterations, the more the resolution of the results will be. However, there may be a limitation on the number of points and iteration due to the computational cost of the process.

### 4.5.2. Simulation methods

In this section some of the available algorithms for simulating fractal surfaces are discussed. Contrary to the previous surface generation algorithms, simulation methods do not require data points as an input, only values of fractal parameters. Using the values of fractal parameters found from a given surface, the generated surface should contain the same characteristics as the original surface. The simulation methods presented in this section are: iFFT-based simulation (following (Wu 2000; Wu 2002; Wu 2004)), Holder type condition anistropic surface model (following (Blackmore, Zhou 1998)) and Holder type condition anisotropic surface model enhanced with BFIS interpolation method.

***Inverse FFT surface simulation***

This method of surface simulation is based on the Inverse FFT algorithm. Data points are computed as a sum of constituents resulting from the power spectral density of the surface. Therefore, PSD is the main input in this simulation. It is computed based on frequency, fractal dimension, and power scaling constant.

Here, the scale dependency of the surface is also taken into account and the input parameters are defined in order to keep the continuity in the PSD plot. The values of all input parameters are chosen based on the results of fractal analysis of asphalt pavement surfaces.

The output of this simulation is a 2D array of complex numbers. To plot the surface, the absolute value of each point is taken. Additionally, a contour graph of the surface is obtained, which gives an easier overview on the pattern of the surface (and iso- or anisotropic nature of it).

***Blackmore anisotropic surface simulation***

This simulation method is an anisotropic fractal model by Blackmore and Zhou (Blackmore, Zhou, 1998).

It is a technique derived from Holder type condition that the surface has to satisfy. Several input parameters are required for the mathematical process of this procedure, which the non-geometrical parameters are taken from Blackmore and Zhou study.

The output of the algorithm is discrete elevation data that can be plotted on an x,y grid. Here, the bi-fractality or multi-fractality of the surface are not included, since it the algorithm leads to an anisotropic surface model and the attempt for changing it was not successful.

### 4.5.3. Combination of simulation and interpolation

The algorithm written for this method first computes elevation data of an anisotropic surface with Blackmore and Zhou's fractal model, and then interpolates between computed points with BFIS algorithm. Formulas for both processes and their required parameters were given in the previous sections. The output of the algorithm is discrete elevation data that can be plotted on an (x; y) grid.

This method builds in an additional self-affine, fractal pattern into an anisotropic fractal model of a surface. Here, it is assumed that the surface remains anisotropic and the fractal nature becomes scale-dependent (bi-fractal).

### *Validation of the surface structure*

In this part of the project, the generated surfaces in the previous sections are analyzed. For this purpose, one of the samples from the measurements is chosen and the required parameters are derived from the raw data. The surfaces are then generated by using the mentioned methods. Due to the number of variables in the algorithms, e.g. arbitrary spacing between data points, arbitrary amplitude, and random coefficients, etc, for validation the surfaces are compared to each other by comparing their fractal and statistical parameters.

### *Fractal analysis of the generated surfaces*

In all procedures of fractal techniques it is necessary to define the spacing between data points of the analyzed data set. Analyzing experimental data, the spacing is equal to the measurement resolution. Analyzing the generated surfaces based on frequency (all methods except the iFFT model), arbitrary value for the spacing can be chosen. Here, the value corresponding to the measurements is chosen for spacing, so that the generated surface data can be compared to experimental data.

Then, the fractal analysis on the generated surfaces is performed using five methods described in the previous part: 1D PSD, 2D PSD, RMS-roughness, Projective Covering, and Structure Function. The generated surface data is treated in the same manner as the experimental data. In this way, it is possible to verify the correctness of the algorithms, comparing the input and output fractal dimension. Here, the relative error of fractal dimension estimation is chosen as the verification criteria.

### *Statistical analysis of the generated surfaces*

Statistical description of surfaces has been used for long for surface characterization. Therefore, as a part of the verification process, the statistical parameters obtained from each generated surface is compared to the original data from measurement. The statistical parameters calculated here are: $S_a$ (arithmetical mean deviation), $S_q$ (RMS height of the surface), $SR_{3z}$ (base roughness areal depth), $SR_{max}$ (maximal peak-to-valley height of the surface, $SR_{pm}$ (mean peak areal height), $SR_{tm}$ (mean peak-to-valley areal roughness), $S_{sk}$ (surface skewness), and $S_{ku}$ (surface kurtosis).

## 4.6 INFLUENCE OF PAVEMENT PROPERTIES ON HYSTERESIS COMPONENT IN MICRO-SCALE

### 4.6.1. FE model description

In modeling the influence of pavement properties on friction the focus of this project is on the effect of surface texture. For thoroughly considering friction, adhesion and hysteresis components should be considered in the contact. Having these two component two types of contact are involved: non-adhesive contact and adhesive contacts; which in the first one the loss of energy is contributed to the rubber deformation and hysteresis, while in the second one the loss of energy due to the effect of adhesion should also be considered. In this project, only the non- adhesive contact between rubber and a rough surface is investigated (see Figure 30).

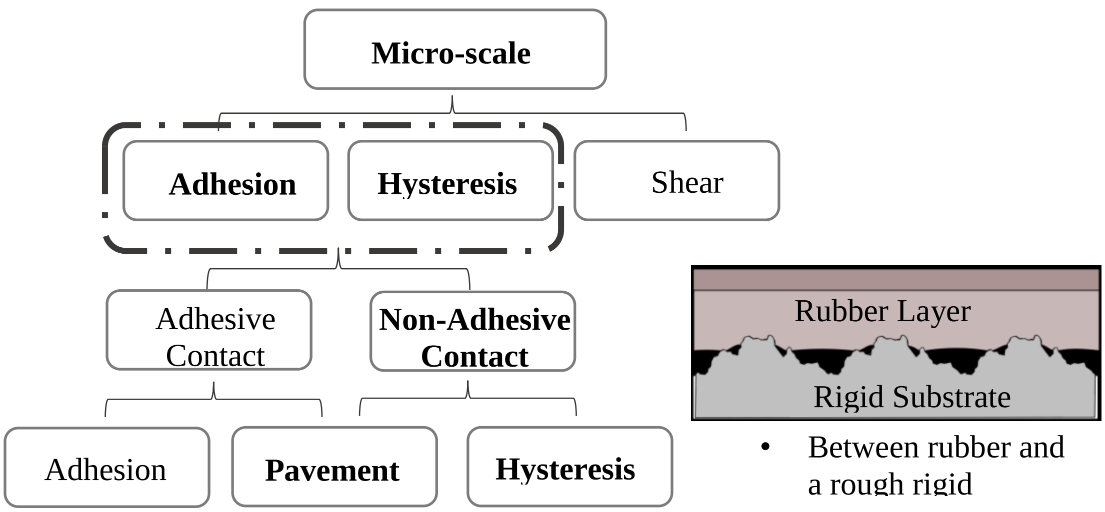


Figure 30. Diagram of the main approach of the project

Here, the finite element model for sliding rubber block on pavement surface has been developed with ABAQUS/Explicit and ABAQUS/Implicit software.

***Geometry of the model***

The generated model is two-dimensional. There are two main parts in this model; the pavement surface and the rubber block. In this model pavement surfaces have been considered as single or combination of sinusoidal waves, with different phase angle between the waves (0-2π), as shown in Figure 31:

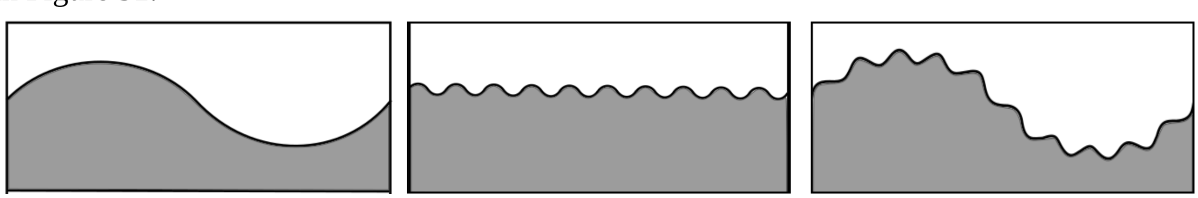

Figure 31.A sample of wavelength combination for pavement surface simulation in FE model

The ratio of wavelength to amplitude (λ/h) of 10 is chosen based on the surface measurement results. At this stage the largest wavelength is chosen to be 4mm.

For generating the surfaces in ABAQUS, the coordinates of the surface are obtained from a Matlab code, the surface is constructed in Auto-cad, and then imported into the ABAQUS model.

For decreasing the computational cost, the smallest required size for the rubber block, which satisfies the boundary conditions, should be found. For the width of the block there is a limitation; the rubber block width should be more than the maximum wavelength. Because, for amounts less than the maximum wavelength, the boundary conditions on the two ends of the block will not be the same (loss of contact at one end). Therefore, here, 4mm is chosen as the width size of the rubber block. The height of the rubber should be big enough to ensure that the load application zone does not affect the contact zone. Therefore, for finding the height of the rubber element, sensitivity analysis is performed to obtain the minimum height in which for values less than that the response of the block to the applied load changes. As a result, the final height of 12 mm is chosen, giving the rubber block the dimension of 4 mm*12 mm.

***Boundary conditions***

For completely defining the problem boundary conditions should be applied. The following boundary conditions have been applied to the model:

- As a rigid element, pavement surface requires the boundary condition defined at only one point. Therefore, a reference point should be defined for the part. Since in the model, the rubber block is sliding on the pavement surface, the pavement surface (reference point) is considered fixed in all directions.
- In Sliding, the top surface of rubber is constrained to move perfectly horizontally
- For simulating a large system by modeling a finite representative element, periodic boundary conditions (PBCs) are required. In this way the rubber block represents the whole tire tread near the surface. For this reason PBCs have been applied to the nodes on the two walls of the rubber block, as follows:

$$u_{left} = -\, u_{right}$$

where, u is the displacement of the node (see Figure 32).

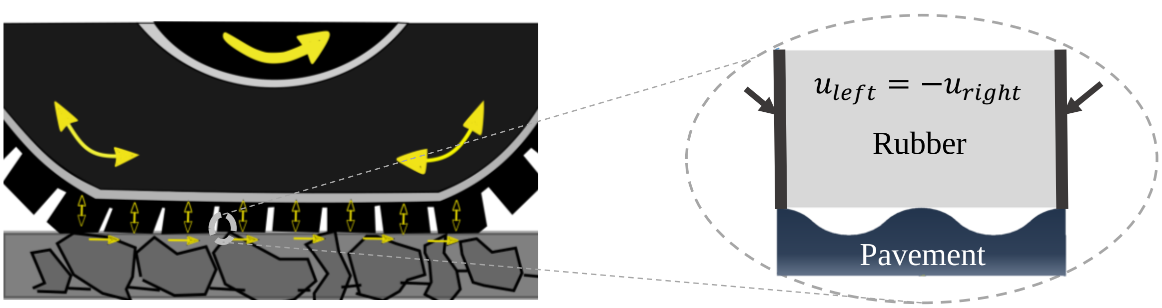


Figure 32. Periodic Boundary condition

This PBC should be applied in both horizontal and vertical direction. For implementing PBCs equation constrains have been used. Using this periodic boundary condition on the sides, all of the points on the side walls are forced to have the same strain and stress distribution as depicted in Figure 33.

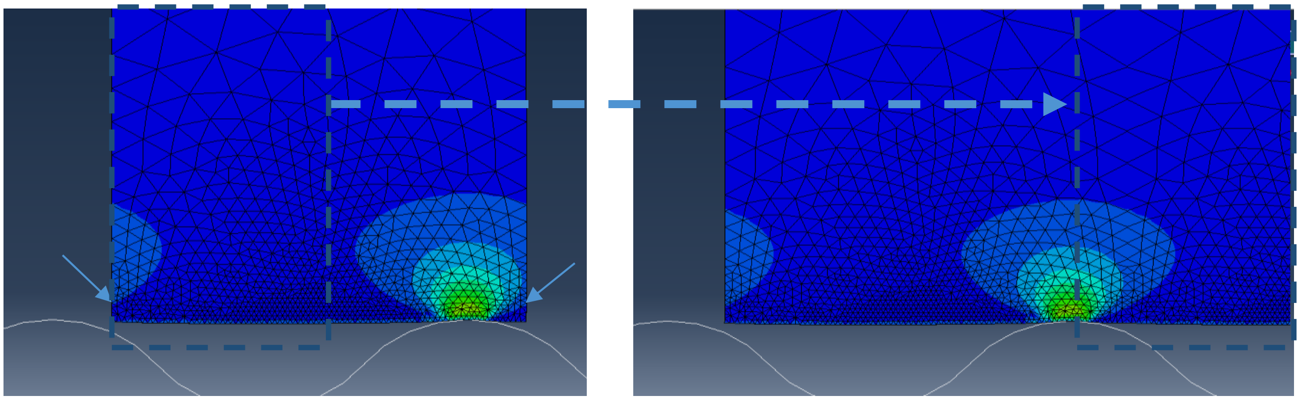

Figure 33. Periodic Boundary condition effect on stress distribution

### ***Interaction properties***

The contact is considered as a friction-less and hard contact since the effects of hysteresis and rubber deformation are required only. The interaction is defined as a surface to surface interaction, since the aim is to prevent any over-closure between the two surfaces. The rigid body is defined as the master surface while the rubber surface is defines as the slave curve.

### ***Applied loads***

There are three different steps defined in the simulation of the model,

Step 1: applying pressure (0.2 MPa equal to the pressure of passenger tires),
Step 2: accelerating the rubber block to a predefined velocity, and
Step 3: sliding the rubber block with a constant velocity.

A schematic view of the geometry of the problem and the applied loads are illustrated in Figure 34.

### ***Material properties***

In this project, the rubber material is considered as a visco-elastic silica-filled rubber material. The material properties can be imported into ABAQUS by two different methods.
(i) by importing a **Prony series** into the material properties of the model. Given the Prony series for elastic modulus, as

$$E(t) = E_{\infty} + \sum_{1}^{n} m_i E_0 \exp(-\frac{t}{\tau_i})$$

in which, $E_{\infty}$ is the long term response, $\tau_i$ is the relaxation time, and $m_i$ are the Prony factors. The Prony series for shear and bulk modulus can be obtained from the elastic Prony series. For incompressible material the bulk modulus can be considered zero and the shear modulus coefficient $g_i$ should be obtained to be inconsistent with the following formula

$$G(t) = G_{\infty} + \sum_{1}^{n} g_i G_0 \exp(-\frac{t}{\tau_i})$$

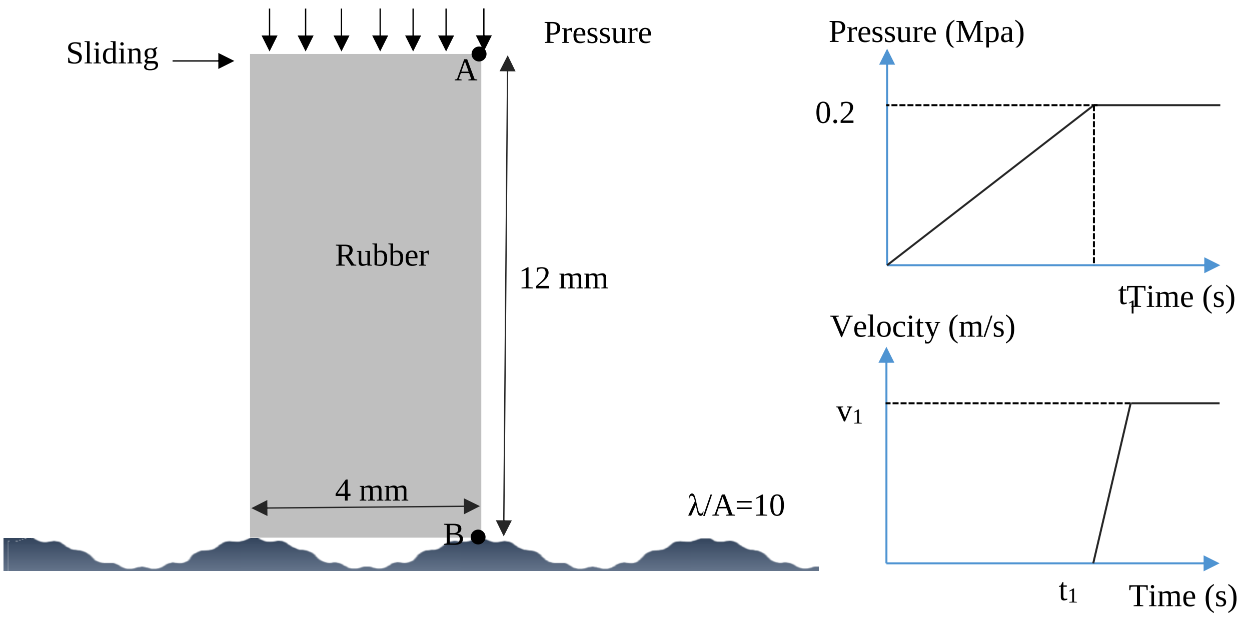


Figure 34. FE model geometry and applied loads

Poisson ratio is considered to be 0.49, and the density is defined to be near zero, to eliminate the dynamic effect.
The ratios of $m_i$ and $\tau_i$ are defined below:

Table 4.Prony series coefficient for rubber material

| $\tau_i$ | $m_i$ |
|---|---|
| 0.0002 | 0.25578 |
| 2.00E-03 | 0.19044 |
| 2.00E-02 | 0.13667 |
| 2.00E-01 | 0.1144 |
| 2 | 0.06416 |
| 20 | 0.03468 |
| 200 | 0.02542 |
| 2000 | 0.01769 |
| 2.00E+04 | 0.01199 |
| 2.00E+05 | 0.00871 |
| 2.00E+06 | 0.00499 |
| 2.00E+07 | 0.00569 |
| 2.00E+08 | -0.00109 |
| 2.00E+09 | 0.00869 |

Consequently, $E_{inf}$=0.12178.
(ii) By importing the constitutive model as a **UMAT subroutine** into the model. In this model, the material is considered hyperelastic-viscoelastic. The material properties are defined by calibration of the model with test results found in the literature.

There are various user subroutines for users provided by ABAQUS/Standard to adapt the software to their particular analysis requirements. These subroutines provide extremely powerful and flexible tools for analysis. They are typically written in Fortran 77 language and C++, and they should be included in the model while execution. However, it may be possible to write the subroutine in other languages as long as we could call them in Fortran. Fortran is designed for scientific programing and it has both object oriented programming and parallel programming built in, so it is suited for large scientific codes. Also it is very fast in comparison to other programs.

### *Types of subroutine*

There are two methods for solving a dynamic equilibrium equation at a time step.

- **Explicit** methods use much smaller time steps in comparison to explicit ones, because they are conditionally stable. This means that the time step for the solution should be less than a certain critical time step. This time step depends on the smallest element size and the material properties. However, they do not involve any matrix solution. Therefore, their computational time per load step is relatively low and they require less storage than implicit algorithms.
- **Implicit** methods can use much larger time steps and they are unconditionally stable. However, they involve the assembly and solution of a system of equations. Therefore, although the time steps are larger, the computational time per load step is relatively high and the storage requirements increase with the size of the mesh. Implicit methods are more difficult to implement.

Correspondingly, there are two types of subroutine for these different methods:

- **VUMAT** for explicit methods
- **UMAT** for implicit methods

### *Subroutine implementation in ABAQUS*

Before discussing writing a subroutine, it is important to know how we can implement it into ABAQUS [7]. For running a user subroutine in an ABAQUS analysis, we require a functional combination of Intel Fortran and Microsoft Visual Studio, beside ABAQUS. There are two methods for running the subroutine, (1) through the software interface (2) with modifying the input file.

(1) To include the subroutine through the software interface, the name of the file with the user parameter should be specified on the ABAQUS execution command as:

    ABAQUS job=**my_analysis** user=**Yeoh-visco**

    The file can be either a source code (my_subroutine.f) or an object file (my_analysis.o). The file extension can be included in the command (user=my_analysis.f); otherwise, ABAQUS will determine automatically which type of file is specified.

(2) For implementation through modification of input file, initially the model should be defined in the ABAQUS interface with a random material definition. After running the model for insuring a successful analysis, the input file can be obtained. Two changes should be implemented to the input file. 1) in Assembly :changing the material name to subroutine name 2) in Material, changing the material name to subroutine name, modifying the density and defining the number of variables required at each point by setting DEPVAR value. A sample of this modification is shown below.

**"ASSEMBLY"**
Material=Yeoh
------------------------------------------
**"Material"**

```
** MATERIALS
**
*Material , name= Yeoh
*Density
1. 2 e−9,
*User Material , constant s=1
1. ,
*DEPVAR
6**
```

Note than subroutine should be in the same directory as the input file.

A complete comprehension of the structure of ABAQUS is not required for developing a user subroutine. Nonetheless, it helps to know the overall structure. In the Figure 35, a flowchart is presented for the flow of the data and actions of an analysis in ABAQUS.

***Steps required for writing a subroutine for a constitutive law:***

For implementing a subroutine in ABAQUS, the first step is to define the inputs and outputs of each increment. These outputs should be stored to be used for the next increments. An example of inputs and outputs of constitutive model are shown in **Error! Reference source not found.**.

Table 5. Inputs and outputs of UMAT Subroutines

| **Inputs** | **Outputs** |
|---|---|
| Total, elastic and inelastic deformation gradient $\boldsymbol{F_t}$,$\boldsymbol{F^e}_t$, $\boldsymbol{F^i}_t$ | Elastic and Inelastic deformation gradient $\boldsymbol{F^e}_{t+dt}$, $\boldsymbol{F^i}_{t+dt}$ |
| Stress tensor at time t $\boldsymbol{T_t}$ | Stress state at the end of the increment $\boldsymbol{T_{t+dt}}$ |
| Deformation gradient at the end of the increment $\boldsymbol{F_{t+dt}}$ | Tangent matrix $\mathbb{C}$ |

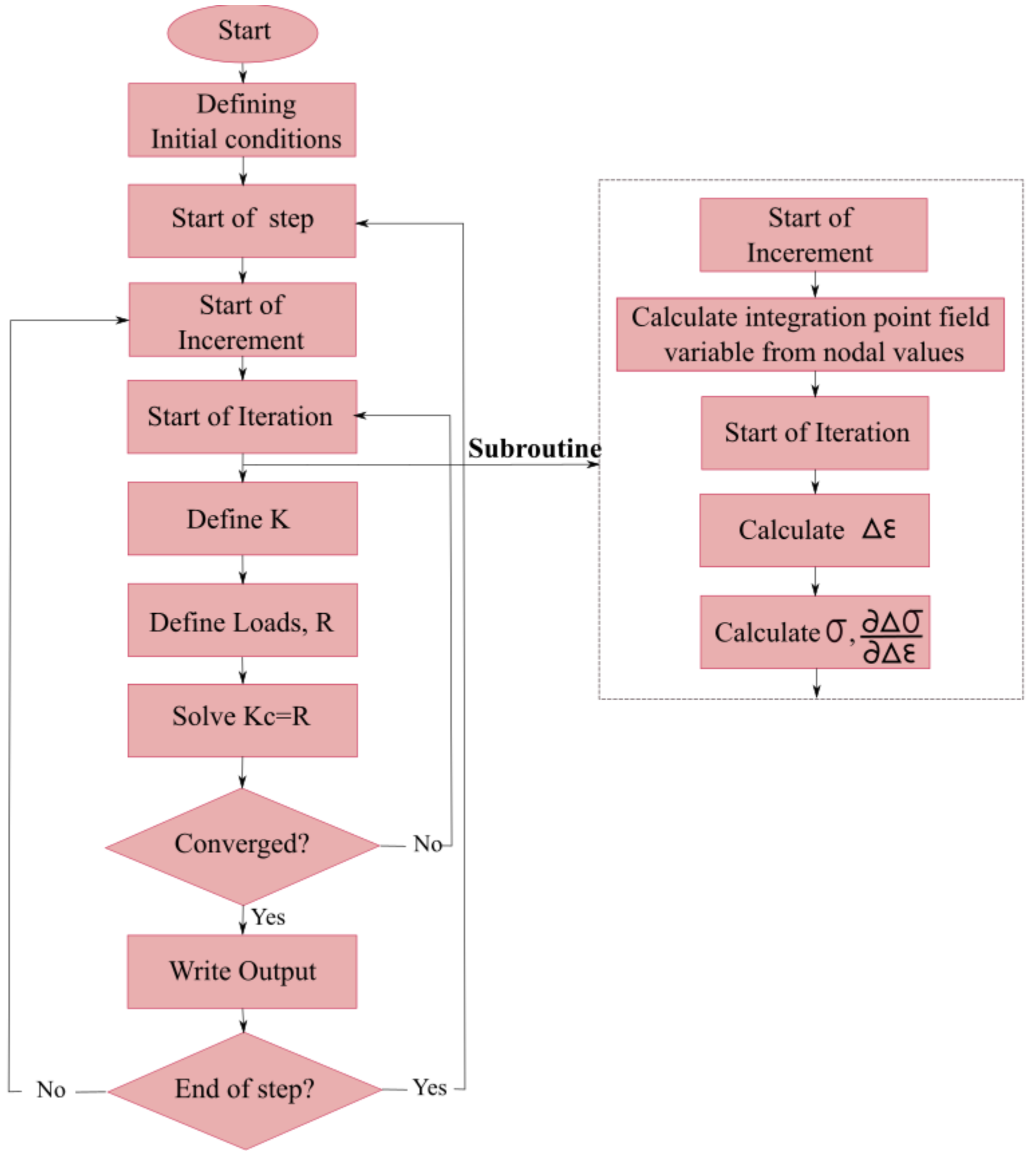


Figure 35. General flow of analysis in ABAQUS and Material Subroutine involvement

In the flowchart in Figure 36, different steps required for writing a subroutine are demonstrated. Additional information will be provided in the next parts.

### ***Material properties definition***

After defining the dimensions, variables and constants, and calling the variables from ABAQUS, the next step is defining the constitutive law. In this step, the constitutive model should be explained for explicit definition of stress-strain relationship. Here, the material property is defined as a combination of Yeoh hyperelastic model and viscoelastic model of Holzapfel (1995).

Hyperelastic materials undergo zero internal dissipation during any external mechanical work. Rubber-like hyperelastic materials are mostly considered as incompressible materials. These materials experience a volumetric locking when implemented in ABAQUS [4]. This volumetric locking is a consequence of numerical techniques in which errors in the numerical solution raises due to the high number of incompressibility constraints relative to the number of degrees of freedom. From mathematical point of view, assuming an incompressible material with Poisson ratio of 0.5, gives bulk modulus of $\kappa = \frac{E}{3-6\nu} \rightarrow \infty$, in which locking is more noticeable.

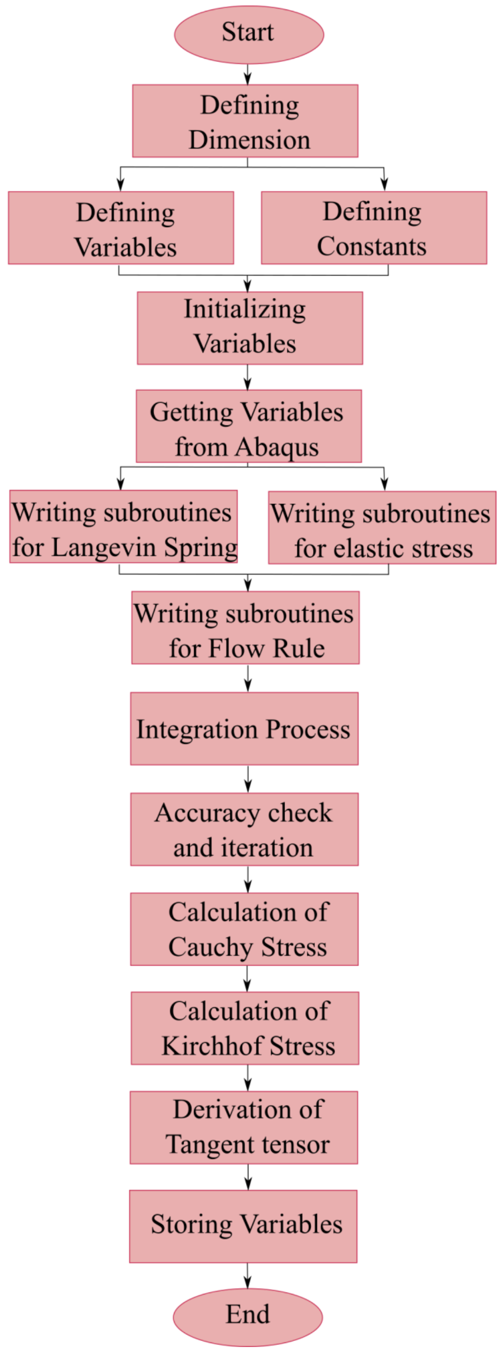


Figure 36. General Flowchart of steps required for writing a subroutine

This volumetric locking causes numerical instabilities; therefore, a mathematical treatment is required for its prevention during a simulation. For this purpose, by considering the material nearly incompressible, the constitutive formulations should be rewritten with considering a multiplicative decomposition of the deformation into purely isochoric and purely volumetric contributions. This decoupled formulation should then be implemented into the subroutine, which requires extra calculations. It should be mentioned that the tangent modulus should also be decoupled.

For developing a constitutive material for a hyperelastic material with finite strain, strain energy functions are required. Isotropic strain energy functions are scalar valued functions which are usually represented by the three invariants I1, I2 and I3 = $J^2$. In this project isotropic material models have been considered only.

Yeoh material is one of the common strain energy functions which is defined as:

$$\psi(\alpha_1, J) = \sum_{i=1}^{3} c_i \, (\alpha_1 - 3)^i + U(J)$$

where, J=det(C) is the Jacobian, C is the right Cauchy-Green strain tensor, $c_i$ are the material constants related to deviatoric response of the material, $\alpha_1 = J^{\frac{2}{3}}(C\colon I)$, where, I is the identity tensor, and $U(J)$ is the volumetric part of the strain energy. Considering the nearly incompressible property of the rubber material, the volumetric part is usually small. However, it can be defined as:

$$U(J) = \frac{1}{D_1}\left(J^2 - 1 - 2\ln(J)\right)$$

where, $D_1$ is the material constants related to volumetric response of the material and it can be considered as $D_1 = \frac{2}{K}$ , where K is the Bulk modulus of the material. Consequently the stress can be obtained from

$$S = \frac{2\partial\psi}{\partial C} \Longrightarrow S_{iso}^{\infty} = \frac{2\partial \sum_{i=1}^{3} c_i \, (\alpha_1 - 3)^i}{\partial C}, \qquad S_{vol} = \frac{2\partial U(J)}{\partial C}$$

For the viscoelasticity model, a large strain viscoelasticity continuum formulation introduced by Holzapfel (1995) has been used. Considering the material as hyperelastic-viscoelastic, the stress-strain relationship can be obtained from

$$S = S_{iso} + S_{vol}$$

$$S_{iso} = S_{iso}^{\infty} + \sum_{\alpha=1}^{m} Q^{\alpha}$$

where, $Q^{\alpha}$ are interpreted as the viscoelastic stresses. Based on the numerical simulation provided in Holzapfel (1995) study, the viscoelastic stress contribution can be evaluated by an iterative algorithm.

$$Q_{n+1}^{\alpha} = \beta_{\infty}^{\alpha} e^{\xi^{\alpha}} S_{iso\ n+1}^{\infty} + \mathcal{H}_{n}^{\alpha}$$

$$\mathcal{H}_{n}^{\alpha} = J^{-2/3} \mathbb{P}: \widetilde{\mathcal{H}}_{n}^{\alpha}, \quad \mathbb{P} = \mathbb{I} - \frac{1}{3} C^{-1} \otimes C$$

$$\widetilde{\mathcal{H}}_{n}^{\alpha} = e^{\xi^{\alpha}} (e^{\xi^{\alpha}} \tilde{Q}_{n}^{\alpha} - \beta_{\infty}^{\alpha} \tilde{S}_{iso\ n}^{\infty}), \ \ \xi^{\alpha} \coloneqq -\Delta t / 2\tau_{\alpha}$$

where, $\tilde{Q}_{n}^{\alpha}$ and $\tilde{S}_{iso\ n}^{\infty}$ are history values known from previous steps.

***Derivation of Tangent tensor***

Stress function for the constitutive model, updated with the results of integrations in the last step, is a nonlinear function of its stated variables. For implementing this stress in the finite element, the standard Newton-Raphson procedure requires the relationship between the stress and its variables to be linearized.

Here, first the linearization process is discussed. Considering a general nonlinear equation $F(x) = 0$, it is not clear to express the derivative of this function with respect to a function of x. Introducing an artificial parameter $\epsilon$, a nonlinear function f can be defined as : $f(\epsilon) = F(x_0 + \epsilon u)$.

A Taylor series expansion can be used for developing the Newton-Raphson method and the associated linearized equation as:

$$f(\epsilon) = f(0) + \left.\frac{df}{d\epsilon}\right|_{\epsilon=0} \epsilon + \frac{1}{2} \left.\frac{d^2 f}{d\epsilon^2}\right|_{\epsilon=0} \epsilon^2 + \cdots$$

$$\rightarrow F(x_0 + \epsilon u) = F(x_0) + \epsilon \left.\frac{d}{d\epsilon}\right|_{\epsilon=0} F(x_0 + \epsilon u) + \frac{\epsilon^2}{2} \left.\frac{d^2}{d\epsilon^2}\right|_{\epsilon=0} F(x_0 + \epsilon u) + \cdots$$

If we truncate this Taylor series, we find the change or increment in the nonlinear function of F(x), considering $\epsilon = 1$:

$$F(x_0 + \epsilon u) - F(x_0) \approx \left.\frac{d}{d\epsilon}\right|_{\epsilon=0} F(x_0 + \epsilon u)$$

The right hand side of the equation above is the directional derivative of F(x) at $x_0$, in direction u:

$$DF(x_0)[u] = \left.\frac{d}{d\epsilon}\right|_{\epsilon=0} F(x_0 + \epsilon u)$$

Therefore, the linearized $F(x_0 + \epsilon u)$ is expressed as:

$$\rightarrow F(x_0 + \epsilon u) \approx F(x_0) + DF(x_0)[u]$$

Applying the same linearization for Piola-Kirchoff stress and its variables $(C, \Omega)$ , considering two terms, we can have:

$$S(C+dc,\Omega+d\Omega)=S(C,\Omega)+\frac{\partial S(C,\Omega)}{\partial C}:dC+\sum_{i=1}^{k}\frac{\partial S(C,\Omega)}{\partial\lambda_m^{D_i}}d\lambda_m^{D_i}$$

$$dS=2\left[\frac{\partial S(C,\Omega)}{\partial C}+\sum_{i=1}^{k}\frac{\partial S(C,\Omega)}{\partial\lambda_m^{D_i}}\odot\frac{\partial\lambda_m^{D_i}}{\partial C}\right]:\frac{1}{2}dC$$

Therefore, we can find the tangent tensor $\mathbb{C}$ as:

$$dS=\mathbb{C}:\frac{1}{2}dC\rightarrow\ \mathbb{C}=2\frac{dS}{dC}=2[\frac{\partial S(C,\Omega)}{\partial C}+\sum_{i=1}^{k}\frac{\partial S(C,\Omega)}{\partial\lambda_m^{D_i}}\odot\frac{\partial\lambda_m^{D_i}}{\partial C}]$$

Further simplifications can be done by substituting the formulation of Piola-Kirchoff stress in the equation above.

In case of considering the incompressibility the tangent tensor is divided into isochoric and volumetric contributions.

$$\mathbb{C}=\mathbb{C}_{iso}+\mathbb{C}_{vol}$$

It worth noting that without linearization the derivation of an exact tangent tensor, in most cases is not a straight forward process; because it requires the derivation of an explicit formula for the true stress and its variation with respect to the current state in terms of a fourth-order tangent modulus tensor. Therefore, most of the time, it is calculated numerically with respect to deformation. However, obtaining a closed form of the tangent modulus is not obligatory because it is used for an iterative operator in a UMAT.

***Verification of the code***

For verification of the code, it is beneficial to develop and test it on the smallest possible model, without any complicated features like contact. For example, the code can be verified by running a uniaxial test on a simple problem that all of its displacements are prescribed to verify the integration algorithm for stresses and state variables. For verifying the tangent matrix, the same test can be run with prescribed load. Also, if the analytical solution is available or the material model exists in standard ABAQUS, another verification can be done. Afterward, the model can be applied to more complex problems.

Pavement body at this stage is considered to be rigid; therefore, it does not require any material properties.

***Meshing***

The two parts of rigid pavement surface and deformable rubber block should be meshed. The numbers of elements in both surfaces are controlled by the size of the smallest wavelength of the rigid surface. By decreasing the wavelength and going to smaller textures, both elements should become smaller. The element size of the rubber should be much smaller than the smallest wavelength, otherwise after deformation the two surfaces penetrate each other. However, by reducing the mesh size, the time increment decreases and therefore the time of process increases. The model that needs seconds to run with a smooth rigid surface needs a long time to process with small wavelengths.

The rigid surface is meshed with a single size of mesh for all parts. However, the mesh in rubber block is constantly changing from the contact surface to the top layer. For this purpose the walls of the rubber block are divided into partitions and different numbers of points are allocated to each partition, so that the elements size increases smoothly as they reach to the top layer (see Figure 37).

### *Element type*

The elements are defined as plain-strain elements since the rubber block is assumed to be thick in the perpendicular direction. Rectangular linear elements have been chosen with free mapping, so that from bottom to the top of the rubber block the size of the elements can change smoothly, in contrary to the structured mapping which forces constant width to the elements (see Figure 37**Error! Reference source not found.**). Triangular elements cannot be used due to volumetric locking problem of this type of element, when the material is incompressible. To prevent volumetric locking, hybrid rectangular element is chosen.

There is no need to define element type for the rigid body.

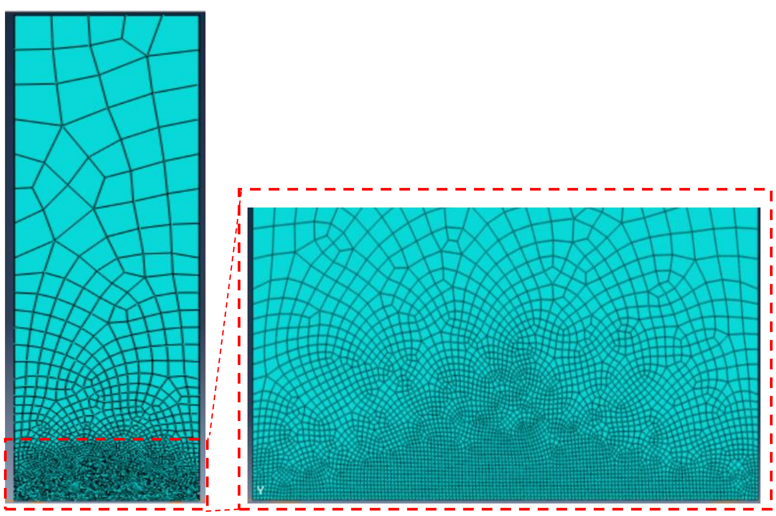

Figure 37. Rubber block meshing

### *Quasi-static analysis*

Using the first method for material property characterization (Prony series), the material is defined as a time-dependent material. Therefore, a solver should be chosen which is capable of modeling this type of material. Considering that in this study, the focus is not the inertia effect of the contact. The main variable applied load here is in the contact interface and from pavement surface to rubber. This load is a smooth sinusoidal load and cannot be considered as an impact. It happens slowly enough for the system to remain in equilibrium. Therefore, it can be considered as quasi-static. For modeling quasi-static problems there are three different ways:

- Using Explicit solvers with mass scaling to eliminate the inertia effect.
- Using Implicit solver with quasi-static condition
- Using Visco solver which is specifically built for rate dependent material in quasi-static condition

Here, the Explicit solver is chosen, since it can be more general than the other two and it can gives us the ability to use adaptive meshing if required. The explicit dynamics procedure is a true dynamic procedure. It is originally developed to model high-speed impact events and the state of dynamic equilibrium where inertia can play a dominant role in the solution. Thus, its application for modeling a quasi-static event requires special consideration. Since it is computationally impractical to model the process in its natural time period, artificially increasing the speed of the process in the simulation is necessary to obtain an economical solution. However, since a viscoelastic material is rate dependent this solution cannot be implemented in this project. So, Mass scaling has been used, which allows the modeling of the process in its natural time scale when considering rate-sensitive materials. It artificially increases the material density by a factor of $f^2$, increasing the stable time increment by a factor of f. So that, fewer increments are required to complete the process. It worth mentioning that, if the speed increases, the state of static equilibrium evolves into the state of dynamic equilibrium and the inertia force becomes more dominant. Thus, it is important to model the process in the shortest time period (higher mass scaling) in which the inertia force is still insignificant.

### *Static analysis*

Using UMAT subroutine for material definition, static analysis is able to perfume the required analysis for the model. Using static analysis, material properties, steps, element type and boundary conditions should be defined again.

### *Validation of the model*

There are a few ways to control the validity of a model. The main important factor for evaluating whether the results of the Explicit model reflect a quasi-static solution or not is examination of the energy content. For this matter, the following factors should be considered

- The energy balance should hold at all time

$$E_I + E_V + E_{FD} + E_{KE} + E_{IHE} - E_W - E_{PW} - E_{CW} - E_{MW} - E_{HF} = E_{total} = constant$$

where, $E_I$ is the internal energy,
$E_V$ the viscous energy dissipation,
$E_{FD}$ the frictional energy dissipation,
$E_{KE}$ the kinetic energy,
$E_{IHE}$ the heat energy,
$E_W$ the work done by external loads
$E_{PW}, E_{CW},$ and $E_{MW}$ are respectively the works done by contact penalties, constraint penalties and propelling added mass,
$E_{HF}$ the external heat energy through external fluxes, and

$E_{total}$ is the total energy equal to the sum of the aforementioned energys.

- The total energy should be constant, in a quasi-static case near zero.
- The kinetic energy of the deforming material should not exceed a small fraction of its internal energy throughout the majority of a quasi-static analysis. A small fraction typically means 1–5%.

Another method to evaluate the model is to check the response of the simulation, e.g. the maximum penetration of any points of the rubber block in the interface should become equal after some cycles and the responses of the simulations should become periodic.

It worth mentioning that there are some built in evaluations in ABAQUS software, e.g. for evaluating the material properties.

### 4.6.2. Running FE model

As it was mentioned previously, in this project the main goal is investigating the effect of different surface textures on hysteresis component of the friction. In order to do so, apart from measuring the hysteresis, some of the established assumptions of contact mechanics are investigated here.

One of the most important assumptions that most of the contact mechanics models are based on is that the friction is the sum of hysteresis over different length scales. This means that friction can be calculated by decomposition of the surfaces to different length scales. While assessing this assumption, the effect of phase angle between two different waves is also investigated. This effect looks promising for future studies.

Moreover, it has been known that the applied pressure (P) and area of contact (A) have a linear relationship unless the pressure is so large that the contact area is close to nominal contact area ($A_0$). Here, for the same surface, different loads are applied and the contact area in each case is calculated. To be sure that the contact area obtained from the software is correct, a Matlab script was written and the results were compared with each other for a simple single wave case. Since the results match one another completely, the output of the software is used in future parts. The other assumptions are as follows:

- Another factor to investigate is that under the same load, the contact area for a smooth surface is more than the one for a rough surface. It can be explained by the fact that on a rough surface the rubber loses contact on the valleys on the surface and requires more load to reach to contact on those areas. For this purpose, two different surfaces are chosen, one as a single wave and the other as the combination of the single wave and a smaller wave. A similar load is applied to them and the contact area is calculated.
- The relationship between the penetration depth and applied pressure is also known to be linear. Here, the same procedure is used for finding this relationship, under different loads.
- One of the important geometrical properties of the surface is the ratio between the amplitude and the wavelength of the wave ($h/\lambda$). If $h/\lambda$ is the same for two different surfaces, the load required for the full contact is assumed to be the same. For investigating

this assumption, different surfaces with similar $h/\lambda$ ratio are imported into the ABAQUS model and the required load for reaching full contact is obtained for each one of them.

- Also, if the ratio between the amplitude and the wavelength is related to the ratio between the applied pressure and the elastic modulus of the rubber ($h/\lambda \alpha \sigma/E$), it is expected to reach to the full contact between the rubber and the surface.

- If the pressure is so high that full contact can be reached, from dimensional argument, hysteresis contribution to friction coefficient only depends on $h/\lambda$ and therefore surface roughness of all length scales are equally important.

# CHAPTER 5 - RESULTS

## 5.1 STATISTICAL CHARACTERIZATION OF A SURFACE

Statistical parameters are sale dependent and they vary depending on the sample length and from one location to the other. Figure 38 is demonstrating some of these parameters and their variation along a profile.

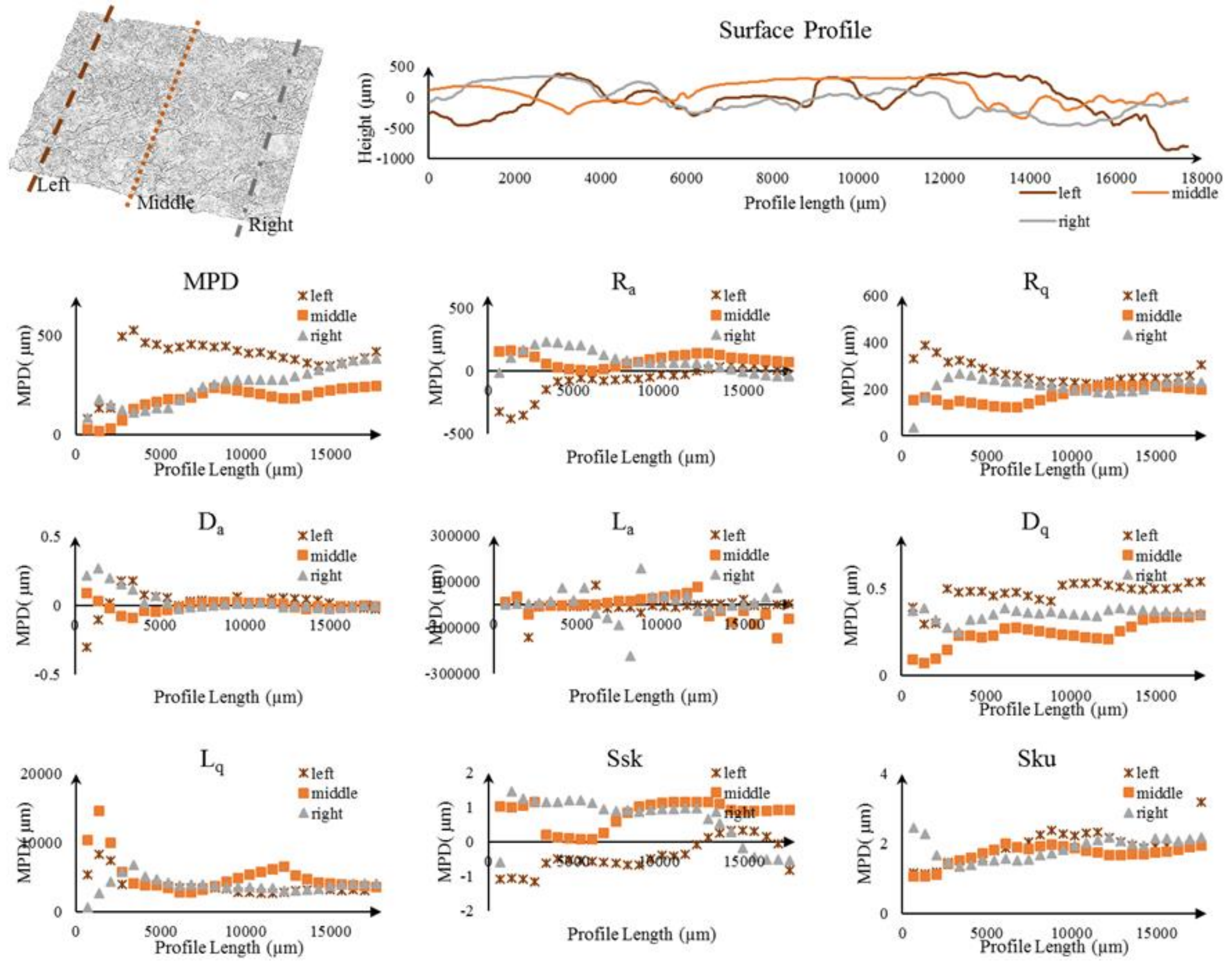


Figure 38. Representation of three 2D profiles of one surface through several statistical parameters

## 5.2 FRACTAL PARAMETERS

### 5.2.1. 1D PSD

Figure 39 shows plots generated with the 1D PSD method for one of the samples. The average signal was created as the average of all single-profile power spectral density graphs. To see how the average signal was positioned within all profiles, a collective graph with all profiles was created. Then the peak envelope (contours) of that graph were found and average signal plotted again. Two different linear regression fit were calculated: (i) including all values in the regression; (ii) including only the points that lie within the linear region (middle of the plot). Finally, the plot of phase information was depicted, which is a random oscillation around a constant value, as it should be for Fourier Transform of fractal data.

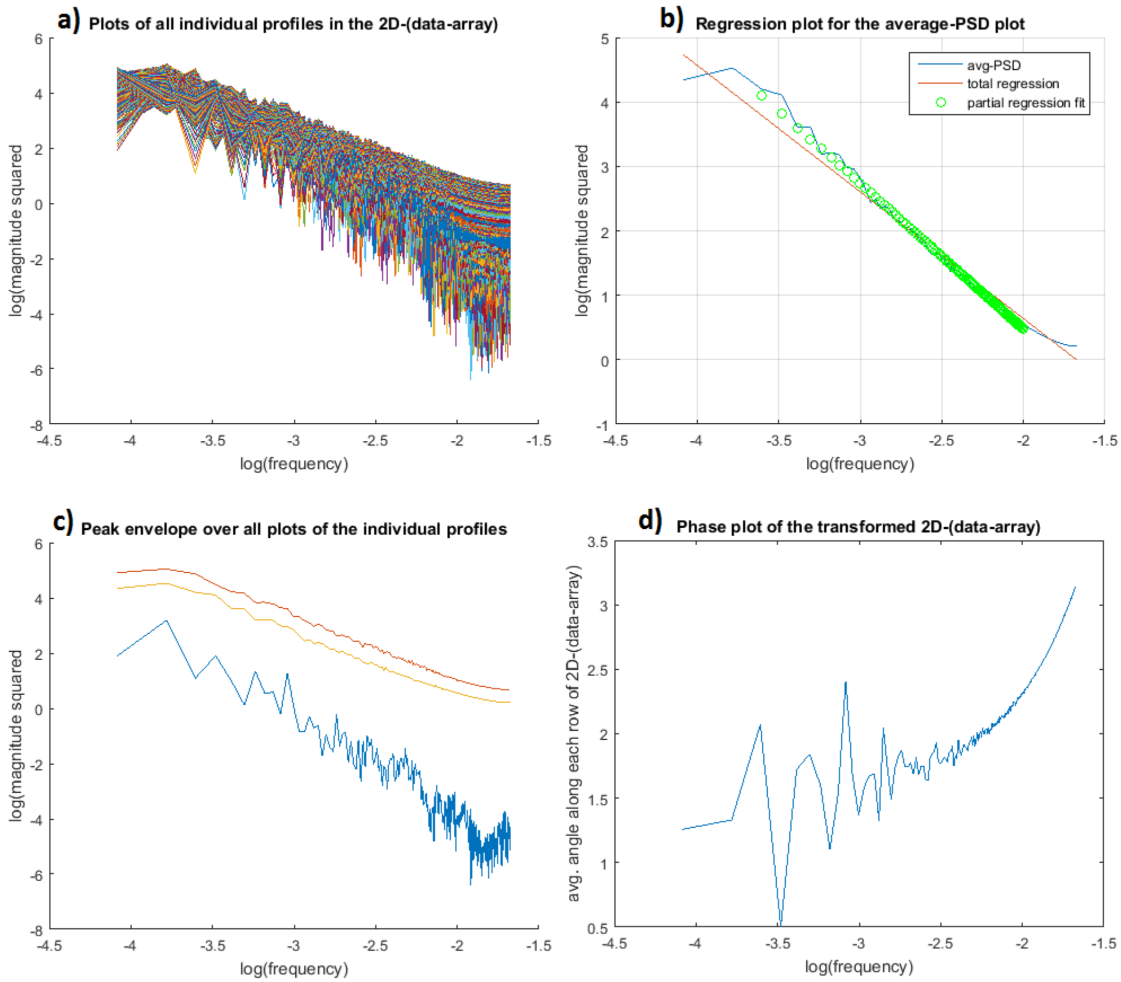


Figure 39. Plots generated with the 1D-PSD script for a randomly chosen data array: a) PSD of all individual profiles of a sample, b) Regression plot for the average PSD c) Maximum, minimum, and average PSD plots, d) phase information corresponding to the average

### 5.2.2. 2D PSD

Figure 40 shows graphs generated with the 2D PSD method for a randomly chosen sample. Subfigure (a) shows a typical power image resulting from the 2D Fourier Transform, in which the distribution of power is decreasing radially. Subfigure (b), phase image, is a corresponding phase information for 2D-FFT. Subfigure (c) shows that the value of the power spectrum averaged over all directions declines with frequency in 1/f manner. Finally subfigure (d), demonstrated the 2D PSD of the surface.

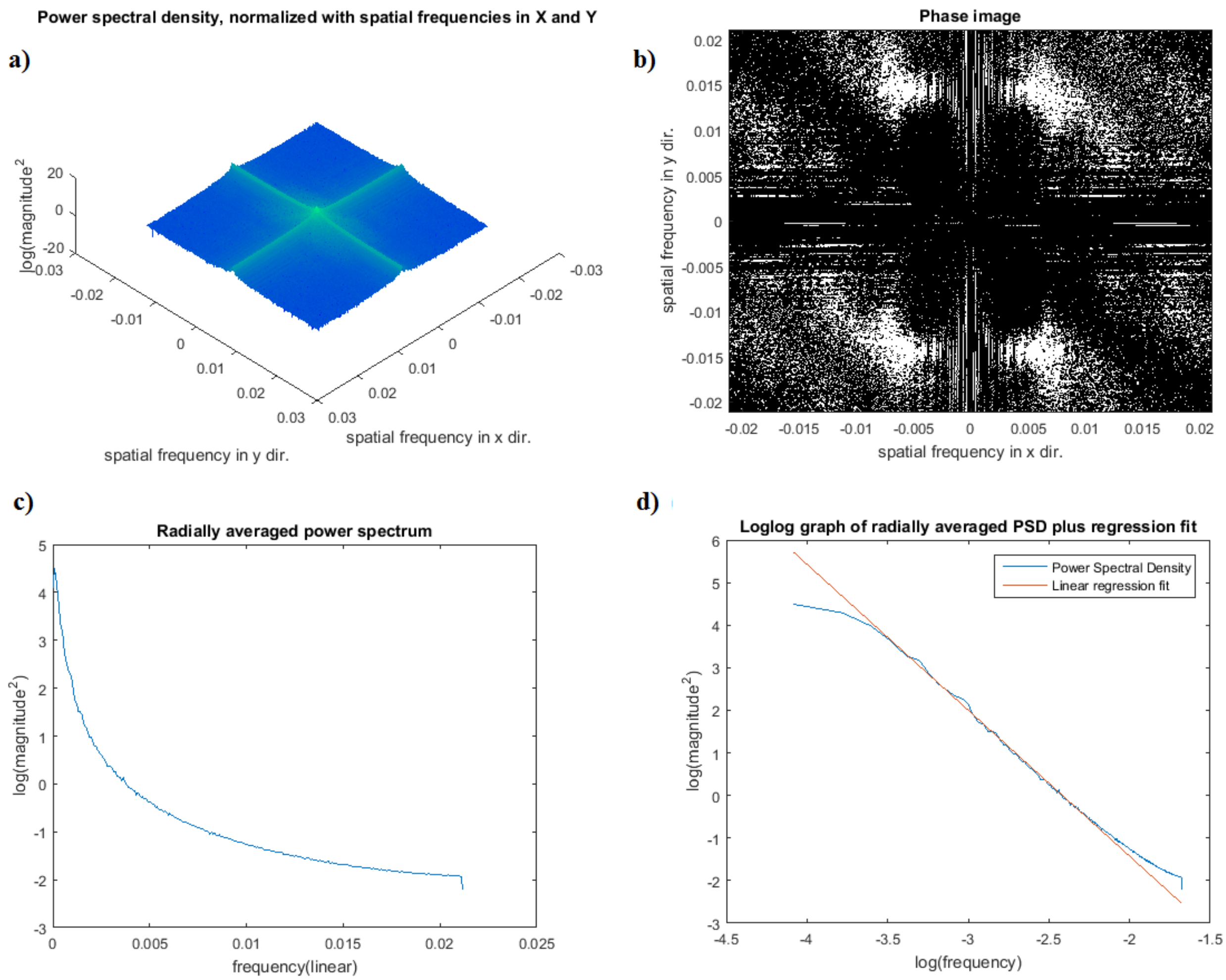


Figure 40. Plots generated with 2D-PSD method a) power image of the 2D surface, b) phase information resulting from the FFT, c) radial average of the power image shows a regular decline of signal's power in all directions, and d) PSD obtained by (log-log) plotting of power vs. frequency.

### 5.2.3. Roughness-length method

Figure 41 shows plots obtained from implementing the roughness-length method to find the fractal dimension of a set of profiles. Subfigure (a) shows the log-log plot of length of window vs. rms for a profile randomly chosen from all data sets. This line should be as close to a straight line as possible (which would indicate perfect fractal behavior). All such plots plotted together give the subfigure (b). The third subfigure shows the variation of D value for all profiles (x axis is the profile number along the data set).

***Dependence of results on the choice of the smallest window size***

After investigating the difference in results depending on the size of the smallest window while fixing the largest window to 20% of the total number of points, it was found that the mean value of fractal dimension increases for increased size of smallest window. Similar results has been obtained for the variance of all fractal dimension values. The fractal dimension range gets narrower as the size of smallest window decreases.

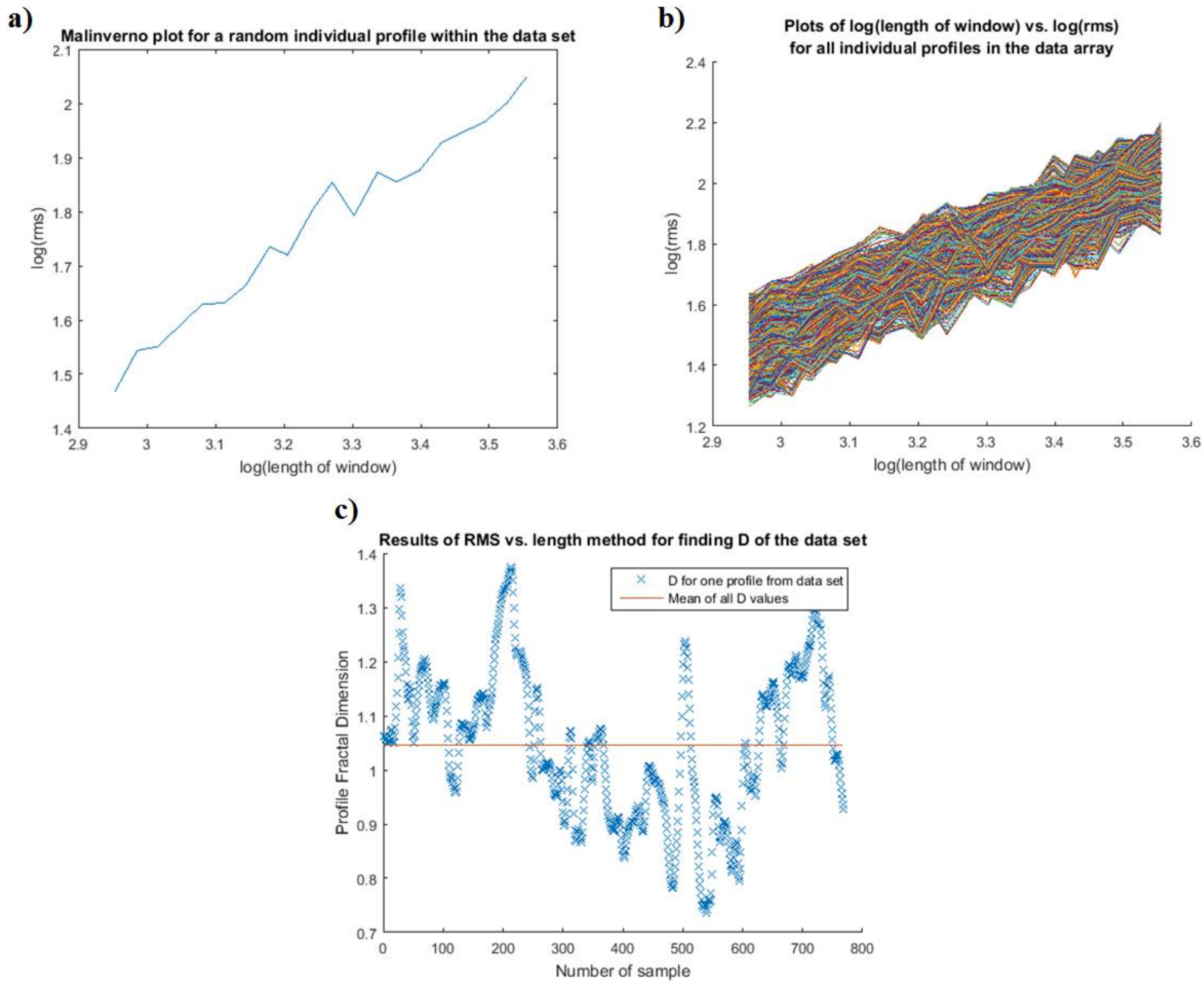


Figure 41. Graphs generated with the roughness-length method, a) plot shows a log-log plot of length of window vs. rms for one profile; b) collective plot of all profiles in the data set, and c) the distribution of D values in the data set.

### 5.2.4. Tessellation (Projective Covering) method

Figure 42 shows an example of a plot generated with the Projective Covering method for a sample surface. The results achieved from all of the samples are similar to S-shaped results demonstrated here. However, the amplitudes and slopes were different. It can be seen that clearly there is more than one tendency in the values and by adjusting the amount of the linear regression fits, three-segments seems to be satisfactory. Figure 42 gives a visual representation and comparison of different number of linear segments that can be used.

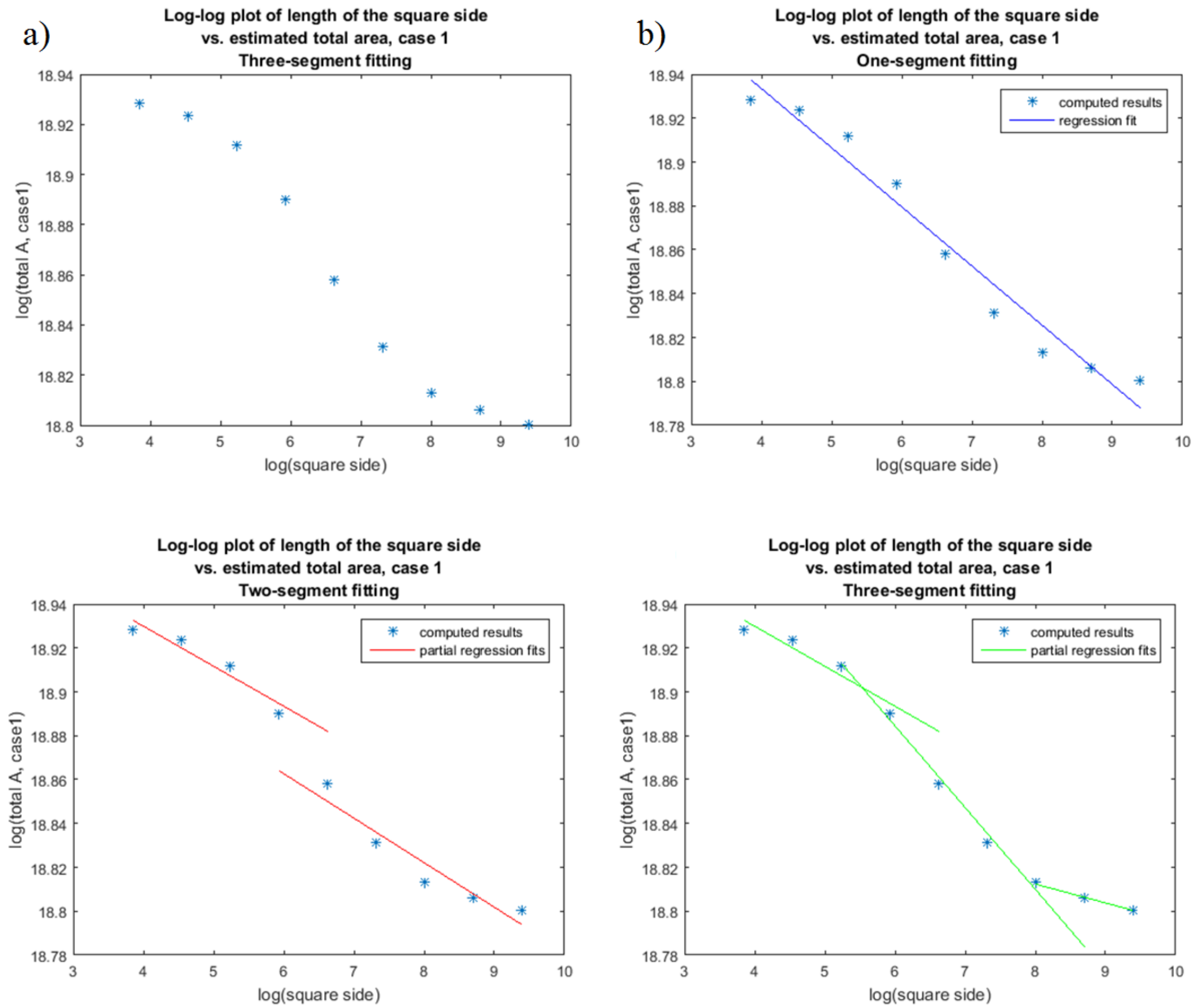


Figure 42. Projective Covering method; a) data points obtained by plotting total area estimations vs. grid size used, b) linear regression fit, c) two-segment regression fit, and d) three-segment regression fit.

### 5.2.5. Comparison of the methods

In this part the results achieved from the different methods, values of fractal dimension and fractal thresholds are compared with each other. This includes four power law methods and structure function method.

To find surface fractal dimension values, the inequalities relating fractal dimension of a profile to a surface is used. Hence, the average fractal dimension value of the ranges is chosen as the fractal dimension of the surface for 1D methods (1D-PSD, RMS-roughness and structure function). For the sake of comparison the fractal dimension values from Projective Covering method are taken from the second segment of the linear regression fit. The results of these comparisons are depicted in Figure 43.

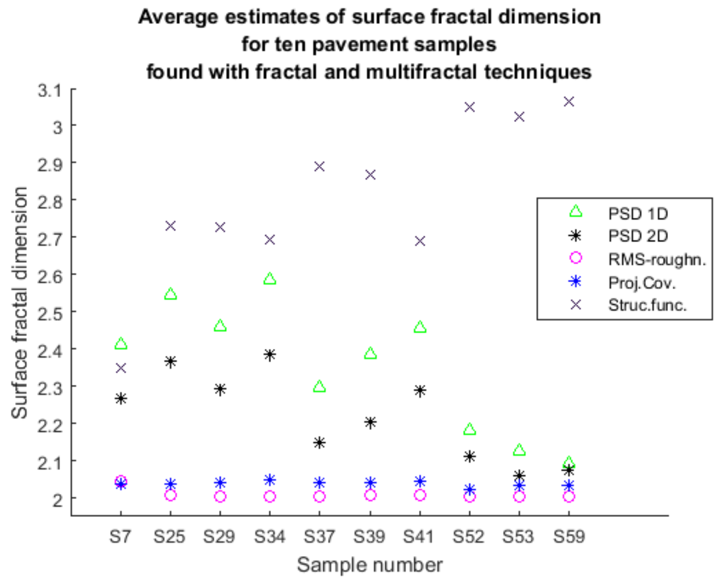


Figure 43. Graphical representation of fractal dimension obtained from different methods in 10 random samples

As it can be seen the results obtained from structure function method are much more than the other methods. RMS-roughness and Projective covering methods give similar values, near 2, for most of the samples. However, the results of 1D and 2D PSDs are in the middle and in the range suggested in the literature.

For finding the thresholds of the fractal behavior, 1D PSD, 2D PSD and Projective Covering methods are used (see Figure 44). Structure function and RMS-roughness methods do not provide sufficient information about fractal nature's thresholds. Overall, the values of fractal ranges are in agreement with each other. The differences in the limits can be explained by the differences in the employed method definitions, e.g. frequency increment (PSD methods), grid-distance (Projective Covering method).

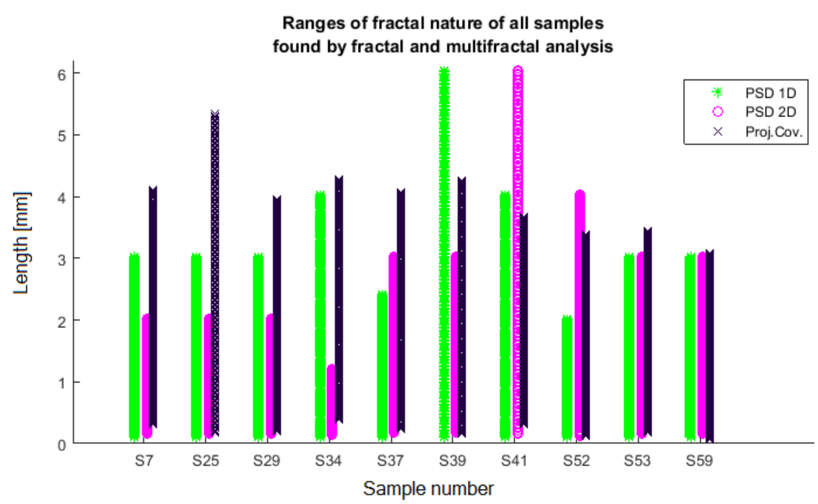


Figure 44. Graphical representation of fractal nature ranges found with three fractal methods for 10 samples

### 5.2.6. Estimation of other fractal parameters (other than D)

Beside fractal dimension and the threshold of fractality of the surfaces, other parameters are required for defining a unique surface. Here, parameters such as power scaling constant G (for two PSD methods), proportionality constant C (for Projective Covering method), and topothesy K (for Structure Function) are calculated.
In case of proportionality constant C, which is the intercept of linear regression fir on y axis to the Projective Covering log-log plot, the second segment (out of three) is considered, since it is corresponding to the same scale as other methods (about 0.2-4.1 mm); so that the results of the same scale are compared for different methods.
Overall, C and K values were similar for all samples - C around 19.00 and K around 0.80. This might indicate that either the two fractal parameters are insensitive to the changes of fractal nature within the same type of surface (asphalt pavement), or the surfaces analyzed are similar in the fractal nature (similar heights of peaks). In contrary, G values, for 1D PSD and 2D PSD methods, varied strongly, by a few orders of magnitude, e.g. for a random surface $G_{1D}$ = 1.9123 e-9, while for another $G_{1D}$ = 3:9415 e-5. This shows that the power spectral density is more sensitive to changes in fractal nature.

## 5.3 MULTI-FRACTAL NATURE OF THE SURFACES

In this part, the scale-dependency of the fractal nature of the samples and the variation of fractal dimension in different direction are investigated.

### 5.3.1. Scale-dependent fractal nature of pavements

Figure 45 shows the structure functions obtained for a random surface among the available samples. It can be seen that the structure function plots for all samples are linear in the beginning of the graph until approximately $\tau$ = 0.189mm, for this sample. After $\tau$ = 0.189mm the plots follow nonlinear trends. Depending on the profile, there are one or more shorter linear fragments, either with positive or negative slopes. However, considering the average of the structure functions of individual profiles, it is possible to define two fractal dimensions one for micro-texture and one for macro-texture.

For fully understanding this behavior, new data was collected with different magnifications. However, no persistent trail on changes of fractal dimension with increasing magnification is found. The change in fractal nature with change of resolution is not also consistent among different methods. However, it can be seen that the changes of fractal dimension values within one sample, obtained by different methods, are not significant.

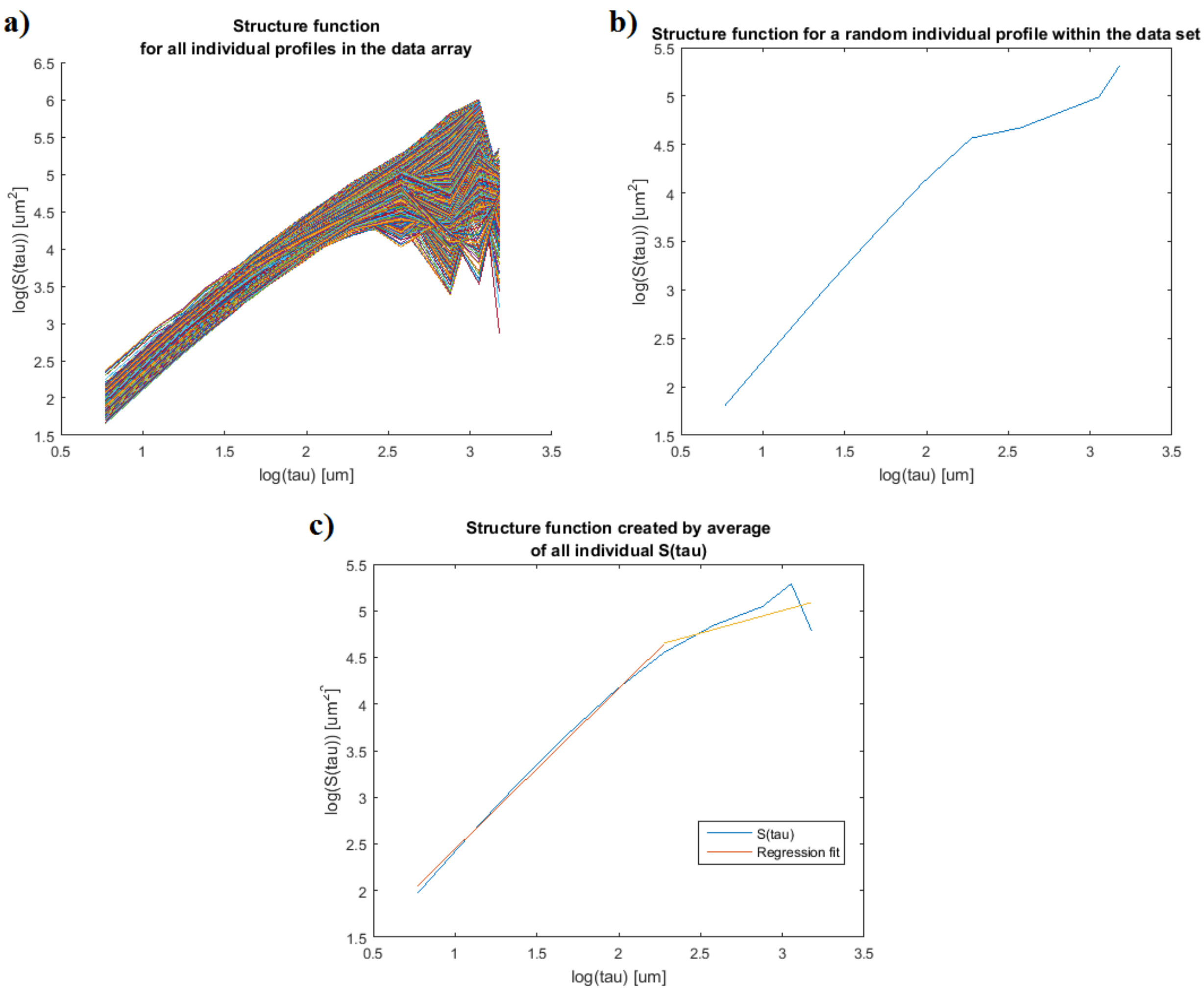


Figure 45. Structure function of a) all profiles in the area, b) a randomly chosen profile in the area, and c) average of all structure function graphs.

### 5.3.2. Anisotropy: driving direction on fractal pavements

After obtaining the fractal dimension for different directions in each sample, the polar plot or rose plot of the results is depicted (Figure 46). This graph is demonstrating the dependency of fractal dimension on the direction of measurement, using three different methods (1D PSD, RMS-roughness, and structure function).

In order to find the driving direction of each sample, fractal dimension values are plotted in each direction separately (Figure 47). The area that indicates the minimum fractal dimension in different methods is chosen as the driving direction (20-60◦ in Figure 47). It worth mentioning that for some of the samples the driving direction was not apparent, e.g. in the case that several directions showed distinctly lowered fractal dimension. This can be explained by the fact that some of the samples were not taken from the wheel path and therefore the effect of tire rolling on them is less than the others. The tendency of RMS-roughness results being the lowest and 1D-PSD results the highest is consistent with the previous results.

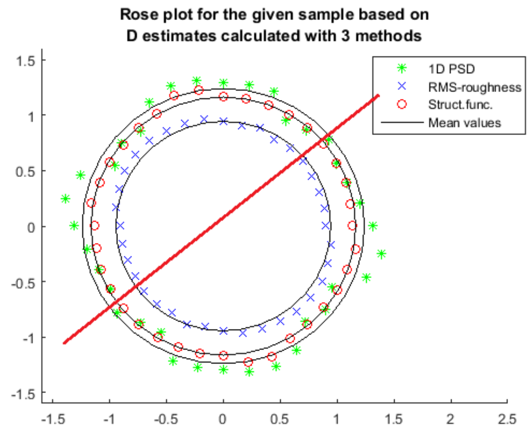


Figure 46. Angular histograms showing the magnitude of fractal dimension in different directions, with circles showing the mean value of D in all directions for each method

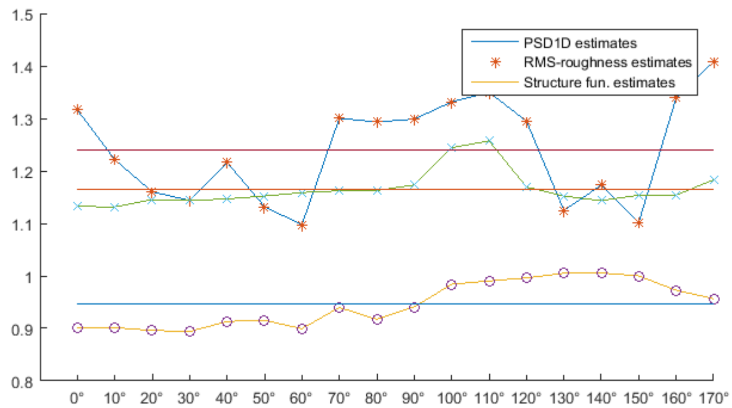


Figure 47. Results of the driving direction analysis shown in non-circular form

## 5.4 3D FRACTAL SURFACES

Here the results of the four methods of BFIS model, iFFT, Blackmore, and BFIS enhanced Blackmore models are presented.

### 5.4.1. BFIS model

Figure 48 is demonstrating the surfaces generated with the BFIS algorithm after subsequent iterations of the interpolation procedure. The surface in the subfigure (a) is a plot of filtered data set, including 9 points from the raw data. The next subfigures are depicting the following iterations to generate the surface with the same resolution as the original data (from macro-texture in first iteration to micro-texture in the last one).

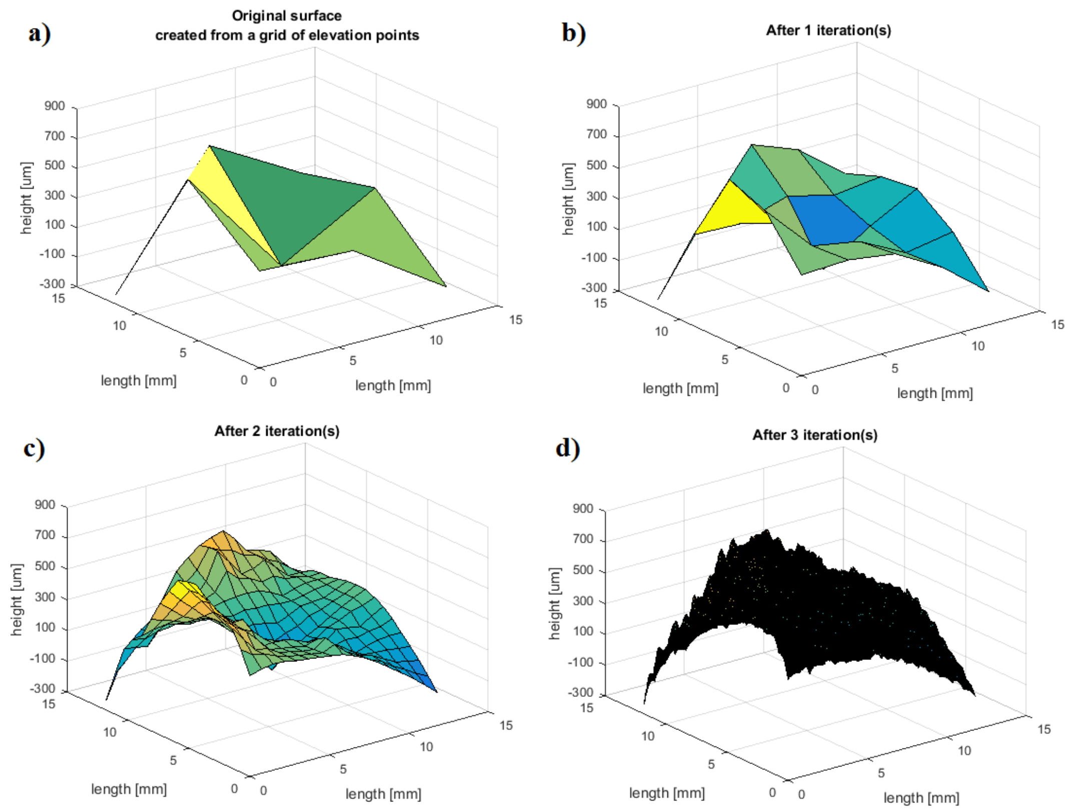


Figure 48. BFIS a) original surface containing only 9 points from the raw data, b) first iteration c) second iteration, and d) third iteration.

### 5.4.2. IFFT model

Figure 49 shows the generated surface using IFFT, its contour and the input PSDs. It can be seen that the surface is not completely random, i.e. its peaks are aligned in two distinct directions. The input parameters - fractal dimension, D, values and power scaling constants, G – affect the output. Increasing fractal dimension leads to an increase in the height of the surface, simultaneously making peaks more flat, reaching the same height as the fractal dimension reaches to the next integer. Also, decreasing power scaling constant made the surface appear less random and more creased along one direction.

### 5.4.3. Blackmore anisotropic surface simulation

Figure 50 is presenting two surfaces and their corresponding contour graphs resulting from the Blackmore and Zhou's anisotropic model. The two surfaces are generated using different number of data points and therefore their results vary dramatically. Although the surface in subplot (a) appears anisotropic (see subplot (b)), the surface generated with the same input parameters, but increased number of points, shows a distinct direction of peaks (see vertical lines in subplot (d)). Numerical input parameters of this algorithm, α, β, n, and D, influences the output by either changing the height of the peaks (α), or the shape of the peaks (n) or both (β and D) cause a change in height and pattern of the peaks.

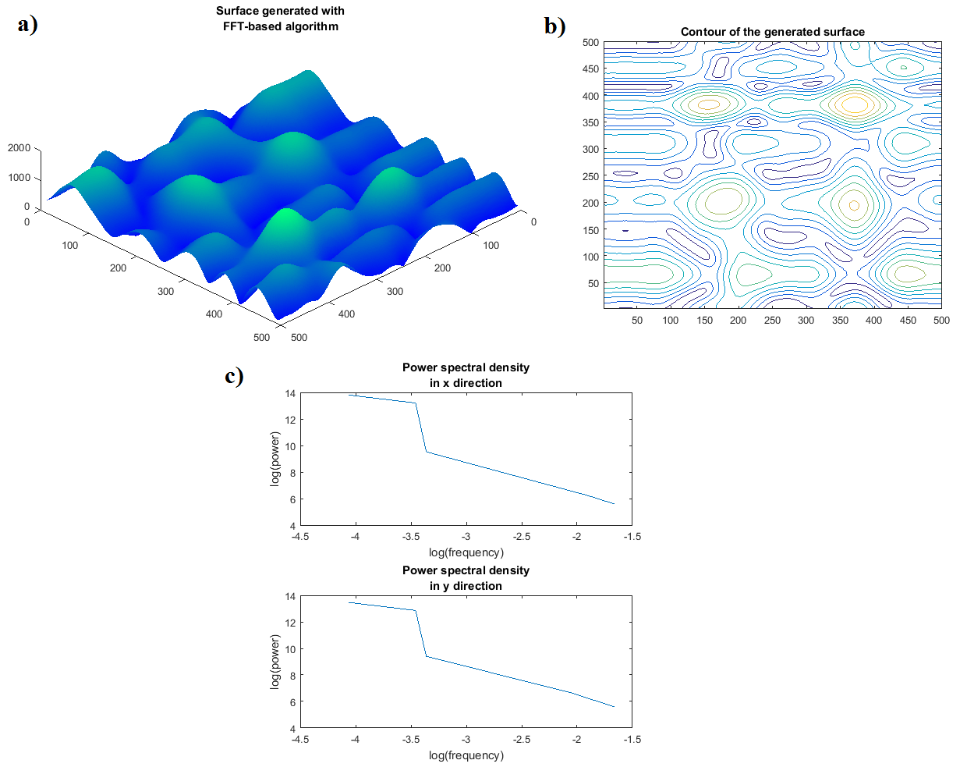


Figure 49. IFFT method, a) generated surface, b) contour graph of the surface, c) PSDs in two directions-inputs

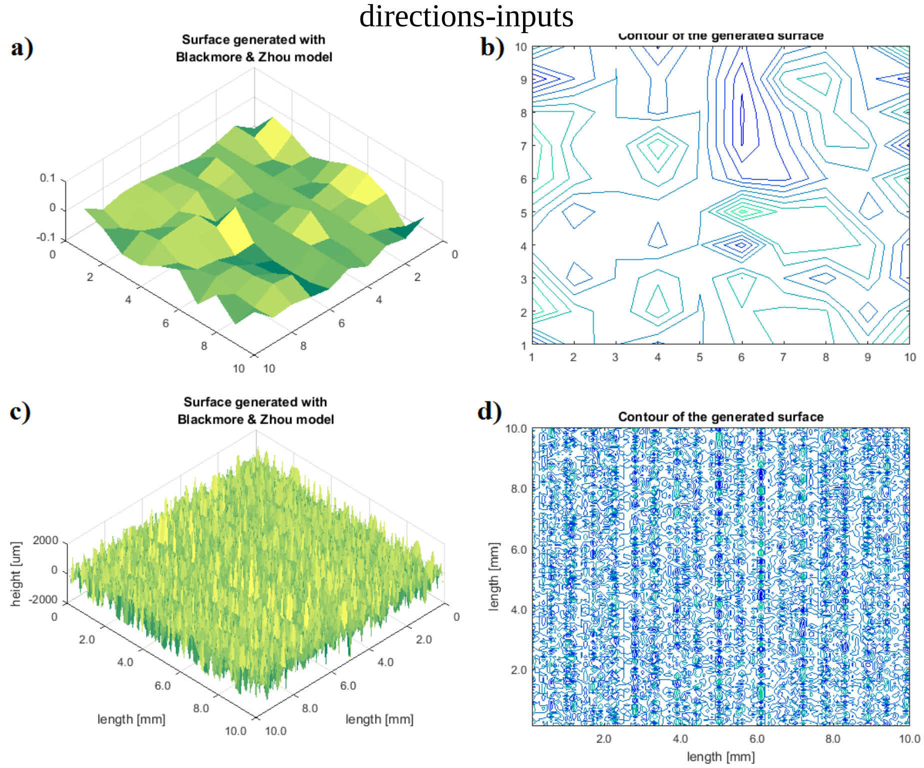


Figure 50. Blackmore algorithm, a and c) surface based on 81 and 1600 data points, b and d) contour map of the surfaces in a and c

### 5.4.4. Combination of simulation and interpolation

The last simulation technique employed here is the combination of BFIS and Blackmore methods (Figure 51). First, a few points are required to build the base surface for iteration which is generated with the Blackmore and Zhou's anisotropic model. Then the interpolation is iterated (subplots b, c, and d). As a combination of two methods, this algorithm has the largest number of input parameters. All parameters, belonging to both BFIS and Blackmore models, affect the surface similar to the way they do when the methods are not combined.

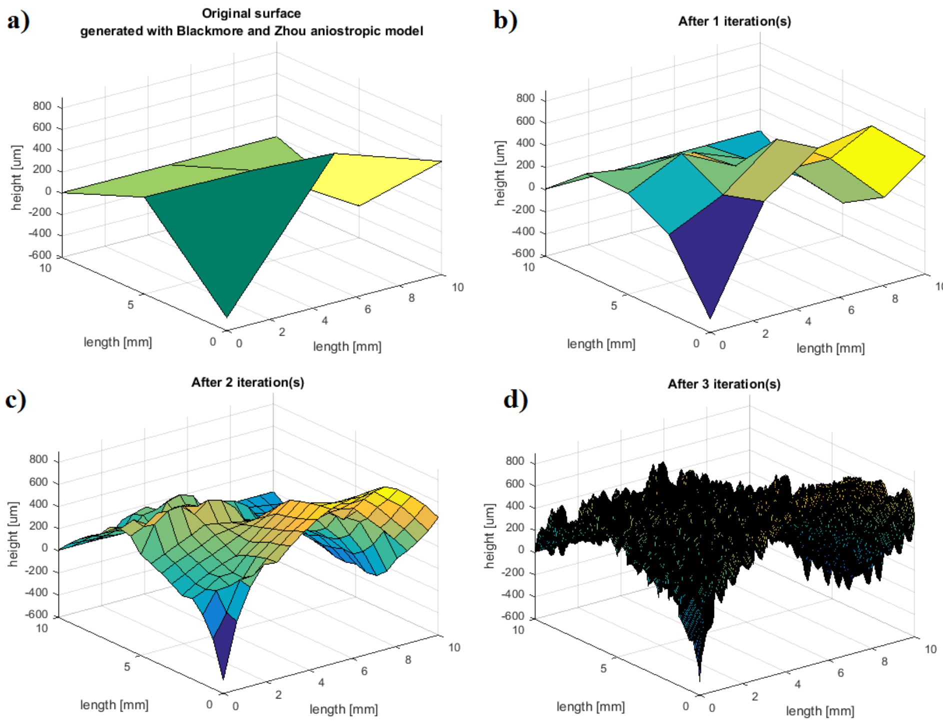


Figure 51. BFIS enhanced Blackmore algorithm, a) surface generated with Blackmore algorithm, consisting of 9 points in total, surface generated after one (b), two (c), and three (d) BFIS interpolation iterations.

### 5.4.5. Validation of the surface structure

Here, the results of the validation of the four surface generation algorithms are presented. First, the surface of one of the pavement samples is modelled using interpolation and simulation scripts. Then, the results of the fractal and statistical parameters calculated for the presented models of the sample are compared with each other. Figure 52 shows the four models and the original surface based on the experimental data.

IFFT model seems to have the most similar texture to the raw surface, with round peaks. The BFIS-enhanced Blackmore model seems to curve to the sides. Blackmore and Zhou's model does not show any locally large irregularities, which is not a good local irregularity representation. However, its combination with BFIS is a better illustration of the surface.

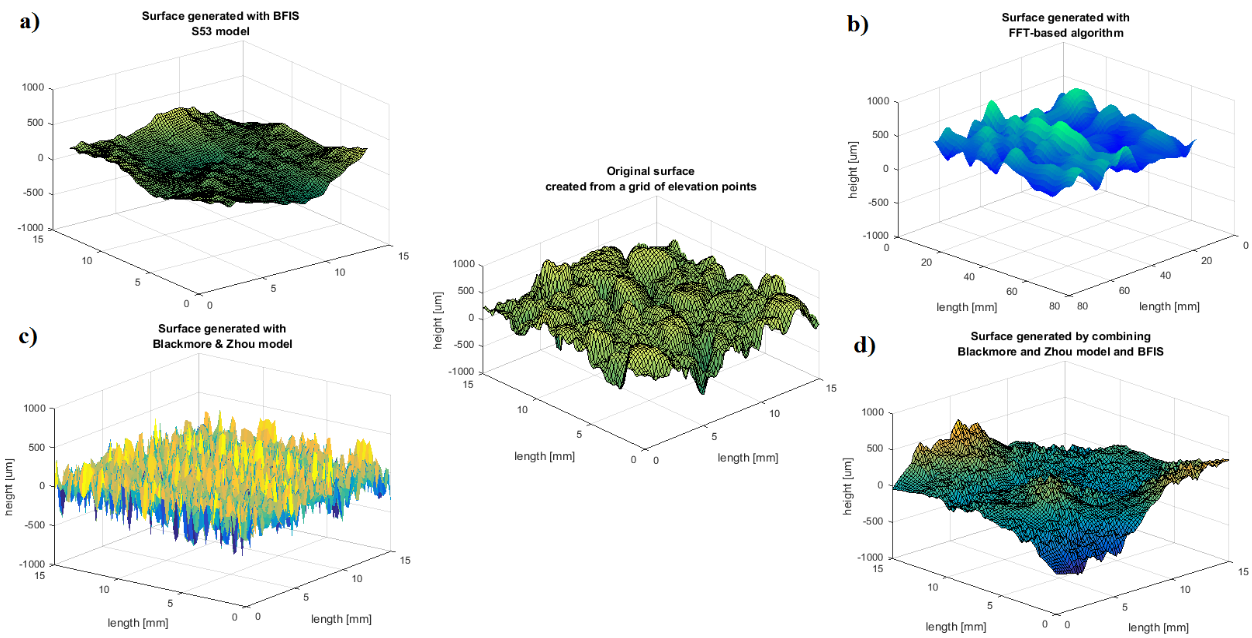


Figure 52. Four models of a sample of the measurement data (in the middle); Using a) BFIS interpolation, b) iFFT simulation, c) Blackmore and Zhou's anisotropic model, and d) Blackmore and Zhou's model enhanced with BFIS interpolation;

### 5.4.6. Fractal analysis of generated surfaces

Comparing the fractal dimension estimation, IFFT shows the minimum relative errors when compared to the original surface, while the maximum error is achieved for Blackmore algorithm (Table 6). BFIS enhanced Blackmore model performs better that non-enhanced, but the relative error is still large (up to 51:36%). This might be due to the unsuitability of the Blackmore model for pavement surface simulation or the selection of the input parameters, making the model susceptible to random variations of the output.

Comparing the fractal analysis techniques, the projective covering technique gives the lowest error for all models, followed by the Structure function method. Both PSD and RMS-roughness methods give a high relative error for BFIS, BFIS enhanced Blackmore, and Blackmore models. According to 1D PSD, 2D PSD, RMS-roughness, and Projective Covering techniques, IFFT surface is the best model for the raw data. BFIS model is better if only the Structure Function results are considered.

Table 6. Relative error in fractal analysis of the generated surfaces

| Fractal technique | Relative error | | | |
|---|---|---|---|---|
| | BFIS | IFFT | Blackmore | Enhanced Blackmore |
| **1D PSD (X/Y dir.)** | 32.8% / 54.5% | 0% / 0% | 150.2% / 127.7% | 48.5% / 51.3% |
| **2D PSD** | 20.9% | 8.3% | 79.6% | 23.8% |
| **RMS-roughness (X/Y dir.)** | 36.3% / 23.6% | 4.61% / 9.52% | 41.8% / 72.3% | 63.9% / 29.7% |
| **Projective covering** | 2.3% | 1.98% | 4.52% | 2.21% |
| **Struc. Func. (X/Y dir.)** | 13.7% / 3.66% | 2.3% / 20.4 % | 52.7% / 93.9% | 10.4% / 37.2 % |

### 5.4.7. Statistical analysis of the generated surfaces

There are significant differences between values of texture parameters for surface models and original surface. Surface skewness ($S_{sk}$) gives the largest error. Smallest relative errors are in estimation of RMS roughness ($S_q$). Overall, BFIS enhanced Blackmore model has the least error and closest values to the original surface, while IFFT is showing the worst results (Table 7).

Table 7. Relative error of statistical analysis of the generated surfaces

| | Relative error | | | |
|---|---|---|---|---|
| **Texture parameters** | BFIS | IFFT | Blackmore | Enhanced Blackmore |
| $S_a$ | 26.02% | 50.62% | 26.49% | 33.02% |
| $S_q$ | 34.76% | 26.83% | 27.21% | 30.12% |
| $SR_{3z}$ | 81.40% | 36.56% | 6.91% | 56.04% |
| $SR_{max}$ | 66.81% | 56.49% | 40.64% | 34.05% |
| $SR_{pm}$ | 9.26% | 134.30% | 81.13% | 28.38% |
| $SR_{tm}$ | 80.54% | 38.74% | 3.87% | 54.53% |
| $S_{sk}$ | 182.48% | 175.94% | 101.41% | 56.54% |
| $S_{ku}$ | 58.77% | 66.33% | 43.51% | 20.66% |

## 5.5 FRICTION MEASUREMENT

The friction tests were performed on pavement samples obtained from MSU, in different conditions of dry, wet, using soap and detergent. The purpose of these tests is to separate the effect of adhesion and hysteresis friction. Figure 53 is showing a part of the results obtained by BPT in different conditions for HMA. It is evident that British Pendulum Number in Dry condition is more while in presence of detergent on the surface it reached the least value which can be considered as the hysteresis component.

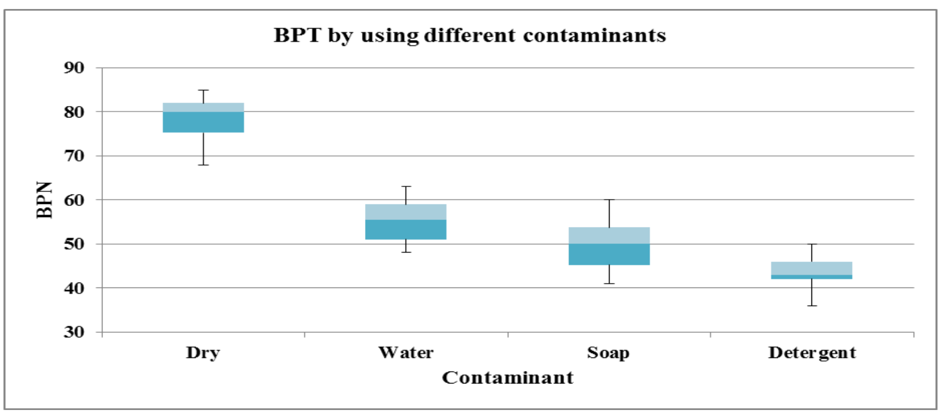


Figure 53. BPN values for different conditions of dry surface and contaminated surfaces of HMA

## 5.6 PAVEMENT MICRO-TEXTURE EFFECT ON HYSTERESIS COMPONENT

Although the UMAT subroutine has been prepared for this project, unfortunately, due to the lack of time, the model was only run with Prony series. Therefore, the following results are all obtained from the quasi-static explicit analysis using Prony series as material properties.

### 5.6.1. Hysteresis component of single wave surfaces

After running the model, the hysteresis component can be obtained by creep dissipation defined in the ABAQUS software.

$$E_c = \int_0^t (\int_V \sigma^c : \dot{\varepsilon}\, dV)\, dt$$

In which $E_c$ is the dissipated energy by time-dependent deformation (Hysteresis), $\sigma^c$ is the applied pressure, and $\dot{\varepsilon}$ is the strain variation by time.

For evaluation of the quasi-static mode of the model few factors should be controlled. The first one is that the total energy should be constant. Also kinetic energy should be less than 5% of the internal energy, as it can be seen in Figure 54.

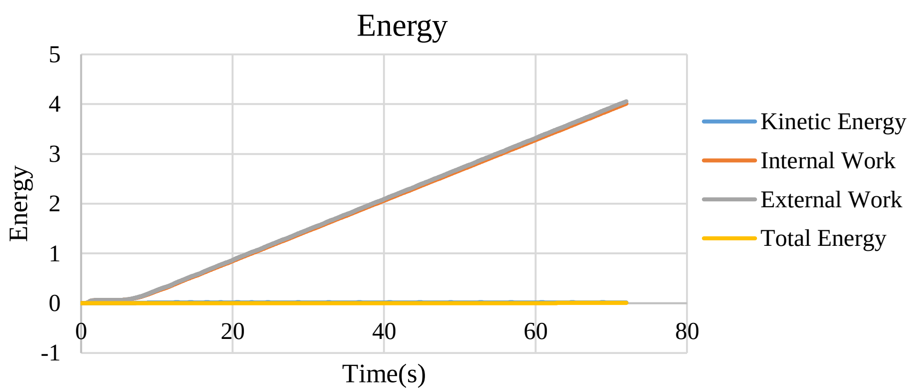


Figure 54. Energy variation by time

Also, the penetration of the rubber at the bottom can be useful for verification of the model. In sliding mode, the maximum penetration of different nodes at the bottom should be the same and reach to a constant value (see Figure 55).

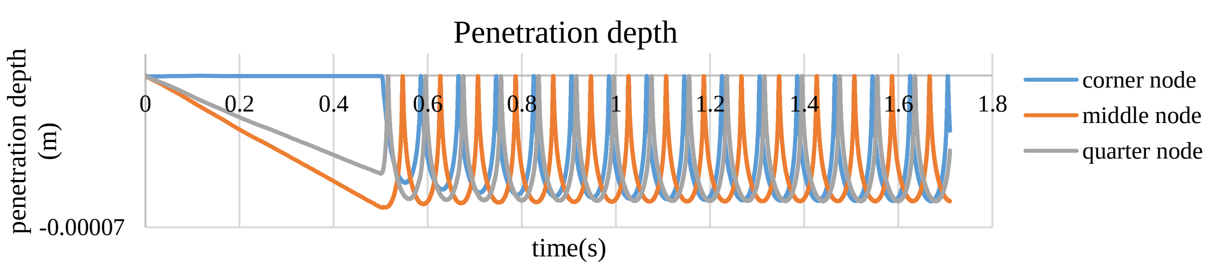


Figure 55. Rubber penetration depth

### 5.6.2. Hysteresis calculation for multiple wave surfaces

At this phase the hysteresis component is calculated for different combinations of the surface. For this purpose λ/h=8 has been chosen based on the PSD of the measured surfaces. Four sinusoidal waves with wavelengths of 4mm, 1mm, 0.5mm, and 0.25mm are chosen and surfaces with different combinations of them are constructed with Matlab code. The surfaces are then imported into Autocad so that the input file for the ABAQUS model could be obtained. After running the model, it is observed that for surfaces with zero phase angle between the waves the creep dissipation is almost equal to the summation of the creep dissipation of the individual waves (as it can be seen in Figure 56).

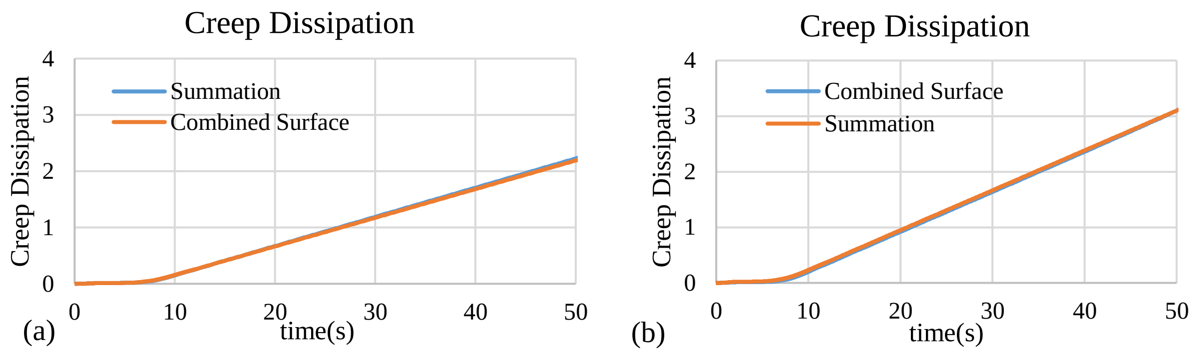


Figure 56. Creep Dissipation for combination of (a) 4mm and 0.5mm wavelength surfaces (b) 4mm, 0.5mm, and 0.25mm wavelength surfaces

However, in the presence of phase angle between the surfaces the creep dissipation of the combined surface is less that the summation of the individual surfaces. This can be an important factor which seems to be neglected in other. After running the model for different surface combinations (only the combination of two waves has been considered at this time), it is found that this effect can be rather significant as it is demonstrated in Figure 57.

As it can be seen, the energy dissipation can change by phase angle between two different waves. The value of these changes is dependent on the wavelength of the second wave (considering the same h/λ ratio):

Relative difference $_{2mm}$ > Relative difference $_{1mm}$ > Relative difference $_{0.5mm}$

In addition, the direction of the phase angle can affect the results slightly.

### 5.6.3. Investigation of the relationship between contact area and applied pressure

As it was mentioned before, it is assumed that the contact area and applied load should have a linear relationship when the load is small and the contact area is not close to nominal contact area, A0. After running the model for a certain surface, with different applied loads and obtaining the contact area ine each case, a linear relationship has been found between the contact area and applied load. Figure 58 is demonstrating this relationship. Graphs on the left show the variation of contact area by different loads in time and the graphs on the right show the linear relationship between the load and contact area.

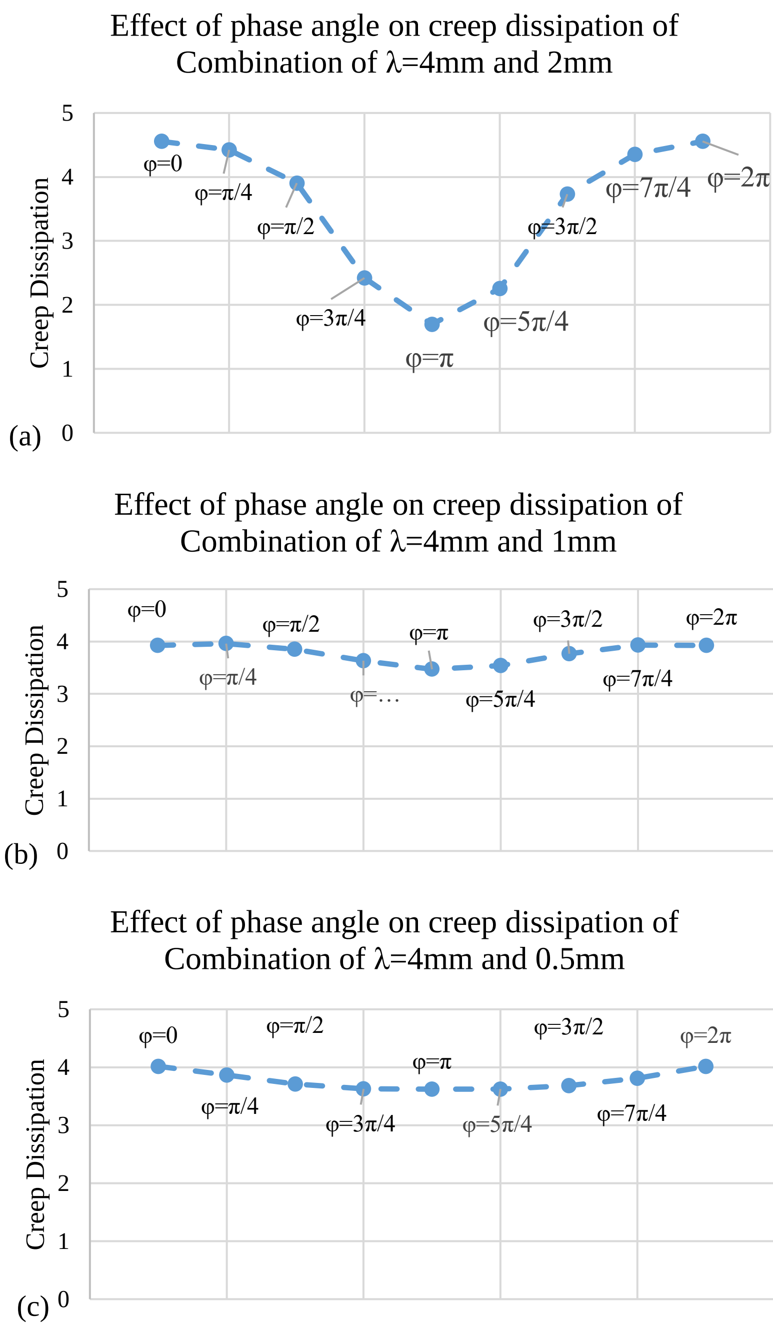


Figure 57. Effect of phase angle on creep dissipation of Combination of (a) λ=4mm and 2mm, (b) λ=4mm and 1mm, and (c) λ=4mm and 0.5mm

Also, the contact area for a certain load is known to be more for a smooth surface in comparison to a rough one. This assumption is proven by the model as it is shown in Figure 59.

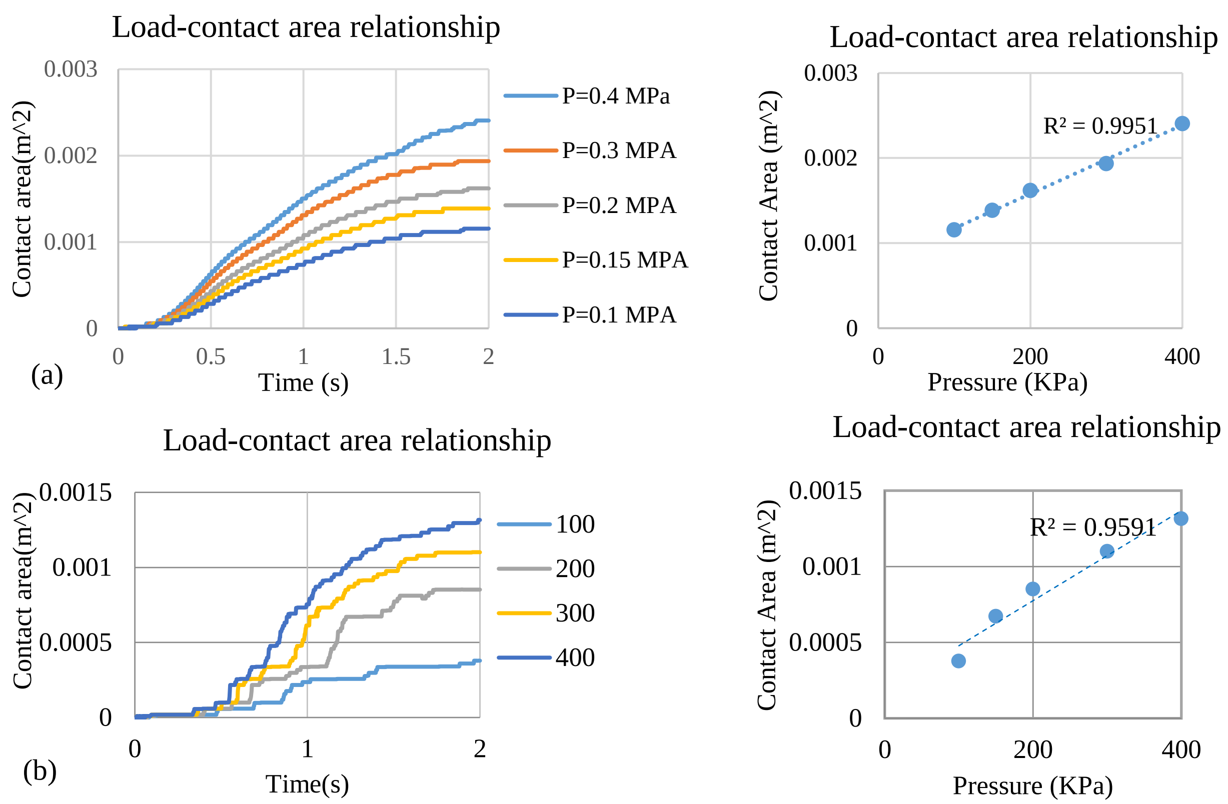


Figure 58. Load-contact relationship (a) for λ=4mm (b) for combination of λ=4mm, λ=1mm and λ=0.25mm.

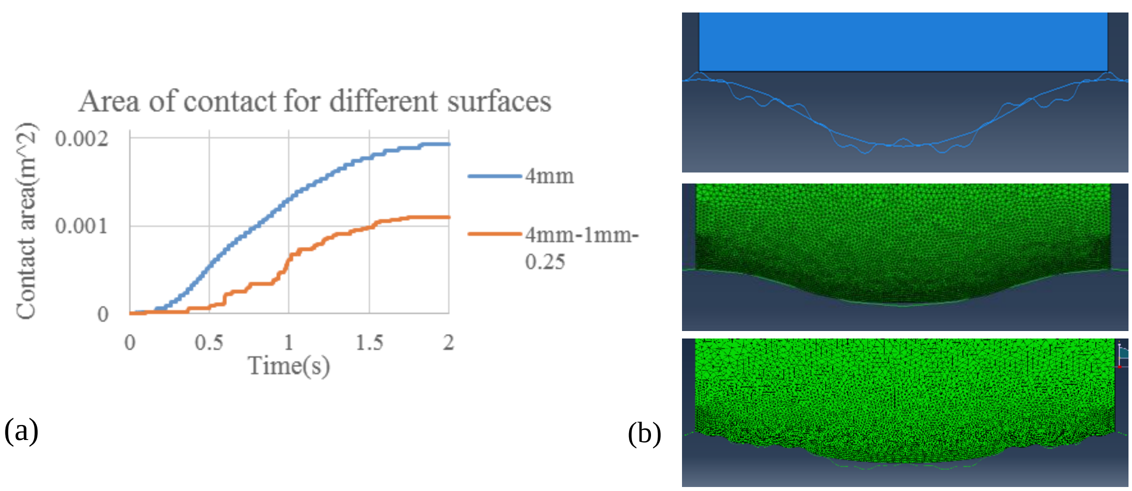


Figure 59. Comparison of area of contact for smooth and rough surfaces

### 5.6.4. Investigation of the relationship between penetration depth and applied pressure

The relationship between the penetration depth and applied pressure is also known to be linear. As it can be seen in Figure 60, this assumption holds in this model as well.

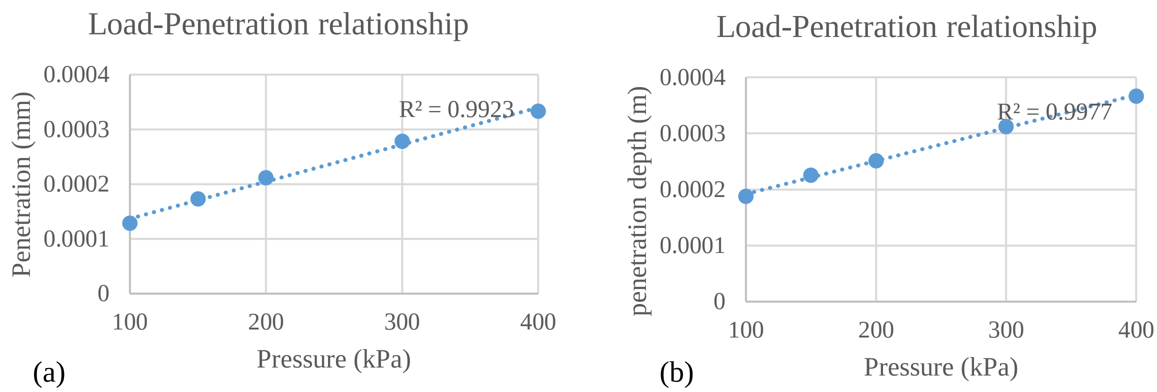


Figure 60. Load-Penetration relationship for (a) λ=4mm and (b) combination of λ=4mm, 1mm, and 0.25 mm

### 5.6.5. Investigation of the relationship between h/λ and applied pressure

It is assumed that if the ratio between the amplitude and the wavelength is related to the ratio between the applied pressure and the elastic modulus of the rubber ($h/\lambda \propto \sigma/E$), the full contact between the rubber and the surface should be reached. Also, if h/λ is the same for two different surfaces, the load required for the full contact would be the same. After running the model it could be seen that these assumptions are valid (see Figure 61 (a)). In addition, a linear relationship has been found between the required pressure for full contact and h/λ ratio (see Figure 61 (b)).

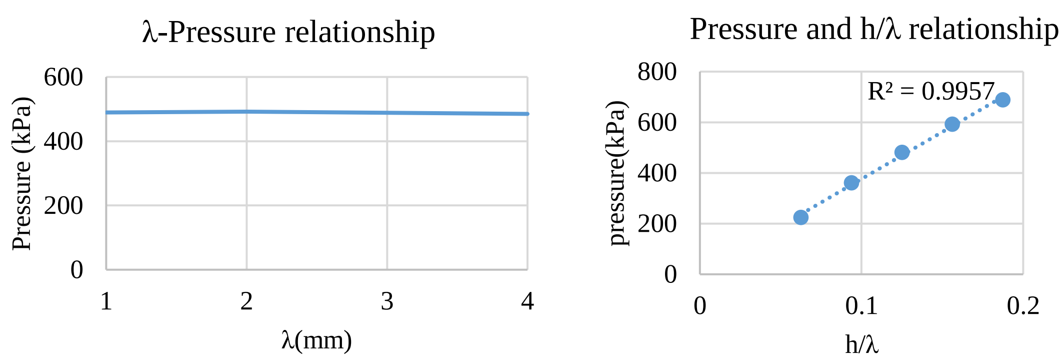


Figure 61. (a) λ-Pressure relationship for different surfaces with the same h/λ ratio when they reach the full contact, (b) relationship between the required pressure for full contact and h/λ ratio.

### 5.6.6. Investigation of the relationship between h/λ and Hysteresis

It is suggested by Persson (2001) that if the applied pressure is high enough to reach the full contact, from dimensional argument, hysteresis contribution to friction coefficient only depends on h/λ ratio. Therefore, surface roughness of all length scales are equally important. However, the results of the model for different h/λ ratio, in full contact, shows the hysteresis and creep dissipation is different for different cases. Figure 62 shows the results of the model for this case.

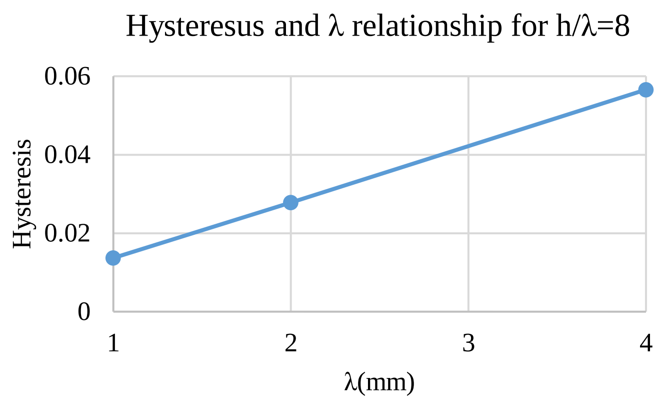


Figure 62. Hysteresis variation for different surfaces with the same h/λ ratio

In fact it can be seen that if the h/λ ratio is the same for two surfaces, the required pressure to reach to full contact is the same. However, the ratio between the hysteresis of the two cases is equal to the ratio between the heights (h1/h2) which is equal to the ratio between their wavelengths (λ1/λ2). This can be explained by the definition of dissipated energy by time-dependent deformation:

$$E_c = \int_0^t \left( \int_V \sigma^c : \dot{\varepsilon} \, dV \right) dt$$

In which $E_c$ is the dissipated energy by time-dependent deformation (Hysteresis), $\sigma^c$ is the applied pressure, and $\dot{\varepsilon}$ is the strain variation by time.
By keeping the h/λ ratio constant between two cases $\sigma^c$ is the same, however $\dot{\varepsilon}$ is changing.

### 5.6.7. Subroutine verification

As it was explained in**Error! Reference source not found.** , the UMAT subroutine consists of hyperelastic and viscoelastic parts (H-V). Before using a UMAT subroutine in the model, few steps should be taken. (i) Finding the constants required for hyperelastic constitutive model. (ii) Finding the constant for viscoelastic part of the constitutive model. (iii) Controlling the response by comparing the results of the UMAT and built-in Yeoh model in ABAQUS. (iv) Controlling the response of the viscoelastic part.

***Finding the constants required for hyperelastic constitutive model***

For finding the hyperelastic constant, the constitutive model should be fitted to a data set obtained from a tensile test performed in slow speed to eliminate the viscoelastic response of the material. For this purpose, the Yeoh constitutive model is defined in a MATLAB code. The code provides stress-stretch graphs which were fitted to the data found from Wu and Liechti (2000).

After fitting the constitutive model to the data, the model constants are found (see Table 8) and the resultant stress-stretch graph is depicted in Figure 63.

Table 8. Calibrated constants for Yeoh hyperelastic model

| Constants | $c_1$ | $c_2$ | $c_3$ |
|---|---|---|---|
| Values | 300 | -22 | 1.6 |

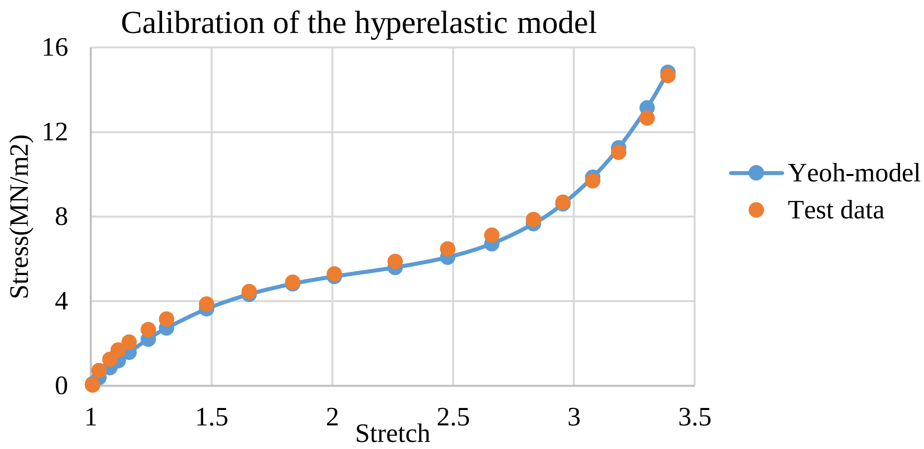


Figure 63. Calibration of Yeoh hyperelastic model

***Finding the constant for viscoelastic part of the constitutive model***

In an experiment, it is not possible to separate the hyerelastic and viscoelastic response of the material. Therefore, for finding the viscoelastic constants of $\tau_i^\alpha$ and $\beta_i^\alpha$, the model should be fitted to a data set obtained from a tensile test performed in a faster speed in comparison to the previous section, so that it includes both viscoelastic and hyperelastic responses of the material. For this purpose, the constants found for the Yeoh constitutive model in the previous section will be used in a MATLAB code to calibrate the viscoelastic part of the model. Similar to the previous section, the code provides stress-stretch graphs which were fitted to the data found from Wu and Liechti (2000).

After fitting the constitutive model to the data, using optimization tools in MATLAB, such as fmincon, the model constants are found (see Table 9) and the resultant stress-stretch graph is depicted in Figure 64.

Table 9. Calibrated constants for Viscoelastic model

| Constants / i | $\tau_i^\alpha$ | $\beta_i^\alpha$ |
|---|---|---|
| 1 | 148.18 | 0.13 |
| 2 | 100.07 | 0.51 |
| 3 | 75.70 | 0.15 |
| 4 | 10.82 | 0.06 |
| 5 | 10.81 | 0.06 |

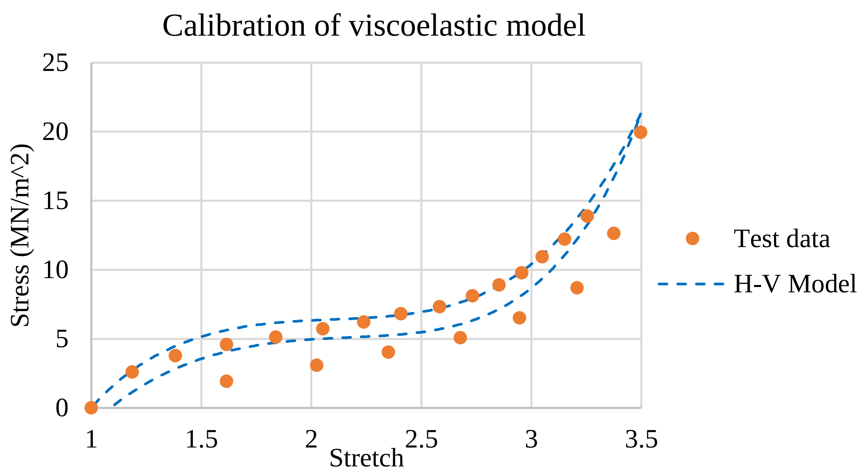


Figure 64. Calibration of hyperelastic-viscoelastic model

### *Controlling the response by comparing the results of the UMAT and built-in Yeoh model in ABAQUS*

To be sure that the UMAT works properly, its results should be compared with the results obtained from an ABAQUS model based on built-in Yeoh constitutive model defined in it. For this purpose, a relaxation tensile test is modeled in ABAQUS which its geometry is depicted in Figure 65. The model consist of a square block of rubber, which is pulled from one side for a predefined strain and then relaxed.

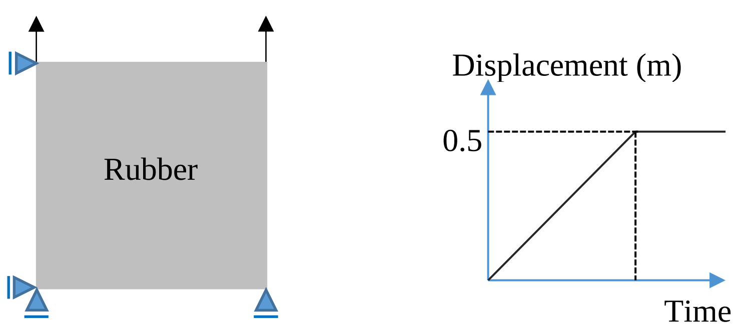


Figure 65. Tensile test modeling in ABAQUS

The comparison of the stress over time of the model for UMAT subroutine and ABAQUS built-in material are shown is Figure 66. As it can be seen, complete agreement exist between the results of the two models.

### *Controlling the response of the viscoelastic part*

For controlling the response of the viscoelastic part, the same tensile test model as the previous section should be used by Viscoelastic UMAT. However, in contrast to the results in Figure 66, stress should relax due to the viscoelastic response of the material in a relaxation test (see Figure 67). For validation of the viscoelastic response, the model can be compared with a standard linear solid model, in both cases of relaxation and creep as it can be seen in Figure 68 (a).

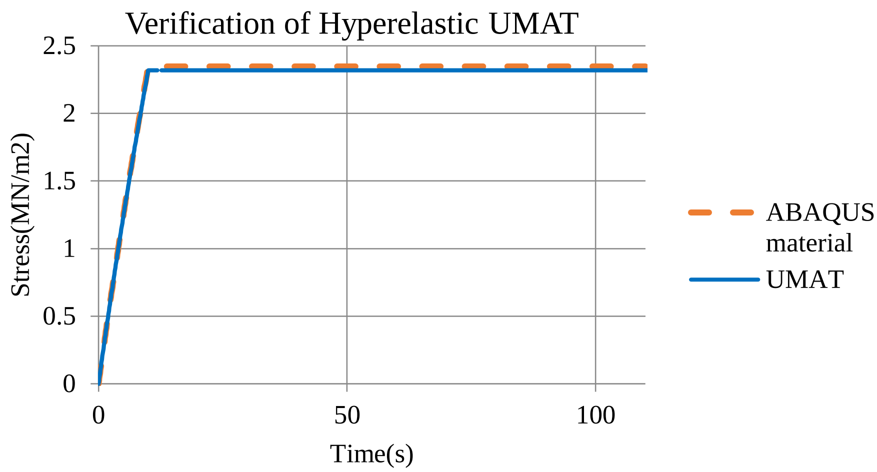


Figure 66. Verification of Hyperelastic UMAT

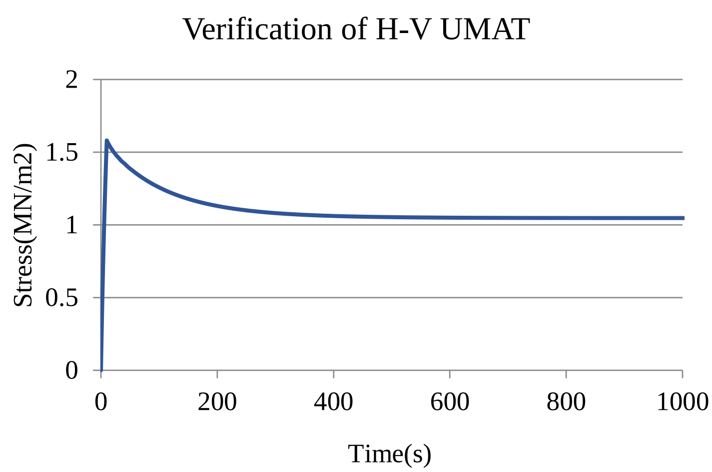


Figure 67. Verification of Hyperelastic-Viscoelastic UMAT

The modulus E and E1 found from both models (relaxation and creep) should match each other. For finding these parameters, the strain and stress should be applied in very slow and very fast speeds. The response of the model in both conditions should be linear due to the dashpot response (see Figure 68 (b) and (c)).

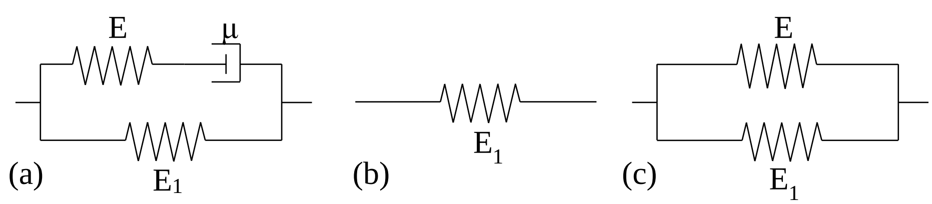


Figure 68. (a) A standard linear solid model (b) response in very slow rates (c) response in very fast rates

As it can be seen, by performing the test in a very slow rate a linear response should be obtained which would give $E_1$. However, the same test in a very fast rate results in E+ $E_1$. After running creep and relaxation tests in these two conditions, the corresponding moduli are obtained which they should be the same. The results achieved from the models are demonstrating the same values for moduli E and $E_1$ (see Figure 69 and Table 10). These results verify the viscoelastic UMAT code which will be later used in the rubber-surface interaction model.

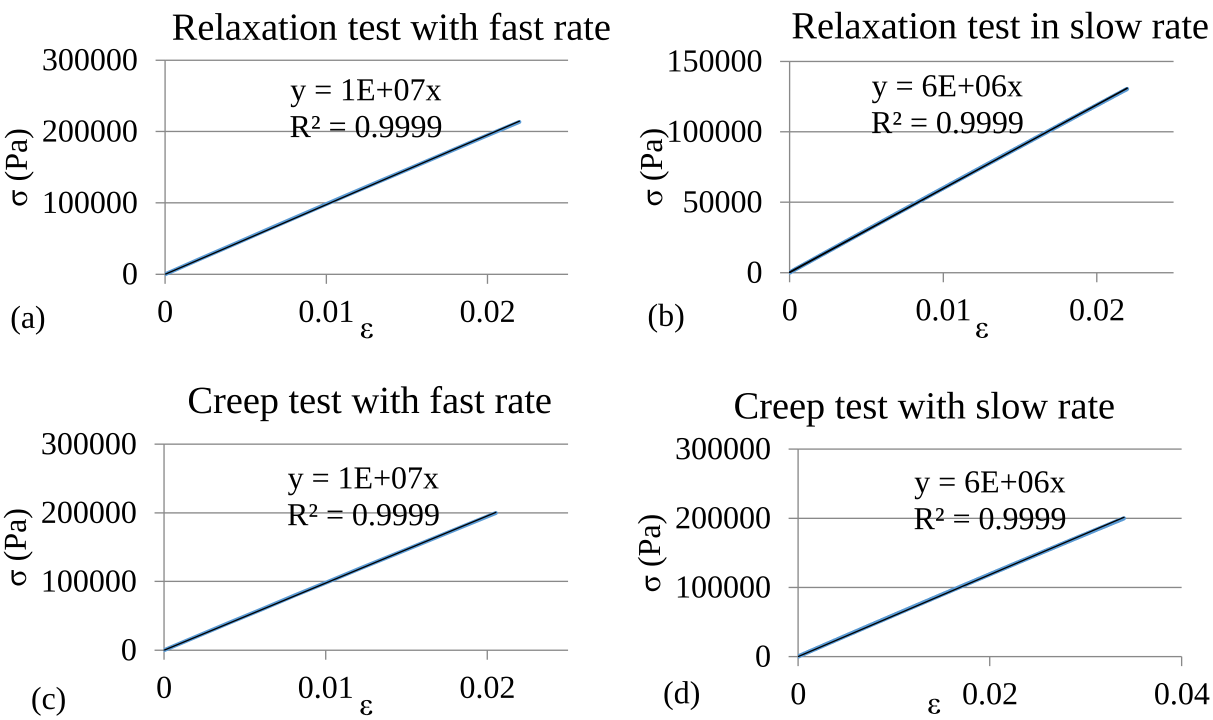


Figure 69. Stress-strain relationships for (a) Relaxation test with fast rate, (b) relaxation test with slow rate (c) creep test with fast rate, and (d) creep test with slow rate

Table 10. Verification of viscoelastic UMAT code

| | Relaxation | Creep test | Relative error (%) |
|---|---|---|---|
| E1 | 5937297 | 5883172 | 0.91 |
| E | 3780122 | 3848070 | 1.76 |

# CHAPTER 6 - DISCUSSION AND CONCLUSION

In this study, different means of surface characterization have been discussed. The statistical parameters such as mean profile depth (MPD) are scale dependent and change with the sample length. Therefore better methods are required for surface characterization when it comes to its simulation. After considering fractal techniques, different methods for finding the fractal dimension have been compared with each other (1D PSD, 2D PSD, roughness-length method, and tessellation). It was found that the results obtained from structure function method were much more than the other methods. However, the results of RMS-roughness and Projective covering methods give similar values, near 2, for most of the samples; while, the results of 1D and 2D PSDs are near 2.5 within the range suggested in the literature for these methods.

Moreover, it could be seen that due to the wide range of wavelength and amplitude presented in a pavement surface, it is not always possible to define the surface with only one fractal dimension. Sometimes it could be more beneficial to characterize the surface in two or more scales and assign a fractal dimension to each scale to obtain a better description for the surface. This scale dependency is shown by different methods which can be used in future studies for surface characterization and simulation and also in relating friction to surface texture.

Another topic which has been investigated in surface characterization is the possibility of finding the driving direction using fractal techniques. When the surface is exposed to a moving wheel its surface gets polished and as a consequence a lower fractal dimension is expected in that direction. With this in mind, surface measurements were performed in different directions and the driving direction was found for the samples. Having different fractal dimension in driving direction is a demonstration of a limitation of the current studies in relating the vehicle performance to surface texture, which have not consider this factor yet.

Four different surface simulation and interpolation techniques were employed in this study (BFIS, IFFT, Blackmore anisotropic simulation and a combination of BFIS and Balckmore). The IFFT method showed a better result in comparison to the fractal techniques, which is in contrary to the expectations. This shows that the fractal techniques employed here are not completely developed in comparison to the IFFT method used, and therefore, more study and work is required to obtain the best results and conclusion.

A 2D FE model has been developed in ABAQUS commercial software for modeling the hysteresis in interaction of the tire tread and surface texture. For this purpose, the rubber was considered as elastic-viscoelastic and hyperelastic-viscoelastic in two different material characterizations. The former was defined as a Prony-series, while a UMAT subroutine code was written for the latter. The pavement surface, however, was considered as a rigid surface. The presented results were all related to the Prony series. For investigation of the surface influence on rubber hysteresis, different pavement surfaces were generated. Different factors, such as the relationship between the applied load, contact area, and penetration depth were investigated. The model could confirm most of the assumptions in contact mechanics. However, it was found that the hysteresis of a surface can be equal to the summation of the hysteresis of the individual length-scales as long as there is zero phase lag between different scales. The results showed that in presence of a phase lag the hysteresis is lower that the summation. This result is in contrary with the previous assumptions in the literature and it should be considered in the future studies.

## TECHNOLOGY TRANSFER

This project is still ongoing and its ultimate goals have not been achieved yet. However, the obtained results and discussions have been transferred to the transportation commodity through the following means:

- Technical talk at FHWA Headquarter VA with the topic of "Pavement Surface Characterization for Optimization of Trade-off between Grip and Rolling Resistance" (October, 2014)
- Publication in TRB conference with the topic of "A review: Pavement Surface Micro-texture and its contribution to Surface Friction"
- Presentation at TRB 2017 Annual Meeting Committee Meeting AFD90 with the topic of "A review: Pavement Surface Micro-texture and its contribution to Surface Friction"
- Technical talk at UIUC with the topic of "Pavement Surface Micro-texture and its contribution to Surface Friction" (February, 2017)

# Reference:


1. American Association of State Highway and Transportation Officials (AASHTO). 1976. Guidelines for Skid-Resistant Pavement Design, Task Force for Pavement Design, AASHTO, Washington, D.C.
2. Andersen, L. G., Larsen, J. K., Fraser, E. S., Schmidt, B., & Dyre, J. C. (2014). Rolling Resistance Measurement and Model Development. Journal of Transportation Engineering, 141(2).
3. Anis BEN SLIMANE, Madji KHOUDEIR, Jacques Brochard, Minh Tan Do. Characterization of road microtexture by means of image analysis. 10th International Conference Metrology and Properties of Engineering Surfaces, Jul 2005, France. 8p, ill., sch_emas, graphique. <hal-00851279>
4. Archard, J. F. (1957), "Elastic Deformation and the Laws of Friction," Proceedings of the Royal Society of London A, 243, pp 190-205.
5. Archard, J. F. (1961). Single contacts and multiple encounters. Journal of Applied Physics, 32(8), 1420-1425.
6. Asi, I. M. (2007). Evaluating skid resistance of different asphalt concrete mixes. Building and Environment, 42(1), 325-329.
7. Bazlamit, S. M., & Reza, F. (2005). Changes in asphalt pavement friction components and adjustment of skid number for temperature. Journal of Transportation Engineering, 131(6), 470-476.
8. Bendtsen, H. (2004). Rolling resistance, fuel consumption-a literature review.ROLLING RESISTANCE, FUEL CONSUMPTION-A LITERATURE REVIEW, (23).
9. Bester, C. J. (1984). Effect of pavement type and condition on the fuel consumption of vehicles (No. HS-039 023).
10. Besselink, I. J. M., Schmeitz, A. J. C., & Pacejka, H. B. (2010). An improved Magic Formula/Swift tyre model that can handle inflation pressure changes.Vehicle System Dynamics, 48(S1), 337-352.
11. Bhushan, B. (1996). Contact mechanics of rough surfaces in tribology: single asperity contact. Applied mechanics reviews, 49(5), 275-298.
12. Bitelli, G., Simone, A., Girardi, F., & Lantieri, C. (2012). Laser scanning on road pavements: A new approach for characterizing surface texture. Sensors, 12(7), 9110-9128.
13. Boere, S. (2009). "Prediction of road texture influence on rolling resistance." M.S. thesis, Eindhoven Univ. of Technology, Eindhoven, Netherlands.
14. Bora, C. K., Flater, E. E., Street, M. D., Redmond, J. M., Starr, M. J., Carpick, R. W., and Plesha, M. E. (2005), "Multiscale Roughness and Modeling of MEMS Interfaces," Tribology Letters, 19(1), pp 37-48.
15. Bush, A. W., Gibson, R. D., and Thomas, T. R. (1975), "The Elastic Contact of Rough Surfaces," Wear, 35, pp 87-111.
16. Cafiso, S., & Taormina, S. (2007). Texture analysis of aggregates for wearing courses in asphalt pavements. International Journal of Pavement Engineering,8(1), 45-54.
17. Carcaterra, A., & Roveri, N. (2013). Tire grip identification based on strain information: Theory and simulations. Mechanical Systems and Signal Processing, 41(1), 564-580.
18. Carr, J. R., Norris, G. M., & Newcomb, D. E. (1990). Characterization of aggregate shape using fractal dimension. Transportation Research Record, (1278).

19. Carr, J. R., Misra, M., & Litchfield, J. (1992). Estimating surface area for aggregate in the size range 1 mm or larger. Transportation Research Record, (1362).
20. Chen, Y., Wang, K. J., & Zhou, W. F. (2013). Evaluation of surface textures and skid resistance of pervious concrete pavement. Journal of Central South University, 20, 520-527.
21. Choubane, B., Holzschuher, C. R., & Gokhale, S. (2004). Precision of locked-wheel testers for measurement of roadway surface friction characteristics.Transportation Research Record: Journal of the Transportation Research Board, 1869(1), 145-151.
22. Ciavarella, M. and Demelio, G. (2001), "Elastic Multiscale Contact of Rough Surfaces: Archard's Model Revisited and Comparisons with Modern Fractal Models," Journal of Applied Mechanics, 68(3), pp 496-498.
23. Ciavarella, M., Murolo, G., Demelio, G., and Barber, J. R. (2004), "Elastic Contact Stiffness and Contact Resistance for the Weierstrass Profile," Journal of the Mechanics and Physics of Solids, 52(6), pp 1247-1265.
24. S. K. Clark, Mechanics of pneumatic tires, U.S. Department of Transportation, National Highway Traffic Safety Administration, 1981.
25. Dames, Jtirgen. The influence of polishing resistance of sand on skid resistance of asphalt concrete. Philadephia, 1990.
26. Dawkins, J.J., R.L. Jackson, and D.M. Bevly, Fractal Terrain Generation for Vehicle Simulation. International Journal of Vehicle Autonomous Systems. In Press.
27. De Wit, C. C., Olsson, H., Astrom, K. J., & Lischinsky, P. (1995). A new model for control of systems with friction. Automatic Control, IEEE Transactions on,40(3), 419-425.
28. M. De Beer, C. Fisher and J. F. J., Determination of pneumatic tyre/pavement interface contact stresses under moving loads and some effects on pavements with thin asphalt surfacing layers, in Eighth International Conference on Asphalt Pavements, Seattle, Washington, 1997.
29. Delanne, Y. (1994). The influence of pavement evenness and macrotexture on fuel consumption. ASTM SPECIAL TECHNICAL PUBLICATION, 1225, 240-240.
30. Descornet, G. (1990). Road-surface influence on tire rolling resistance. Surface characteristics of roadways: International research and technologies, ASTM STP, 1031, 401-415.
31. Dewey, G. R., Robords, A. C., Armour, B. T., & Muethel, R. (2001, July). Aggregate wear and pavement friction. In 80th Transportation Research Board Annual Meeting (p. 152)
32. Do, M. T., Zahouani, H., & Vargiolu, R. (2000). Angular parameter for characterizing road surface microtexture. Transportation Research Record: Journal of the Transportation Research Board, 1723(1), 66-72.
33. Do, M. T., & Marsac, P. (2002, January). Assessment of the polishing of the aggregate microtexture by means of geometric parameters. In TRB 81st Annual Meeting (Transportation Research Board) (pp. 19p-schémas).
34. Dunford, A., 2008. Measuring Skid Resistance without Contact, 2006e2007 Progress Report, Published Project Report PPR 315. Transport and Research Laboratory, Wokingham.
35. Ebbott, T. G., Hohman, R. L., Jeusette, J. P., & Kerchman, V. (1999). Tire temperature and rolling resistance prediction with finite element analysis. Tire Science and Technology, 27(1), 2-21.

36. Ergun, M., Iyinam, S., & Iyinam, A. F. (2005). Prediction of road surface friction coefficient using only macro-and microtexture measurements. Journal of transportation engineering, 131(4), 311-319.
37. FHWA. 1980. Skid Accident Reduction Program. Technical Advisory T5040.17, Federal Highway Administration, U.S. Department of Transportation.
38. Flintsch, Gerardo W., et al. "The little book of tire pavement friction." Surface Properties Consortium [online].2012.
39. Forster, S. W. (1981). Aggregate microtexture: Profile measurement and related frictional levels (No. FHWA-RD-81-107 Final Rpt.).
40. Forster, S. W. (1989). Pavement microtexture and its relation to skid resistance.Transportation Research Record, (1215).
41. Gallaway, Bob M., and Hisao Tomita. "Microtexture Measurements of Pavement Surfaces." Texas Transportation Institute, Texas A&M Univ., CoUege Station, Research Rept (1970): 139-1.
42. Ghoreishy, M. H. R. (2008). A state of the art review of the finite element modelling of rolling tyres. Iranian Polymer Journal, 17(8), 571-597.
43. Greenwood, J. A., & Williamson, J. B. P. (1966). Contact of nominally flat surfaces. Proceedings of the Royal Society of London. Series A. Mathematical and Physical Sciences, 295(1442), 300-319..
44. Guo, Z., Meng, Y., Wu, H., Su, C., & Wen, S. (2007). Measurement of static and dynamic friction coefficients of sidewalls of bulk-microfabricated MEMS devices with an on-chip micro-tribotester. Sensors and Actuators A: Physical,135(2), 863-869.
45. Gustafsson, F. (1997). Slip-based tire-road friction estimation. Automatica,33(6), 1087-1099.
46. W. Hall, Finite element modeling and simulation for a 'smart' tyre, Coventry: University of Warwick, 2003.
47. Hall, J. W., Smith, K. L., Titus-Glover, L., Wambold, J. C., Yager, T. J., & Rado, Z. (2009). NCHRP web-only document 108: Guide for pavement friction.Transportation Research Board of the National Academies, Washington, DC.
48. Hammarström, U., Karlsson, R., & Sörensen, H. (2009). Road surface effects on rolling resistance–coastdown measurements with uncertainty analysis in focus. Deliverable D5 (a). The Swedish Road and Transport Research Institute/EIE/06/039 S, 12.
49. Heinrich, Gert, and Manfred Klüppel. "Rubber friction, tread deformation and tire traction." Wear 265.7 (2008): 1052-1060.
50. R. Henderson, G. Cook, P. Cenek, J. Patrick, S. Potter ,The effect of crushing on the skid resistance of chipseal roads. Land Transport NZ, 2006.
51. Henry, John Jewett. Evaluation of pavement friction characteristics. Vol. 291. Transportation Research Board, 2000
52. Henry, J. J., & Dahir, S. H. (1979). Effects of Textures and the Aggregates that produce them on the Performance of Bituminous Surfaces. Transportation Research Record, (712).
53. Henry, John J. "Tire wet-pavement traction measurement: A state-of-the-art review." The Tire Pavement Interface: A Symposium. Eds. M. G. Pottinger, and T. J. Yager. Vol. 929. ASTM International, 1986.
54. Hogervorst, D. (1974). Some properties of crushed stone for road surfaces.Bulletin of the International Association of Engineering Geology-Bulletin de l'Association Internationale de Géologie de l'Ingénieur, 10(1), 59-64.

55. Home, W. B., & Buhlmann, F. (1983). A method for rating the skid resistance and micro/macrotexture characteristics of wet pavements. Frictional interaction of tire and pavement, ASTM STP, 793, 191-218.
56. Hoever, C., & Kropp, W. (2013, September). The influence of lateral road surface resolution on the simulation of car tyre rolling losses and rolling noise. In Proceedings of Internoise 2013, The 42nd International Congress and Exposition on Noise Control Engineering, Innsbruck, 15.-18. Sept. 2013.
57. Jackson, R. L. and Streator, J. L. (2006), "A Multiscale Model for Contact between Rough Surfaces," Wear, 261(11-12), pp 1337-1347.
58. Jackson, R. L. and Green, I. (2006), "A Statistical Model of Elasto- Plastic Asperity Contact between Rough Surfaces," Tribology International, 39(9), pp 906-914.
59. Jamieson, N.J. and Cenek, P.D.(1999): "Effects of Pavement Construction on the Fuel Consumption of Trucks," in Proceedings of the Options for Post Millenium Pavements Symposium, Wairekei Resort, Taupo, New Zealand, 17-19 Oct.1999
60. Javidi, Bahram, Daesuk Kim, and Sherif El-Sayed Kishk. A laser-based 3D data acquisition system for the analysis of pavement distress and roughness. No. JHR 04-300. Connecticut Transportation Institute, School of Engineering, University of Connecticut, 2004.
61. Jayawickrama, P. W., R. Prasanna, and S. P. Senadheera. "Survey of state practices to control skid resistance on hot-mix asphalt concrete pavements."Transportation Research Record: Journal of the Transportation Research Board1536.1 (1996): 52-58.
62. Johnsen, William A. Advances in the design of pavement surfaces. Diss. Worcester Polytechnic Institute, 1997.
63. Khasawneh, M. A., & Liang, R. Y. (2008). Correlation Study Between Locked-Wheel Skid Trailer and Dynamic Friction Tester. In Transportation Research Board 87th Annual Meeting (No. 08-2442).
64. Keller, J. M., Chen, S., & Crownover, R. M. (1989). Texture description and segmentation through fractal geometry. Computer Vision, Graphics, and Image Processing, 45(2), 150-166
65. Kissoff, N. V. "Investigation of regional differences in Ohio pavement skid resistance through simulation modeling." PhD dissertation, Univ. of Toledo, Toledo, Ohio. 1988.
66. Kogut, L. and Jackson, R. L. (2005), "A Comparison of Contact Modeling Utilizing Statistical and FractalApproaches," Journal of Tribology, 128(1), pp 213-217
67. Kokkalis, A. G., & Panagouli, O. K. (1998). Fractal evaluation of pavement skid resistance variations. I: surface wetting. Chaos, Solitons & Fractals, 9(11), 1875-1890.
68. Kokkalis, A. G., Tsohos, G. H., & Panagouli, O. K. (2002). Consideration of fractals potential in pavement skid resistance evaluation. Journal of transportation engineering, 128(6), 591-595.
69. Kowalski, Karol J., Rebecca S. McDaniel, and Jan Olek. "Identification of Laboratory Technique to Optimize Superpave HMA Surface Friction Characteristics." (2010).
70. KummerHW, Unified Theory of Rubber and Tire Friction, Engineering Research Bulletin B-94 Engineering Publications, The Pennsylvania State University(1966)
71. Kuttesch, Jeffrey S. Quantifying the relationship between skid resistance and wet weather accidents for virginia data. Diss. Virginia Polytechnic Institute and State University, 2004.
72. Larsson, K. (2000). A rolling contact model using green's functions. InterNoise 29 27-30 August 2000, Nice, France

73. Leu, M. C., & Henry, J. J. (1978). Prediction of skid resistance as a function of speed from pavement texture measurements. Transportation Research Record, (666).
74. Li, L., & Chan, P. (1993). Quantitative analysis of aggregate shape based on fractals. ACI Materials Journal, 90(4).
75. Li, S., Noureldin, S., & Zhu, K. (2010). Safety Enhancement of the INDOT Network Pavement Friction Testing Program: Macrotexture and Microtexture Testing Using Laser Sensors.
76. Li, S., Zhu, K., Noureldin, S., & Harris, D. (2005). Identifying friction variations with the standard smooth tire for network pavement inventory friction testing.Transportation Research Record: Journal of the Transportation Research Board, 1905(1), 157-165.
77. Lin, Y. J., & Hwang, S. J. (2004). Temperature prediction of rolling tires by computer simulation. Mathematics and Computers in Simulation, 67(3), 235-249.
78. Lindner, M., Kröger, M., Popp, K., & Blume, H. (2004). Experimental and analytical investigation of rubber friction. Safety, 200, 300.
79. Liu, C. S., & Peng, H. (1996). Road friction coefficient estimation for vehicle path prediction. Vehicle system dynamics, 25(S1), 413-425.
80. Liu, Y., Fwa, T. F., & Choo, Y. S. (2004). Effect of surface macrotexture on skid resistance measurements by the British Pendulum Test. Journal of Testing and Evaluation, 32(4), 304-309.
81. Lopez, I. (2010). Influence of material damping on the prediction of road texture and tread pattern related rolling resistance. In Proceedings of the International Conference on Noise and Vibration Engineering ISMA (pp. 4039-4052).
82. Luchini, J. R., Peters, J. M., & Arthur, R. H. (1994). Tire rolling loss computation with the finite element method. Tire Science and Technology,22(4), 206-222.
83. Luce, Anthony David. Analysis of aggregate imaging system (AIMS) measurements and their relationship to asphalt pavement skid resistance. Diss. Texas A&M University, 2006.
84. Lu, Q., and B. Steven. Friction Testing of Pavement Preservation Treatments: Literature Review. Publication UCPRC-TM-2006-10. University of California, California Department of Transportation, December 2006
85. Mahboob Kanafi, M., Kuosmanen, A., Pellinen, T. K., & Tuononen, A. J. (2015). Macro- and micro-texture evolution of road pavements and correlation with friction. International Journal of Pavement Engineering, 16(2), 168-179.
86. Mandelbrot, B. B. (1983). The fractal geometry of nature. Macmillan
87. Majumdar, A. and Bhushan, B. (1991), "Fractal Model of Elastic–Plastic Contact between Rough Surfaces." Journal of Tribology, 113(1), pp 1-11.
88. Majumdar, A. and Bhushan, B. (1990), "Role of Fractal Geometry in Roughness Characterization and Contact Mechanics of Surfaces," Journal of Tribology, 112(2), pp 205-216.
89. Matilainen, M. J. & Tuononen, A. J. (2012), 'Intelligent tire to measure contact length in dry asphalt and wet concrete conditions', Seoul: AVEC 12, 1--6.
90. Mc Allen, J., Cuitino, A. M., & Sernas, V. (1996). Numerical investigation of the deformation characteristics and heat generation in pneumatic aircraft tires: Part I. Mechanical modeling. Finite elements in analysis and design, 23(2), 241-263.
91. Mc Allen, J., Cuitino, A. M., & Sernas, V. (1996). Numerical investigation of the deformation characteristics and heat generation in pneumatic aircraft tires: Part II. Thermal modeling. Finite elements in analysis and design, 23(2), 265-290

92. McCool, J. I. (1986), “Comparison of Models for the Contact of Rough Surfaces,” Wear, 107(1), pp 37-60.
93. McLean, J., & Foley, G. (1998). Road surface characteristics and condition: effects on road users (No. ARR 314).
94. Meyer, W. E., Hegmon, R. R., & Gillespie, T. D. (1974). Locked-Wheel Pavement Skid Tester Correlation and Calibration Techniques. NCHRP report, (151).
95. Moore, D. F. (1975). The friction of pneumatic tyres.
96. Neese, Jesse L. "Characterizing veneer roughness and glue-bond performance in Douglas-fir plywood." (1997).
97. Nielsen, C. and T.D.F. Skibsted, The Energy-Saving Road: Improving Socio-Economic Conditions by Reducing Rolling Resistance. A Socio-Economic Report. 2010, NCC Roads A/S: Denmark
98. Nordström, O. (1998). Development and validation of BV14, a new twin track fixed slip friction tester for winter road maintenance monitoring in Sweden. InXTH PIARC INTERNATIONAL WINTER ROAD CONGRESS 16-19 MARCH 1998 IN LULEAA, SWEDEN (Vol. 3).
99. Noyce, D. A., Bahia, H. U., Yambó, J. M., & Kim, G. (2005). Incorporating road safety into pavement management: maximizing asphalt pavement surface friction for road safety improvements. Midwest Regional University Transportation Center Traffic Operations and Safety (TOPS) Laboratory.
100. Ono, E., Hattori, Y., & Muragishi, Y. (2005). Estimation of tire friction circle and vehicle dynamics integrated control for four-wheel distributed steering and four-wheel distributed traction/braking systems. R&D Review of Toyota CRDL,40(4), 7-13.
101. Ong, Ghim Ping, T. F. Fwa, and Jing Guo. "Modeling hydroplaning and effects of pavement microtexture." Transportation Research Record: Journal of the Transportation Research Board 1905.1 (2005): 166-176.
102. Park, H. C., Youn, S. K., Song, T. S., & Kim, N. J. (1997). Analysis of temperature distribution in a rolling tire due to strain energy dissipation. Tire Science and Technology, 25(3), 214-228.
103. Pasterkamp, W. R., & Pacejka, H. B. (1997). The tyre as a sensor to estimate friction. Vehicle System Dynamics, 27(5-6), 409-422
104. Pelloli, Rita. Road surface characteristics and hydroplaning. No. Proceeding. 1977.
105. Persson, B. N. J. (2001), “Elastoplastic Contact between Randomly Rough Surfaces,” Physical Review Letters, 87(11), p 116101.
106. Persson, B. N. J., Bucher, F., and Chiaia, B. (2002), “Elastic Contact between Randomly Rough Surfaces: Comparison of Theory with Numerical Results,” Physical Review B, 65, p 184106-1.
107. Persson, B. N. (2001), 'Theory of rubber friction and contact mechanics', The Journal of Chemical Physics 115(8), 3840--3861.
108. Persson, Bo NJ. "Contact mechanics for randomly rough surfaces." Surface Science Reports 61.4 (2006): 201-227.
109. PIARC Technical Committee on Surface Characteristics (C1) 1995. International PIARC Experiment to Compare and Harmonize Texture and Skid Resistance Measurements, Paris, France Saito, Kazuo, et al. "Development of portable tester for measuring skid resistance and its speed dependency on pavement surfaces." Transportation Research Record: Journal of the Transportation Research Board 1536.1 (1996): 45-51.

110. Pinnington, R. J. "Rubber friction on rough and smooth surfaces." Wear267.9 (2009): 1653-1664
111. Pinnington, R. J. (2012). A particle-envelope surface model for road–tyre interaction. International Journal of Solids and Structures, 49(3), 546-555.
112. Pollock, H. M., Shufflebottom, P., & Skinner, J. (1977). Contact adhesion between solids in vacuum. I. Single-asperity experiments. Journal of Physics D: Applied Physics, 10(1), 127.
113. Putman, C. A., Igarashi, M., & Kaneko, R. (1995). Single-asperity friction in friction force microscopy: The composite-tip model. Applied physics letters,66(23), 3221-3223.
114. Radó, Zoltán. A study of road surface texture and its relationship to friction. Diss. Pennsylvania State University, 1994
115. Rao, K. N., Kumar, R. K., & Bohara, P. C. (2006). A sensitivity analysis of design attributes and operating conditions on tyre operating temperatures and rolling resistance using finite element analysis. Proceedings of the Institution of Mechanical Engineers, Part D: Journal of Automobile Engineering, 220(5), 501-517.
116. Rezaei, A., Chowdhury, A., & Harris, P. (2009). Predicting asphalt mixture skid resistance based on aggregate characteristics.
117. Ribble, C., Szecsy, R., & Zollinger, D. G. (1992, April). Aggregate macro shape and micro texture in concrete mix design. In ASCE Spring Meeting, New York.
118. Rocchini, C. M. P. P. C., Cignoni, P., Montani, C., Pingi, P., & Scopigno, R. (2001, September). A low cost 3D scanner based on structured light. InComputer Graphics Forum (Vol. 20, No. 3, pp. 299-308). Blackwell Publishers Ltd.
119. Rohde, Steve M. "On the effect of pavement microtexture on thin film traction." International Journal of Mechanical Sciences 18.2 (1976): 95-101.
120. Roovers, M. S., Graaff, D. D., & Moppes, R. V. (2005). Round robin test rolling resistance/energy consumption. Ministry of Traffic and Waterworks DWW, M+ P consulting engineers, Vught Shida, Z., Koishi, M., Kogure, T., & Kabe, K. (1999). A rolling resistance simulation of tires using static finite element analysis. Tire Science and Technology, 27(2), 84-105
121. Samuels, S. E. (1986). The feasibility of measuring road surface microtexture by means of laser techniques.
122. Saito, K., Horiguchi, T., Kasahara, A., Abe, H., & Henry, J. J. (1996). Development of portable tester for measuring skid resistance and its speed dependency on pavement surfaces. Transportation Research Record: Journal of the Transportation Research Board, 1536(1), 45-51.
123. Salah H R Ali, 'Advanced Nanomeasuring Techniques for Surface Characterization',ISRN Optics, Vol 2012, Article ID 859353
124. Sandberg, U., & Ejsmont, J. A. (2000). Noise Emission, Friction and Rolling Resistance of Car Tires: Summary of an Experimental Study. Swedish National Road and Transport Research Institute.
125. Sandberg, U., Bergiers, A., Ejsmont, J. A., Goubert, L., Karlsson, R., & Zöller, M. (2011). Road surface influence on tyre/road rolling resistance. Swedish Road and Transport Research Institute (VTI), Prepared as part of the project MIRIAM, Models for rolling resistance in road infrastructure asset management systems.

126. Sansoni, G.; Trebeschi, M.; Docchio, F. State-of-the-art and applications of 3D imaging sensors in industry, cultural heritage, medicine, and criminal investigation. Sensors 2009, 9, 568–601.
127. Savkoor, A. R. "Paper viii (iii) Tribology of tyre traction on dry and wet roads." Tribology Series 18 (1991): 213-228.
128. Serigos, P. A., Smit, A. D. F., & Prozzi, J. A. (2014). Incorporating Surface Micro-texture in the Prediction of Skid Resistance of Flexible Pavements. InTransportation Research Board 93rd Annual Meeting (No. 14-2278).
129. H. Shiobara, T. Akasaka and S. Kagami, Two-dimensional contact pressure distribution of a radial tire in motion, Tire Science and Technology, vol. 24, pp. 294-320, 1996.
130. Slimane, A. B., Khoudeir, M., Brochard, J., & Do, M. T. (2008). Characterization of road microtexture by means of image analysis. Wear, 264(5), 464-468.
131. Smith, Kelly L., et al. Guide for pavement friction. National Cooperative Highway Research Program, Transportation Research Board of the National Academies, 2009.
132. Song, T. S., Lee, J. W., & Yu, H. J. (1998). Rolling resistance of tires-an analysis of heat generation (No. 980255). SAE Technical Paper.
133. Stanley, H. M. and Kato, T. (1997), "FFT-Based Method for Rough Surface Contact," Journal of Tribology, 119(3), pp 481-485.
134. Stroup-Gardiner, M., Studdard, J., & Wagner, C. (2004). Evaluation of hot mix asphalt macro-and microtexture. Journal of Testing and Evaluation, 32(1), 7-16.
135. Taneerananon, P., and W. O. Yandell. "Microtexture roughness effect on predicted road-tyre friction in wet conditions." Wear 69.3 (1981): 321-337.
136. A. Tsotras, On the interaction between modal behaviour and shear force behaviour of a pneumatic tyre, Loughborough: Loughborough University, 2010.
137. Ueckermann, Andreas, et al. "Calculation of skid resistance from texture measurements." Journal of Traffic and Transportation Engineering (English Edition) 2.1 (2015): 3-16.
138. Vantsevich, V. V., & Stuart, C. (2007, January). Probabilistic interactions of vehicles with surroundings: Modeling for dynamic control. In ASME 2007 International Mechanical Engineering Congress and Exposition (pp. 1649-1658). American Society of Mechanical Engineers
139. Wallman, Carl-Gustaf, and Henrik Astrom. "Friction measurement methods and the correlation between road friction and traffic safety." A literature review. VTI meddelande A 911 (2001): 2001.
140. WanYu Liu ; Xiaoming Sun ; Jian Ping Huang and Kai Xie "Pavement roughness measurement based on structure light", Proc. SPIE 7133, Fifth International Symposium on Instrumentation Science and Technology, 71332X (January 12, 2009); doi:10.1117/12.810576;
141. Wang, Hao, Imad L. Al-Qadi, and Ilinca Stanciulescu. "Effect of Surface Friction on Tire–Pavement Contact Stresses during Vehicle Maneuvering."Journal of Engineering Mechanics 140.4 (2013): 04014001.
142. Warren, T. L. and Krajcinovic, D. (1995), "Fractal Models of Elastic–Perfectly Plastic Contact of Rough Surfaces Based on the Cantor Set," International Journal of Solids and Structures, 32(19), pp 2907-2922.

143. Weiss, M., Tsujimoto, S., & Yoshinaga, H. (1993). Belt construction optimization for tire weight reduction using the finite element method. Tire Science and Technology, 21(2), 120-134.
144. Williams, A. R., & Lees, G. (1970). Topographical and petrographical variation of road aggregates and the wet skidding resistance of tyres. Quarterly Journal of Engineering Geology and Hydrogeology, 2(3), 217-236.
145. Williams, F. R., & Dudek, T. J. (1982). Load-deflection hysteresis and its relationship to tire rolling resistance.
146. Willner, K. (2004), "Elasto-Plastic Normal Contact of Three-Dimensional Fractal Surfaces Using Halfspace Theory," Journal of Tribology, 126(1), pp 28-33.
147. Woźniak, R., Taryma, S., & Ronowski, G. (2012). Modernization of the Trailer for Tyre/Road Rolling Resistance Measurements. Key Engineering Materials,490, 179-186.
148. Wriggers, Peter, and Jana Reinelt. "Multi-scale approach for frictional contact of elastomers on rough rigid surfaces." Computer Methods in Applied Mechanics and Engineering 198.21 (2009): 1996-2008.
149. Wu, J-D., and Kenneth M. Liechti. "Multiaxial and time dependent behavior of a filled rubber." Mechanics of Time-Dependent Materials 4.4 (2000): 293-331.
150. Wullens, F., & Kropp, W. (2004). A three-dimensional contact model for tyre/road interaction in rolling conditions. Acta Acustica united with Acustica,90(4), 702-711.
151. Yan, W. and Komvopoulos, K. (1998), "ContactAnalysis of Elastic–Plastic Fractal Surfaces," Journal of Applied Physics, 84(7), pp 3617-3624.
152. Yandell, W. O. (1971). A new theory of hysteretic sliding friction. Wear,17(4), 229-244.
153. Yandell, W. O., & Sawyer, S. (1994). Prediction of tire-road friction from texture measurements. Transportation Research Record, (1435).
154. Yoon, E. S., Singh, R. A., Oh, H. J., & Kong, H. (2005). The effect of contact area on nano/micro-scale friction. Wear, 259(7), 1424-1431.

# Appendix A – Yeoh Hyperelastic sobroutine UMAT

```
c***********************************************************************
      subroutine umat(stress,statev,ddsdde,sse,spd,scd,rpl,ddsddt,
     #drplde,drpldt,stran,dstran,time,dtime,temp,dtemp,predef,dpred,
     #materl,ndi,nshr,ntens,nstatv,props,nprops,coords,drot,pnewdt,
     #celent,dfgrd0,dfgrd1,noel,npt,kslay,kspt,kstep,kinc)
      include 'aba_param.inc'
      character*8 materl
      real*8 stress(ntens),statev(nstatv),ddsdde(ntens,ntens)
      real*8 ddsddt(ntens),drplde(ntens),stran(ntens),dstran(ntens)
      real*8 time(2),dfgrd0(3,3),dfgrd1(3,3),predef(1),dpred(1)
      real*8 props(nprops),coords(3),drot(3,3)
      real*8 dtime,sse
      integer i1,i2
      real*8  delta(3,3)
      real*8  detf,f(3,3),c(3,3),cinv(3,3)
      real*8  spk(3,3),cmat(3,3,3,3)
      real*8  sigma(3,3),spmat(3,3,3,3)
      do i1=1,3
        do i2=1,3
          delta(i1,i2)=0.0d0
          f(i1,i2)=dfgrd1(i1,i2)
        enddo ! i2
        delta(i1,i1)=1.0d0
      enddo ! i1
      call kinematics(f,detf,c,cinv)
      call spkcmat(nprops,props,delta,detf,c,cinv,spk,cmat)
      call cauchyspmat(delta,detf,f,spk,cmat,sigma,spmat)
      call assign(ntens,sigma,spmat,stress,ddsdde)
      return
      end
c***********************************************************************
c***********************************************************************
      subroutine kinematics(f,detf,c,cinv)
      implicit none
      integer  i1,i2,i3
      real*8   f(3,3)
      real*8   fac
      real*8   detf,c(3,3),cinv(3,3)
      detf=f(1,1)*f(2,2)*f(3,3)
     #    -f(1,1)*f(2,3)*f(3,2)
     #    -f(1,2)*f(2,1)*f(3,3)
     #    +f(1,2)*f(2,3)*f(3,1)
     #    +f(1,3)*f(2,1)*f(3,2)
```

```
     #    -f(1,3)*f(2,2)*f(3,1)

      do i1=1,3
        do i2=1,3
          c(i1,i2)=0.0d0
          do i3=1,3
            c(i1,i2)=c(i1,i2)+f(i3,i1)*f(i3,i2)
          enddo ! i3
        enddo ! i2
      enddo ! i1
      cinv(1,1)=+c(2,2)*c(3,3)-c(2,3)*c(3,2)
      cinv(1,2)=-c(1,2)*c(3,3)+c(1,3)*c(3,2)
      cinv(1,3)=+c(1,2)*c(2,3)-c(1,3)*c(2,2)
      cinv(2,1)=-c(2,1)*c(3,3)+c(2,3)*c(3,1)
      cinv(2,2)=+c(1,1)*c(3,3)-c(1,3)*c(3,1)
      cinv(2,3)=-c(1,1)*c(2,3)+c(1,3)*c(2,1)
      cinv(3,1)=+c(2,1)*c(3,2)-c(2,2)*c(3,1)
      cinv(3,2)=-c(1,1)*c(3,2)+c(1,2)*c(3,1)
      cinv(3,3)=+c(1,1)*c(2,2)-c(1,2)*c(2,1)
      fac=1.0d0/(detf*detf)
      do i1=1,3
        do i2=1,3
          cinv(i1,i2)=cinv(i1,i2)*fac
        enddo ! i2
      enddo ! i1
      return
      end
c***********************************************************************
c***********************************************************************
      subroutine spkcmat(nprops,props,delta,detf,c,cinv,spk,cmat)
      implicit none
      integer  nprops
      real*8   props(nprops),delta(3,3)
      real*8   detf,c(3,3),cinv(3,3)
      integer  i1,i2,i3,i4
      real*8   alpha1,fac0,fac1,fac2,fac3,fac4,fac5,fac6
      real*8   ak,c1,c2,c3
      real*8   fac7,fac8,fac9,fac,fac10,fac11
              real*8   alpha2
      real*8   y(3,3),yf(3,3),ys(3,3)
      real*8   cmatisoe2(3,3,3,3)
      real*8   dcinvdc(3,3,3,3)
      real*8   cmatisoe1(3,3,3,3),cmatisov(3,3,3,3)
      real*8   spk(3,3),cmat(3,3,3,3)

      alpha1=c(1,1)+c(2,2)+c(3,3)
```

```
 fac0=0.5d0
 do i1=1,3
   do i2=1,3
     do i3=1,3
       do i4=1,3
         dcinvdc(i1,i2,i3,i4)=-fac0*cinv(i1,i3)*cinv(i2,i4)
#                           -fac0*cinv(i1,i4)*cinv(i2,i3)
       enddo ! i4
     enddo ! i3
   enddo ! i2
 enddo ! i1
 ak=props(1)
 c1=props(2)
 c2=props(3)
         c3=props(4)
 fac0=detf**(-2.0d0/3.0d0)
         fac=ak*(detf*detf-1.0d0)/2.0d0
         alpha2=fac0*alpha1
         fac1=alpha2-3.0d0
 fac2=fac0
 fac3=alpha2/3.0d0
         fac4=c1+2.0d0*c2*(fac1)+3.0d0*c3*(fac1)**(2.0d0)
          do i1=1,3
   do i2=1,3
                     y(i1,i2)=fac2*delta(i1,i2)-fac3*cinv(i1,i2)
     spk(i1,i2)=fac*cinv(i1,i2)+2.0d0*y(i1,i2)*fac4
   enddo !i2
 enddo ! i1
 fac5=4.0d0*(2.0d0*c2+6.0d0*c3*(alpha2-3.0d0))
 fac6=4.0d0*fac0/3.0d0
 fac7=4.0d0*alpha2/9.0d0
 fac8=4.0d0*alpha2/3.0d0
         fac9=4.0d0*fac4
         fac10=ak*(detf*detf-1.0d0)
 fac11=ak*detf*detf
 do i1=1,3
   do i2=1,3
     do i3=1,3
       do i4=1,3
                                 yf(i1,i2)=fac2*delta(i1,i2)-fac3*cinv(i1,i2)
                                 ys(i3,i4)=fac2*delta(i3,i4)-fac3*cinv(i3,i4)
         cmatisoe1(i1,i2,i3,i4)=fac5*yf(i1,i2)*ys(i3,i4)
         cmatisoe2(i1,i2,i3,i4)=-fac6*delta(i1,i2)*cinv(i3,i4)
#                            -fac6*cinv(i1,i2)*delta(i3,i4)
#                            +fac7*cinv(i1,i2)*cinv(i3,i4)
#                            -fac8*dcinvdc(i1,i2,i3,i4)
```

```
                cmat(i1,i2,i3,i4)=fac9*cmatisoe2(i1,i2,i3,i4)
     #                   +fac5*yf(i1,i2)*ys(i3,i4)
     #                   +fac10*dcinvdc(i1,i2,i3,i4)
     #                   +fac11*cinv(i1,i2)*cinv(i3,i4)
            enddo ! i4
          enddo ! i3
        enddo ! i2
      enddo ! i1
      return
      end

c***********************************************************************

c***********************************************************************
      subroutine cauchyspmat(delta,detf,f,spk,cmat,sigma,spmat)
      implicit none
      real*8   delta(3,3),detf,f(3,3),spk(3,3),cmat(3,3,3,3)
      integer  i1,i2,i3,i4,i5,i6,i7,i8
      real*8   fac0,fac1
      real*8   sigma(3,3),spmat(3,3,3,3)
      fac0=1.0d0/detf
      do i1=1,3
        do i2=1,3
          sigma(i1,i2)=0.0d0
          do i3=1,3
            do i4=1,3
              sigma(i1,i2)=sigma(i1,i2)+f(i1,i3)*spk(i3,i4)*f(i2,i4)
            enddo ! i4
          enddo ! i3
          sigma(i1,i2)=fac0*sigma(i1,i2)
        enddo ! i2
      enddo ! i1

      fac0=1.0d0/detf
      fac1=0.5d0
      do i1=1,3
        do i2=1,3
          do i3=1,3
            do i4=1,3
              spmat(i1,i2,i3,i4)=0.0d0
              do i5=1,3
                do i6=1,3
                  do i7=1,3
                    do i8=1,3
                      spmat(i1,i2,i3,i4)=spmat(i1,i2,i3,i4)
     #                 +f(i1,i5)*f(i2,i6)*cmat(i5,i6,i7,i8)
     #                 *f(i3,i7)*f(i4,i8)
```

```
            enddo ! i8
           enddo ! i7
          enddo ! i6
         enddo ! i5
         spmat(i1,i2,i3,i4)=fac0*spmat(i1,i2,i3,i4)
         spmat(i1,i2,i3,i4)=spmat(i1,i2,i3,i4)
     #                +fac1*delta(i1,i3)*sigma(i2,i4)
     #                +fac1*delta(i1,i4)*sigma(i2,i3)
     #                +fac1*sigma(i1,i3)*delta(i2,i4)
     #                +fac1*sigma(i1,i4)*delta(i2,i3)
        enddo ! i4
       enddo ! i3
      enddo ! i2
      enddo ! i1

      return
      end
c***********************************************************************
c***********************************************************************
      subroutine assign(ntens,sigma,spmat,stress,ddsdde)
      implicit none
      integer  ntens
      real*8   sigma(3,3),spmat(3,3,3,3)
      integer  i,j,i1,i2,j1,j2
      real*8   stress(ntens),ddsdde(ntens,ntens)
      integer  ind1(4),ind2(4)
      data     ind1/1,2,3,1/
      data     ind2/1,2,3,2/

      do i=1,ntens
       i1=ind1(i)
       i2=ind2(i)
       stress(i)=sigma(i1,i2)
       do j=1,ntens
        j1=ind1(j)
        j2=ind2(j)
        ddsdde(i,j)=spmat(i1,i2,j1,j2)
       enddo ! j
      enddo ! i

      return
      end
c***********************************************************************
```